NOTICE

The quality of this microform is heavily dependent upon the quality of the original thesis submitted for microfilming. Every effort has been made to ensure the highest quality of reproduction possible.

If pages are missing, contact the university which granted the degree.

Some pages may have indistinct print especially if the original pages were typed with a poor typewriter ribbon or if the university sent us an inferior photocopy.

AVIS

La qualité de cette microforme dépend grandement de la qualité de la thèse soumise au microfilmage. Nous avons tout fait pour assurer une qualité supérieure de reproduction.

S'il manque des pages, veuillez communiquer avec l'université qui a conféré le grade.

La qualité d'impression de certaines pages peut laisser à désirer, surtout si les pages originales ont été dactylographiées à l'aide d'un ruban usé ou si l'université nous a fait parvenir une photocopie de qualité inférieure.

Canadä

The Preparation and Characterisation of Compounds

in MF_2-SnF_2 Systems (M=Ba and Ca)

Zhimeng Zhu

A Thesis

in

The Department

of

Chemistry

Presented in partial Fulfilment of the Requirements

for the Degree of Master of Science at

Concordia University

Montreal, Quebec, Canada

October 1990

ISBN 0-315-64671-3

Canada

ABSTRACT

The Preparation and Characterization of Compounds

in the MF_2-SnF_2 systems (M=Ba and Ca)

Zhimeng Zhu

Two new mixed fluorides of tin(II) and calcium have been prepared by reaction of aqueous solutions of SnF_2 and $Ca(NO_3)_2 \cdot 4H_2O$ under strictly controlled conditions. The end products of the reaction are highly dependent on the local Ca concentration in the solution. One is crystalline $CaSn_2F_6$ with tin(II) possessing a stereoactive lone pair of electrons with strong p character. The other is a fluorite-type $Ca_{1-x}Sn_xF_2$ solid solution with random orientation of the tin-lone pair axis. Both phases show zero stabilization by the lattice energy (no increase in compacity) and therefore are not very stable. $CaSn_2F_6$ loses SnF_2 in aqueous solutions to give $Ca_{1-x}Sn_xF_2$; this SnF_2 is partly oxidized by oxygen dissolved in water to give Sn_7F_{16} and SnO_2. This has resulted in the first reported preparation of Sn_7F_{16} from aqueous solution. $CaSn_2F_6$ is thermally unstable, in agreement with density measurements, and decomposes at ca. 220 °C to give SnF_2 and CaF_2. $Ca_{1-x}Sn_xF_2$ has an ionic conductivity of 5×10^{-3} (ohm^{-1}cm^{-1}K) at 400K and an activation energy of 0.61 eV. The transport number is ca 0.99 in agreement with [119]Sn Mössbauer spectroscopic studies which show an isomer shift of 3.3-3.5 mm/s and a quadrupole splitting of 1.5-1.8 mm/s, characteristic of divalent tin with the lone pair of electrons being stereoactive and therefore non-conducting. The electrode reaction is controlled by the charge transfer process at temperature below 95 °C. The anodic and cathodic Tafel slopes are 60 to 70 mV/decade. Thermodynamic studies show that the products have $\Delta H = -69900$ cal/mol, $\Delta S = 69$ cal/mol,deg and $\Delta G = -49300$ cal/mol.

ACKNOWLEDGEMENTS

TABLE OF CONTENTS

LIST OF TABLES

ix

LIST OF FIGURES

SYMBOLS

σ - conductivity $(\Omega\text{-cm})^{-1}$

σ_o - pre-exponential factor in Arrhenius equation

ω - angular frequency

ϕ - phase angle which corresponds to phase difference between applied sinusoidal voltage and resultant sinusoidal current

μ - mobility $(cm^2/ V\text{-sec})$

ν-   - jump frequency

ρ - density (g/cm^3)

ρ_c - theoretical density

ρ_m - measured density

$\gamma_\pm$ - activity coefficient of the activated complex

η - overpotential

θ - Bragg angle

λ - wavelength

A   - area (cm^2)

a_o - activity

B   - line broadening due to small particle size, in radians

B_s - linewidth at half height for a well crystalline standard

B_m - linewidth at half height for the sample

c   - concentration (mole)

c^b - bulk concentration (mole)

c^o - observed concentration (mole)

D   - diffusion coefficient $(cm^2 s^{-1})$

D_o - frequency factor

E_g - energy gap (eV)

E_a - activation energy (eV)

e   - charge on the electron

F   - Faraday constant

f   - frequency (Hz)

G   - Gibb's free energy

Im   - amplitude of sinusoidal current

j   - flux (mole cm^2 s^{-1})

k   - Boltzmann's constant

l   -distance between two electrodes

M   - molecular weight

m   - mass of one unit cell

N   - Avogadro's number

n   - mole fraction in reaction mixture

P   - pressure

Q   - heat capacity

Q   - total charge flowing

S   - entropy

T   - temperature (°K)

t   - average particle diameter(Å)

t   - time (sec)

U   - internal energy

u   - chemical potential

V   - measured voltage

Vm   - amplitude of applied sinusoidal voltage (volt)

Va   - applied voltage

v   - volume (cm^3)

W   - work

x   - distance from the electrode (cm)

     - thickness of the diffusion layer

x_v - mole fraction of anion vacancies

Z   -number of molecular formulas per unit-cell

Z'   - real part of impedance

Z"   - imaginary part of impedance

Z_t - total impedance

Z_{cell} - cell impedance

CHAPTER 1.

INTRODUCTION

A large number of solids have ionic conductivity comparable to that of molten salts and are referred to as "fast ionic conductors" or "solid electrolytes". In recent years these materials have simulated considerable interest. From the technological point of view, solid electrolytes have many potential applications in batteries and other electrochemical devices. Among solid electrolytes, fast fluoride ionic conductors have become a research field of growing importance. Indeed, materials with very good electrical performances have been isolated, with particular emphasis on materials crystallizing in the fluorite structure type, as models of fast ion conductors due to their relative structural simplicity and availability as large single crystals. Such materials have proved to be useful for thermodynamic measurements, specific electrodes, solid-state batteries, electrochromic device, gas sensors, etc.

Fluoride ions are predicted to be the best anionic conductors because they are univalent, light and have a small ionic size. Furthermore, these materials are very often electronic insulators having band gaps of at least several electron-volts. Accordingly, the electron and hole concentrations in the electrolytes are extremely small, an essential property for their use as electrolytes in electrochemical batteries [1,2]. The work reported in this thesis is concerned with the preparation and characterization of fluoride conductors based on the fluorite-type structure and the investigation of some of their properties. The fluorite structure (Fig 1-1 a) [3] consists of a simple cubic lattice of anions with the cations situated at centers of alternate cubes. The unoccupied cube centers are believed to be the key to the defect and diffusion properties of these materials. It is thought that the anion sublattice disorders, with anions leaving their lattice sites and moving to interstitial locations at or near these cube centers, thus forming Frenkel defects, which consist of a combination of interstitials and vacancies. It has been suggested that the best fluoride conductors would be non-stoichiometric phases involving a cation with high polarizability and a structure deriving from the fluorite type [4]. In other words, a significant number of fluoride ions leave their normal position to

(b)

(O: F_I, •: Ca, x: V_{FII})

(a)
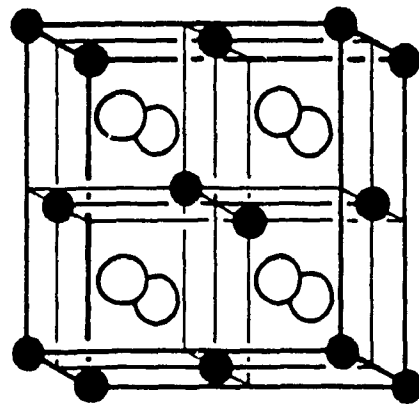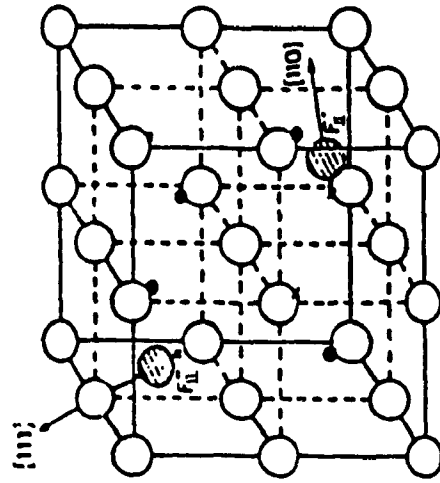
(O: F, •: Ca)

Fig. 1-1 (a) Fluorite-type Structure
(b) Frenkel Defects in the Fluorite-type Structure

go to interstitial positions. Examples are $Pb_{0.88}In_{0.12}F_{2.12}$, $Pb_{0.75}Sb_{0.25}F_{2.25}$ and $Sr_{0.69}La_{0.31}F_{2.31}$ [5,6]. Figure 1-1 (b)[7] shows a Frenkel defect in the fluorite-type structure with anions at normal sites (named F_i) and the cations occupying only half of the octacoordinated sites. The excess F^- ions are located in interstitial sites (F_{II}).

Transport number measurements [8] and diffusion studies [9,10] show that, as the temperature is increased, the cation sublattice remains nearly perfect while the anion sublattice becomes highly disordered. By doping with impurities, it is known that Frenkel defects are dominant and further that the anion vacancies are more mobile than the interstitial anion [11,12].

It has been reported [13] that the addition of strontium (2+), barium (2+) or lead (2+) ions to an aqueous solution of tin (II) fluoride results in the immediate precipitation of crystalline metal (II) trifluorostannate(II) phase, $M(SnF_3)_2$. The same authors report that similar reactions with Ca^{2+} result in an amorphous solid with a variable composition. In the case of lead(II), the structure of the product obtained, $PbSnF_4$ [14], cannot be written as $(PbF)+(SnF_3)^-$, the way suggested by Donaldson and Senior [13]. The compounds $BaSnF_4$ and $SrSnF_4$ cannot be obtained by the precipitation method. However, they can be prepared by solid state reactions at high temperature followed by quenching [15]. The preparation of the calcium and barium derivatives investigated in this study, with a description of the characterization techniques will be discussed in chapter 3.

The total conductivity of solid electrolytes consists of contributions from ionic and electrical motion. The conduction by electronic and ionic defects as well as the motion mechanism will be described in the chapter 2. A.C. impedance measurements are used to separate the ionic conductivity of bulk material from intergranular effects and the theory behind this is described in chapter 4, which also contains the electrochemical theory, the electrode kinetic theory, thermodynamic theory and practice for characterization. In chapter 5 and 6, the experimental results will be discussed. The major conclusions of this research are presented in chapter 7.

CHAPTER 2.

CHARGE TRANSPORT IN SOLIDS

In solids, the diffusion of electrons always occurs, but, in ionic crystals, the motion of ions also contributes to the total conductivity due to the displacement of their ionic charge. Thus solids are either ionic conductors or electronic conductors depending on the transport number, t, and the mobility μ of the charge carriers. (t_e and t_i are the transport numbers of electron and ionic species respectively and, $t_e + t_i$ = 1 by definition). A good ionic conductor has a high ion mobility and $t_i \approx 1$.

2.1. Ionic Conduction

The interest in the fluorite-type structure is due to the high fluoride ion mobility in these materials which leads to high ionic conductivity. Included in this class of materials are numerous compounds where fluoride ions are the mobile species, such as CaF_2, BaF_2 and PbF_2, although they are poor conductors (σ about 10^{-13} $\Omega^{-1}cm^{-1}$ at 25 °C).

X-ray diffraction experiments have shown that the structure is crystalline with the general ordering of the ions situated on regular lattice sites. However, to explain the motion of ions, the presence of some disorder is necessary. Figure 2-1 show the schematic diagram of diffusion mechanisms [16]. The important and most widely used models of disorder were proposed by Frenkel and Schottky. Frenkel's model is based on the assumption that some atoms might jump from normal lattice sites to unoccupied interstices. Based on this assumption, an interstitial ion may jump from interstice to interstice, Fig. 2-1(a), or push an ion from a regular site to an interstice (Fig. 2-1 (b)). In contrast, Schottky's suggestion is that some ions can jump from their normal lattic sites onto the surface of the crystal resulting in unoccupied sites or "vacancies" which can then participate in a number of diffusion mechanisms. This gives rise to the so called "vacancy mechanism" in Fig. 2-1(c). Another mechanism based on defects is the "ring mechanism" [Fig. 2-1(d), (direct exchange between two or more ions)], however, this process is not probable in ionic crystals. In the
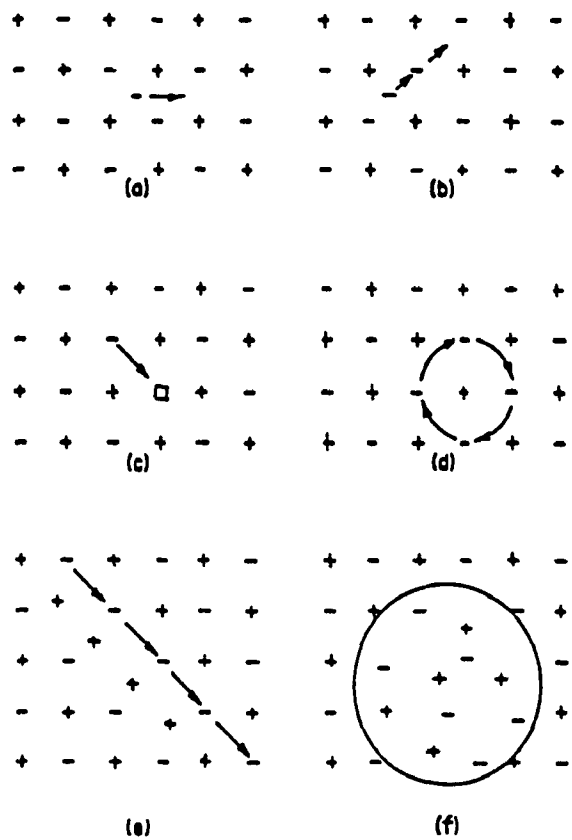
Fig. 2-1. Types of Defects and Jump Process

case of ionic crystals, "crowdion mechanism" (Fig. 2-1(e)) and "relaxion mechanism" (Fig. 2-1(f)) in which defects involving several disordered ions have been suggested. In the crowdion mechanism, several disordered atoms are in a row and in the relaxion mechanism disordered atoms are involved in a small volume.

The ionic conductivity is given by

$$\sigma = \sigma^- = eN\mu^-X^-$$

Where the σ is the ionic conductivity, e is the electronic charge, N is the number of molecules per unit volume and X^- is the mole fraction of anion. The mobility μ^- is directly proportional to the jump frequency v^-. Thus the conductivity, which is the directly obtainable quantity, depends on the defect concentration and the jump frequency. The conductivity also strongly depends on temperature, and the size of the mobile ion. At an optimum size, the activation energy would be low [17].

In ionic crystals the motion of ions under the influence of an external electric field creates a net ionic current. Experimentally, it is often found that the ionic conductivity can be described by an Arrhenius relation

$$\sigma^- = eN\mu^-X^- = \sigma_0 \exp\left(-\frac{E_a}{kT}\right)$$

In the situation of intrinsic conduction, the both ion mobility and concentration are temperature dependent. So the equation can be rewritten as

$$\sigma T = \sigma_0 T \exp\left(-\frac{E_a}{kT}\right)$$

where the T is absolute temperature, σ_o is the pre-exponential factor, $\sigma_o = Ne^2 a^2 v/kT$, E_a is the activation energy, k is the Boltzmann's constant. The ionic conductivity is multiplied by the absolute temperature in order to remove the factor of 1/T that appears in the pre-exponential factor; a plot of log(σT) versus 1/T gives straight line if the thermally-activated conduction obeys the Arrhenius law, and the slope of the line gives E_a.

Ionic conductors show a wide range of conductivities from 10^1 to 10^{-20} $(\Omega.cm)^{-1}$ at room temperature

[18] (Table 2-1). The electrical properties of ionic conductors can be explained on the basis of diffusion though a matrix of possible sites. Fast ion conduction involves a crystal structure which facilitates this migration.

The significance of the fast ion conductors is that solid electrolytes are available which at room temperature exhibit ionic conductivity comparable to that of liquid electrolytes. Their useful ionic conductivity values can be achieved over a wide range of temperature and ambient conditions, and a wide variety of ions are available as conducting species in solids.

Table 2-1. Conductivity of Some Solid Electrolytes

Ag^+ Electrolytes	Conductivity $(\Omega.cm)^{-1}$	Na^+ Electrolytes	Conductivity $(\Omega.cm)^{-1}$
$RbAg_4I_5$	2.4×10^{-1}	Na β'' alumina	10^{-2}
Ag_3SI	1×10^{-2}	NaCl	10^{-20}
AgI	2×10^{-6}	Plastic	10^{-20}
AgCl	3×10^{-8}	Glasses	$10^{-10} \sim 10^{-17}$

2.2. Electronic Conduction

In contrast to electronic conductivity, the motion of an electron through a periodic lattice is well described by Band Theory and materials are subsequently divided into metals, semi-conductors and insulators. In metals (Fig. 2-2 a) [19], the conduction band is partially occupied by electrons. In semiconductors, Fig. 2-2 b, the conduction band is partially populated at "higher" temperatures but is completely empty at "lower" temperatures, or the valence band contains "holes" (electron vacancies) at high temperature. In insulators, Fig. 2-2 c, the conduction band is essentially empty at all temperatures and the

7
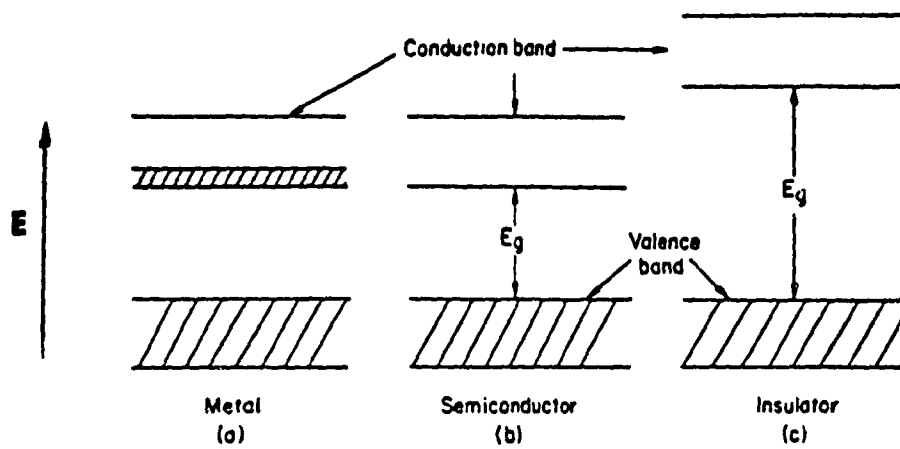
Fig. 2-2. Typical Band Diagrams Illustrating the

Differences Between Metals, Semiconductors,

and Insulators

valence band is full. The forbidden energy region between the valence band and the conduction band is called the "energy gap", "band gap" or "electron activation energy", E_g.

The formation of electron band energy in the solid can be considered using two different approaches: the interaction of localized electrons and their energy levels, and a collective or essentially free electron approximation. In terms of the band theory, the solid electrolytes or ionic crystals are insulators, so their band structure must consist of a full valence band separated from an empty conduction band by an energy gap. Free electrons do not participate in the normal properties of the solid electrolytes. However, free electrons are produced in the crystal by photons of sufficient energy and the electronic structure manifests itself in the photoconductivity of the crystal and the general interaction of the crystal with the exciting light. The electronic conductivity of the solid electrolytes can be expressed as

$$\sigma_e = ne\mu_e$$

where n is the number of free electrons, e is the electron charge, and the μ_e is the electron mobility.

As in the case of semiconductors, the number of free electrons in a solid electrolyte is temperature dependent. The number of conduction electrons n is given by

$$n = n_o \, e^{-E_g/kT}$$

where n_o is the concentration of atoms at the lattice sites, k is the Boltzmann constant. So

$$\sigma_e = (n_o \, e^{-E_g/kT}) \, e\mu_o$$

or

$$\sigma_e = A \, e^{-E_g/kT}$$

$$\log \sigma_e = \log A - E_g/2.303kT$$

The plot of $\log \sigma_e$ vs. $1/T$ should give a straight line with a slope of $-E_g/2.303k$. The measurement of σ_e as function of temperature will permit calculation of the electron activation energy and the transport number of solid electrolytes.

Since the solid electrolytes are never fully ionic conductors, it is necessary to determine both ionic and electronic components conductivity. The physical and electrochemical characterization of $MSnF_4$ (M= Ba, Pb, Ca) material will be discussed in following chapters.

CHAPTER 3.

PREPARATION AND PHYSICAL CHARACTERIZATION:

THEORY AND PRACTICE

The preparation of mixed fluorides in the CaF_2-SnF_2 system, and of $BaSnF_4$ will be described in this chapter. In order to characterize and investigate the physical properties of the fluoride ion conductors synthesized, X-ray powder diffraction, Mössbauer Spectroscopy and elemental analyses (atomic absorption spectrometry, fluoride ion electrode, UV spectrometry) were used. The theory behind these techniques will be described. To allow comparison to other MF_2-SnF_2 systems, relevant details to the preparation and characterization o˙ other M^{2+} compounds (M = Ba, Pb) will be discussed.

3.1. Materials Preparation

3.1.1. The CaF_2-SnF_2 System

The synthesis of compounds in the CaF_2-SnF_2 system was performed by precipitation reactions between α-SnF_2 and $Ca(NO_3)_2.4H_2O$ in aqueous solutions. Stannous fluoride, SnF_2, in the α-monoclinic form, was obtained from Ozark-Mahoning (97.5% purity) and calcium nitrate, $Ca(NO_3)_2.4H_2O$, from Fisher Scientific Company (99% purity). The reagents were used without further purification and the reactions were carried out in doubly distilled water. The use of further purified water did not yield significantly different results.

The 1.5 M calcium nitrate aqueous solution was added to the 1.5 M stannous fluoride aqueous solution at room temperature in different n values, where n is the molar ratio of calcium nitrate to the sum of calcium nitrate and stannous fluoride (n = Ca /(Ca + Sn)) used for the preparation (n = 0.05-0.8). The volume of the stannous fluoride solution was kept constant. Calcium nitrate was always added to the stannous fluoride solution at a constant of ca. 5 ml/min by use of a burette. Stirring of the mixture was controlled at a medium speed.

A white precipitate formed upon mixing of the two solutions. The product was filtered immediately after the end of the addition of the calcium nitrate solution. It was then washed with doubly distilled water and allowed to dry in air at room temperature.

3.1.2. $BaSnF_4$

The preparation of $BaSnF_4$ uses the "Bent Copper Tube" method designed by Denes [20]. Stannous fluoride was the same as used above and barium fluoride was obtained from Nichols Chemical Company Limited.

The reagents were mixed in a molar ratio 1:1. The copper tube reactor was cleaned with concentrated HCl, washed repeatedly with water, rinsed with distilled water, then with acetone to remove the water and dried by using a heat gun. Sample loading and sealing the Cu tube were carried out as described in [20]. One end of the tube was sealed by hammering and bending. Then the reagent mixture was put in the copper tube. The tube, loaded with the reagent mixture, was placed in a glove box under a nitrogen atmosphere for temporary sealing. This is necessary to avoid oxidation of tin(II) to tin(IV) and hydrolysis of the fluorides to oxides by residual moisture when the sample is heated. Then the tube was removed from the glove box and final sealing of the second end was performed by hammering and bending. The sealed copper tube was heated in an oven in two steps, first at about 200 °C for one hour, and then at 500°C for another hour. Then the tube was removed from the oven and allowed to cool to room temperature. Pre-heating the reagent mixture at 200 °C was carried out because of the low melting point of SnF_2 (M.P.= 215°C) and its high reactivity in the liquid state, which could give some reaction with residual H_2O, O_2 and even Cu after long exposure. However, because of the much lower reactivity of barium fluoride (M.P. = 1355°C), heating up to 500°C for one hour is necessary for a complete reaction to give $BaSnF_4$ as the only product. Despite all these precautions, a minor amount of Sn(IV) (1 to 2%) is found in the product, most of which is already present in commercial SnF_2 [20]. To avoid the presence of Sn(IV) in $BaSnF_4$, a small amount of Sn metal may be added to the reaction mixture. The product had a light greyish powder.

3.2. X-ray Powder Diffraction

3.2.1. Principles

W. L. Bragg (1913) found that one could account for the position of the diffracted beams produced by a crystal in an X-ray beam by a very simple model according to which X-rays are diffracted from various families of planes of atoms in the crystal. Although it is a diffraction phenomenon, it looks like a simple geometric reflection by a mirror, and as a result, the improper name "reflected beams" is often used. The diffracted beams are found for situations in which the X-ray scattered by the atoms contained in parallel planes interfere constructively to give a diffraction pattern (Fig. 3-1).

The unit-cell edges parallel to the reference axes are called a, b, and c. In a crystal, any plane can be identified by its Miller's indices (hkl), which are integer numbers defined as follows: the plane intersects the $\vec{a}$ axis at a distance a/h from the origin, the $\vec{b}$ axis at k/b, and the $\vec{c}$ axis at l/c. Each plane is repeated in neighbouring unit-cells and all the identical planes forms a "family" of (hkl) planes, which are parallel to each other and equidistant. The spacing between two neighbouring planes of the same family is called the "d-spacing", d_{hkl}. Each family of planes is equivalent to a grating and gives rise to diffraction with radiations the wavelength of which is of the same order of magnitude than the d-spacing. The path difference for beams diffracted by adjacent planes is $2d\sin\theta$. Reinforcement of the radiation diffracted from successive planes will occur when the path difference is an integral number n of wavelengths. The condition for constructive interference is that

$$n\lambda = 2d \sin\theta$$

or
$$n\lambda = 2d_{hkl} \sin\theta_{hkl} \quad \text{for the (hkl) family of planes,}$$

This is Bragg's law, and the diffracted beam are often referred to as "Bragg peaks".

A crystal consists of atoms arranged in a pattern that is repeated periodically in three dimensions. The space in three dimensions can be divided into identical elementary parallelepipeds. Repetition of these parallelepipeds by translation in the three directions of space generates a lattice. The generating

12
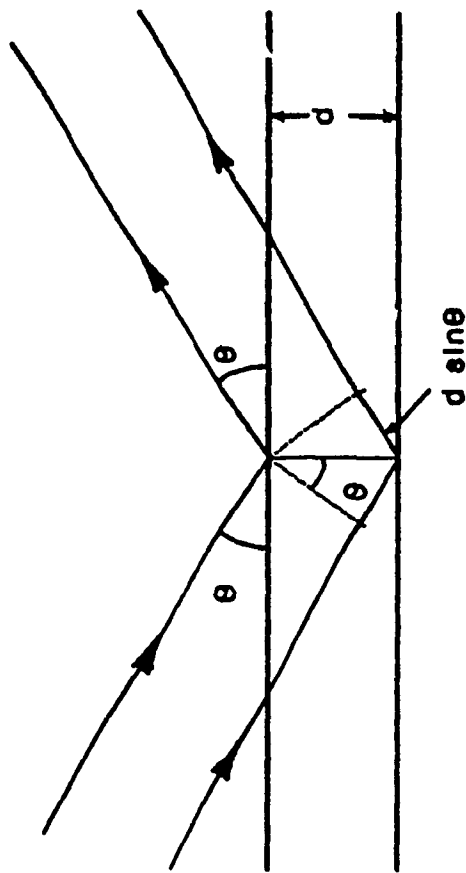
Fig. 3-1 Derivation of Bragg Law

$$2d \sin\theta = n\lambda$$

where d is the spacing between parallel atomic planes

parallelepiped is called a "unit-cell" [21]. The simplest kind of three-dimensional pattern is a set of points forming a lattice; each of these points is called a lattice point. Such a simplified pattern is called a "lattice array". A unit-cell is the smallest parallelepiped unit which expresses all the symmetry of the crystal structure and which, when repeated in three dimensions, ultimately make up a whole crystal. The size and shape of the unit cell is specified by the unit cell parameters a, b, c, α, β and γ, where the values a, b, and c are the lengths of the three edges of the unit cell, whereas α, β and γ are the angles between the edges (Fig. 3-2).

The X-ray powder diffraction method is very important for the characterization of solids. It is particularly useful in phase analysis because every crystalline material has its own characteristic pattern of Bragg peaks called "powder pattern". Two main factors determine the powder pattern of a crystalline solid, (i) the size and the shape of the unit cell determines the line position, and (ii) the atomic number and position of the various atoms in the cell determine the line intensity. Thus, it is highly unlikely that two materials have the same powder patterns unless they are isostructural and isoelectronic.

Other main uses of X-ray powder diffraction are:

(1) The line positions are related to the unit-cell parameters a, b, c, α, β and γ, which can be calculated from accurately measured Bragg peak positions, provided their indexation, i.e. their Miller's indices (hkl), are unambiguously known;

(2) Systematic absences of lines for some families of (hkl) planes give the symmetry elements that have a lattice translation, i.e. screw axes and glide planes;

(3) The line intensity gives the atomic positions (crystal structure) and texture (preferred orientation). The crystal structure is usually obtained from single crystal data, whereas the texture is obtained from polycrystalline samples;

(4) The line width gives the average particle size;

(5) The degree of crystallinity, presence of glasses, etc..., can also be obtained when appropriate.

The average particle size can be calculated using Scherrer's formula:
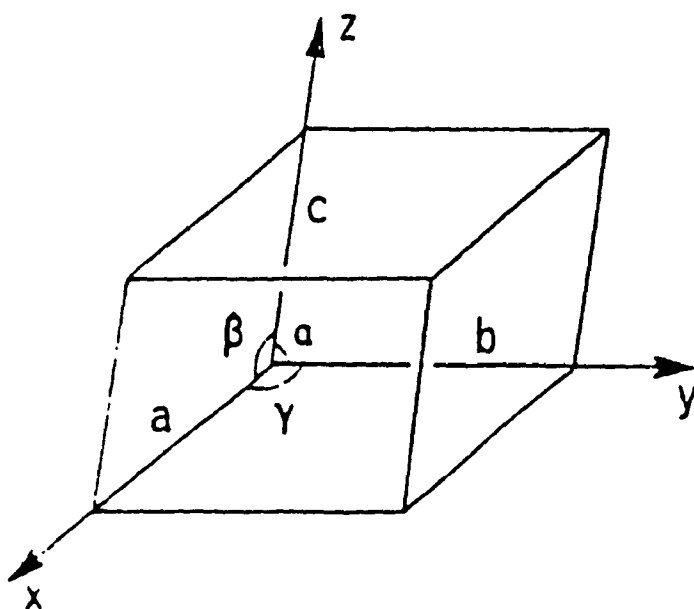
Fig. 3-2. Unit-cell Nomenclature

$$t(\text{Å}) = \frac{0.9\lambda}{B\cos\theta}$$

Where, t: average particle diameter (Å);

θ: Bragg angle;

λ: wavelength;

B: line broadening due to small particle size in radians, obtained from Warren's formula:

$$B^2 = B_m{}^2 - B_s{}^2 \qquad B \text{ in radians} = B\,(°\theta)\,\pi\,/\,180$$

B_s: linewidth at half height for a well crystalline standard (NaCl was used as standard because it is well crystalline, stable and, has peaks in the same θ range as our samples but with no overlap)

B_m: linewidth at half height for the sample

The limitations of this method are: (i) instrumental broadening which usually precludes measurements for $t \geq 1000$ Å, and (ii) lines that are too broad be distinguished from background fluctuations, which places another limit at $t \leq 40$ Å. Therefore, only particles with 40 Å $\leq t \leq 1000$ Å can be measured.

3.2.2. Instrumentation

X-ray powder diffraction was carried out on a Phillips PW 1050-25 diffractometer, using the Ni-filtered Kα radiation of copper (λ = 1.54178 Å). The X-ray tube was powdered at 800W (40 mV and 20 mA), the CPS (counts per second) range was 4×10^2, the time constant was 1 second, and no zero suppression was used.

Figure 3-3 shows the geometry of diffraction for the Philips line focusing diffractometers [21]. The radiation diffracted in the plane of the page at a given 2θ angle is brought to an approximate focus on the circumference of a circle - the focusing circle - by positioning the sample surface tangent to the circle, the X-ray tube target and the receiving slit on the same circle. The sample surface bisects the diffraction angle 2θ in this case. The X-ray beam diffracted from the surface of the sample is focused into the receiving slit before entering the detector or counter. This assures strong and narrow Bragg peaks and a weak

16
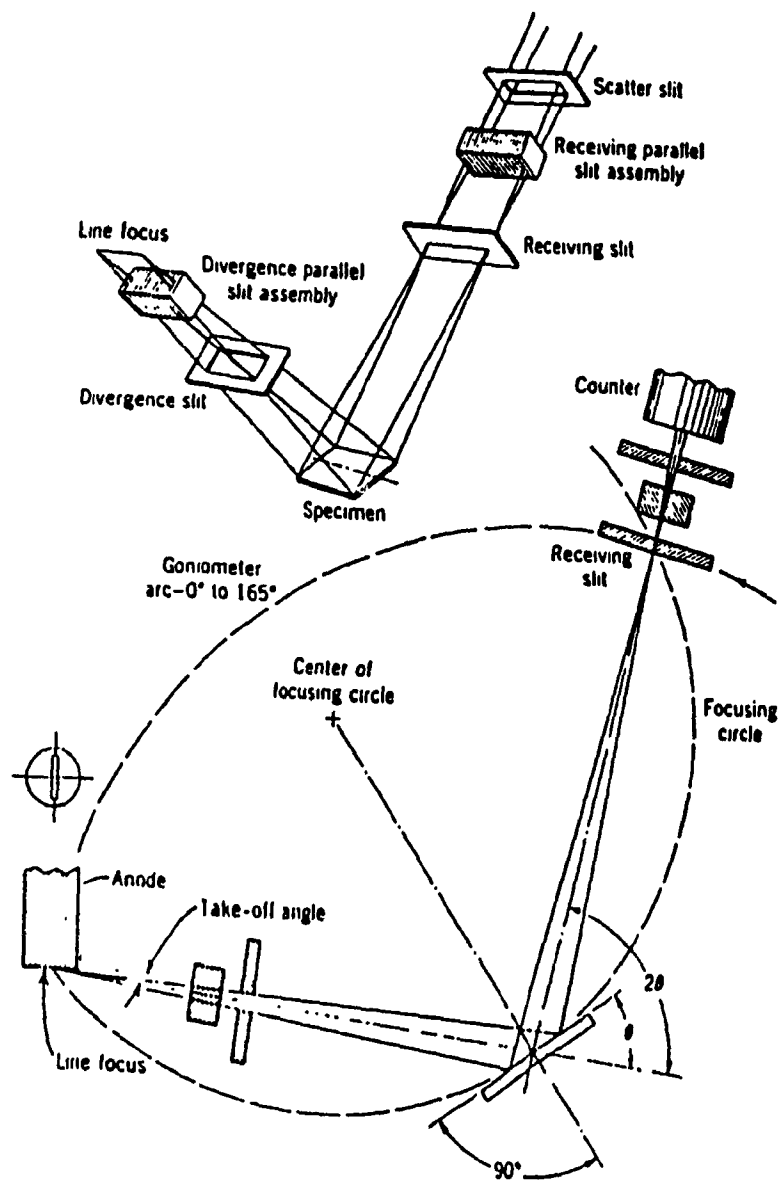
Fig. 3-3 A Schematic Arrangement of the Line Focusing X-ray Powder Diffractomer

· background.

The angular range required to obtain the desired diffraction pattern is scanned by rotating the counter at a constant speed ($0.5°(\theta)$ per minute). In order to maintain the geometry of the focusing circle, the sample is geared to rotate about the same axis at half the speed of the counter. The detector is a Xe/CO_2 scintillation counter. After detection, the signal is amplified and analyzed in a pulse height analyzer, then sent to a recorder, as a measurement of intensity versus diffraction angle θ, on a strip chart recorder. At the very end of this work, the diffractometer was automated with the Sietronics Sie112 system. The patterns were recorded in the step scanning mode, at an angular speed of $0.5 °(\theta)$ mn^{-1}, in the angular range 3 to $35°(\theta)$.

3.2.3. Experimental

In the X-ray powder method, the sample to be examined must be a fine powder and placed in a beam of monochromatic X-rays. Each crystallite, i.e. each particle of the powder, is a small single crystal oriented at random with respect to the incident beam and with respect to other crystallites.

Each sample was manually ground to a fine powder by a mortar and pestle and put in a sample holder, whose area is 2 cm^2, by pressing with a glass slide to form a flat smooth surface which is placed on the focusing circle at the center of the diffractometer. Preferred orientation is enhanced by the pressure applied to the powder to form a smooth flat surface. Preferred particle orientation is often difficult to control, and it strongly affects relative peak intensities, therefore, it must always be kept in mind when assessing peak intensities. The size of the particles in the powder is also an important parameter. If the size of the crystallites is small (ca<1000 Å), broadening of the peaks occurs as explained above, and in extreme cases (< ca. 40 Å), no diffraction pattern is observed. Surface roughness may also have a marked effect on relative peak intensity and their position since a part of the sample is shifted from the focusing circle.

3.3. Mössbauer Spectroscopy

A Mössbauer spectrum provides a picture position and splitting of the nuclear energy levels; the

18

Mössbauer parameters obtained are called chemical isomer shift and quadrupole splitting. The principles of Mössbauer spectroscopy and spectrum accumulation as well as the instrumentation will be discussed in the following sections.

3.3.1. Principles of Mössbauer Spectroscopy

The Mössbauer effect is the resonant emission of a γ-ray photon by a γ-ray source and its reabsorption in a solid matrix called "absorber", without loss of energy due to nucleus recoil and without thermal broadening. It provides a means of eliminating the destructive effects of the recoil and thermal energies. Its unique feature is in the production of monochromatic γ-radiation with a very narrowly defined energy spectrum, so that it can be used to resolve minute energy differences.

The primary decay of the parent radioactive nuclide produces a nucleus which is in a highly excited state. The latter then de-excites by emitting a series of γ-ray photons until by one or more routes, depending on the complexity of the γ-cascade, it reaches a stable ground state.

A Mössbauer spectrum gives a picture of the way the nuclear energy levels are disturbed by the nuclear environment, i.e. valence electrons and surrounding atoms. The purpose of our applications was to measure the Mössbauer parameters, chemical isomer shift δ and quadrupole splitting Δ (Fig. 3-4) [22]. Another important parameter, not relevant to our materials, is the effective magnetic hyperfine field acting at the nucleus. The electron density at the nucleus, which determines the isomer shift, is due to s-electrons only. Only those nuclear states with $I > 1/2$ have a nuclear quadrupole moment and hence show a quadrupole splitting (I is the nuclear spin) because of the interaction of the nuclear quadrupole moment Q with the electric field gradient (e.f.g.) acting at the nucleus in the case of non-spherical distribution of electric charges around the nucleus. Therefore, the chemical isomer shift δ gives information on the s valence electron density, the oxidation state, spin state and electronegativity of the ligands. The quadrupole splitting gives information on the electronic structure due to p, d and/or f electrons, i.e. oxidation state and spin state, bonding properties and local symmetry. In the case of tin-119, the nuclear transitions $\pm 1/2 \rightarrow \pm 1/2$ and $\pm 1/2 \rightarrow \pm 3/2$ result in two lines of equal intensity and equal linewidth, if $\Delta \neq 0$ and one line only if $\Delta = 0$.
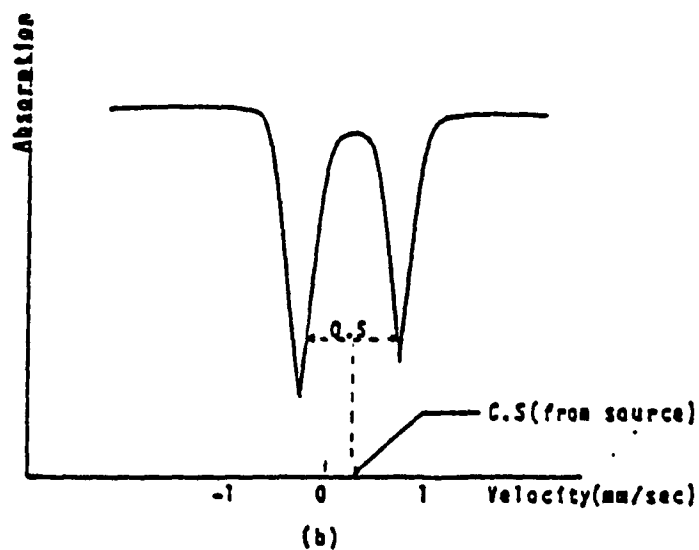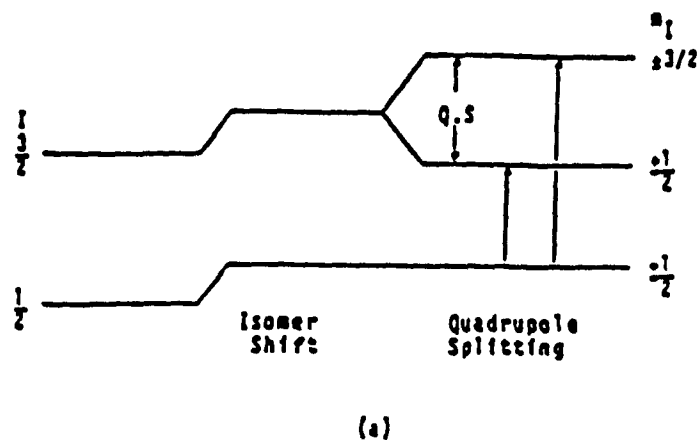
Fig. 3-4 Nuclear Energy Levels, Isomer Shift and Quadrupole Splitting

(a) Absorber energy levels.

(b) Resultant Mössbauer spectrum.

However, in some cases, the two lines can have non equal intensities and their relative intensity contains information about the state of the tin nuclei in the sample:

(i) Texture effect, i.e. preferred orientation, in polycrystalline samples, give an asymmetric doublet (the same is true for single crystals) and the asymmetry of the spectrum can give the relative orientations of the γ-ray beam and the direction of the main axis V_{zz} of the e.f.g.;

(ii) The Goldansii-Karyagin effect: this is due to the anisotropy of thermal vibrations of the tin nucleus, and its gives information about the directional thermal vibration and thus the strength of bonding as a function of direction;

(iii) Imperfect overlapping of two quadrupole doublets: if the amplitude of one line is higher than the other, the other should be broader, and therefore this is easy to distinguish from (i) and (ii) which give two lines of same width. Texture effects and Goldanskii-Karyagin can be difficult to distinguish from another.

Another important Mössbauer parameter is the recoil-free fraction of each tin site, i.e. the fraction of tin-119 nuclei that absorb a recoilless γ-photon resonantly, i.e. without transfer of energy to the vibrational levels, and therefore give rise to the Mössbauer absorption line(s). For the same quantity of tin-119 nuclei in a sample, a high recoil-free fraction will give a strong spectrum, whereas a small recoil-free fraction will give a weak spectrum. Strong bonds (ex: SnO_2) will give a high recoil-free fraction, weak-bonds (ex. SnF_2) will result in a lower recoil-free fraction. The recoil-free fraction decreases as temperature increases, due to increasing thermal vibrations.

3.3.2. Instrumentation

3.3.2.1. Principles of Spectrum Accumulation

The Mössbauer absorption spectrum is a record of the transmission of resonant γ-rays through an absorber as a function of the Doppler velocity, with respect to the source. The measurement of a Mössbauer spectrum is almost exclusively carried out by repetitively scanning the whole velocity range required, thereby accumulating the whole spectrum simultaneously, and allowing continuous monitoring of the
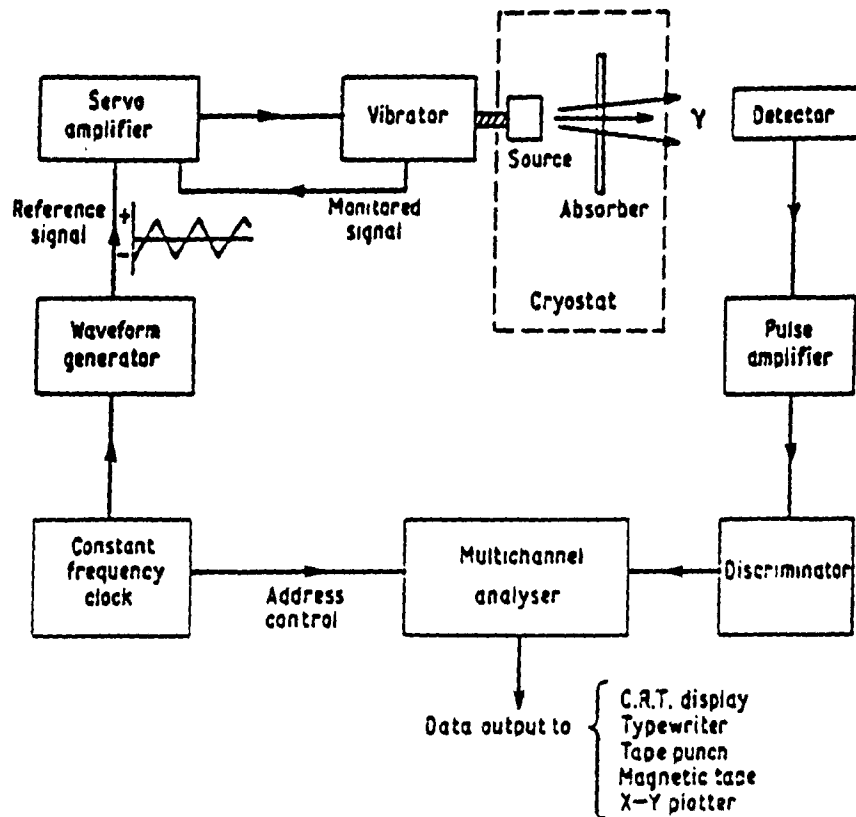
Fig. 3-5. A Schematic Arrangement for a Mössbauer Spectrometer

resolution. This can be achieved electro-mechanically, and a typical modern Mössbauer spectrometer is illustrated schematically in Fig. 3-5 [23].

The major component is the multichannel analyzer, which can store an accumulated total of γ-counts, using binary memory storage like a computer, in one of several hundred individual registers known as channels. Each channel is held open in turn for short time interval of fixed length, which is derived from a very stable constant-frequency clock device. Any γ-counts registered by the detection system during that time interval are added to the accumulated total already stored in the channel. The timing pulses from the clock is used to synchronize a voltage waveform, which is used as a command signal to the servo-amplifier controlling an electromechanical vibrator usually called "transducer". The latter moves the source relative to the absorber. A waveform, with a voltage increasing linearly with time, imparts a motion with a constant acceleration in which the drive shaft and the source spend equal time intervals at each velocity increment. The multichannel analyzer and the drive are synchronized so that the velocity changes linearly from -v to +v with increasing channel number. In this way the source is always moving at the same velocity when a given channel is open and the counts registered into any given channel always correspond to the same velocity of the source.

The geometric arrangement of the source, absorber and detector are important since the angle θ between emitted γ-ray and the axis of motion of the source creates the "cosine-effect", which causes a spread in the apparent Doppler energy, thus resulting in line broadening. The way of reducing this effect is adequate separation between source and detector. When a high energy γ-ray source (E_γ > 30 keV) is used, the source and absorber are cooled in a cryostat to liquid helium temperature as shown on Fig. 3-5. However, the recoil free fraction of tin-119 (E_γ = 23.8 keV) is usually high enough such that all our experiments were carried out with both the source and absorber at ambient temperatures.

3.3.2.2. Instrumentation Used

A Harshaw (Tl)NaI scintillation detector was used in our [119]Sn Mössbauer spectroscopic study for its high efficiency for the 23.8 keV radiation of tin-119. The pulses are amplified, passed through a

discriminator which rejects most of the nonresonant background radiation, and are finally fed to the open channel address.

One of the most important experimental aspects is in the choice of a source matrix. It is very desirable to have a high recoilless fraction and a single emission line unbroadened by hyperfine interactions and lattice defects. The γ-ray source in this work for ^{119}Sn Mössbauer spectroscopy was a 15 mCi $Ca^{119m}SnO_3$ pellet supplied by Amersham. The Doppler velocity was obtained using an Elscint driving system working in the constant acceleration mode (triangular waveform). All spectra, taken at room temperature and were accumulated in a quarter of a 2K Tracor Northern 7200 multichannel analyzer operating in the multiscanning mode. After accumulation, the data were transferred to an IBM compatible computer and saved on a diskette. About 300-500 mg sample was used (depending on the content of tin in the sample) and pressed in a Teflon holder with a tight fitting cap. Isomer shifts were referenced to $CaSnO_3$ at room temperature as velocity zero.

3.4. Chemical Analysis

3.4.1. Atomic Absorption Spectrometry

3.4.1.1. Principles

Atomic absorption spectrometry is based on the measurement of the absorption of the resonance radiation by free atoms in the gaseous state, i.e. of spectral lines corresponding to the transition of atoms between the ground and excited states. When the solution of the metal to be titrated is aspirated into a flame, the sample element is converted to atomic vapour. The ground state atoms in the vapour can absorb radiation given by a special source made from that element. This work used the wavelength range where the absorption follows Beer's law, that is, the absorbance is proportional to the path length in the flame and the concentration of atomic vapour in the flame, while the atomic vapour concentration in the flame is proportional to the concentration of the solution being aspirated.

3.4.1.2. Instrumentation

The requirement for atomic absorption spectrometry are a light source, a cell (the flame), a monochromator and a detector. A schematic diagram of dual beam atomic absorption spectrometer used in this study is illustrated in Fig. 3-6. for a system with a signal detector shared by both beams.

The source beam was alternately directed though the flame and around the flame by the chopper. After recombination, the two beam passed though a monochromator to a detector and readout system. The difference between the two beam was integrated over 3 seconds and then displayed.

The source, a hollow cathode lamp, is used for a special element since it emits the light at a specific wavelength. In other words, for the measurement of Ca(2+) and Sn(2+), the hollow cathode lamp for calcium and tin are used. A premix chamber burner is used in which the fuel and support gas are mixed before entering the burner head where combustion takes place. The sample solution is aspirated though a capillary by the "venturi effect" using the support gas for aspiration. Large droplets of the sample condense and drain out of the chamber. The remaining fine droplets mix with the gases and enter the flame.

The Ca(2+) and Sn(2+) analyses were performed using a Perkin Elmer Atomic Absorption Spectrometer Model 503. The sample solution was prepared by dissolving the sample in a 10% (v/v) HCl solution. The amount of sample used was between 100 to 200 mg depending on the M(2+) content, to bring the sample absorption into the linear range. The standard solutions were prepared using 1000 ppm stock solution of Sn and Ca diluting with 10% (v/v) HCl.

For analysis of Sn, a wavelength of 284.0 nm was used. A Cathodeon Ltd., Type c hollow cathode lamp was used as the source. To avoid the formation of solid SnO_2 in the flame, a nitrous oxide-acetylene reducing flame was used.

For Ca, the wavelength was 342 nm. A Cathodeon Ltd. hollow cathode lamp was used and the flame, air-acetylene, was oxidizing. Subsequent standard solutions of 100, 200 and 300 ppm for tin and 2, 3 and 5 ppm for calcium were run. The absorption of tin standard solution and calcium standard solution as well as standard curve calculations are listed in Tables 3-1 and 3-2. By interpolation, the Sn(2+) and Ca(2+) concentrations in the samples (in ppm) were obtained from their absorbance.

25

power supply | hollow cathode lamp

rotating chopper

J_0

burner

fuel

sample

compressed air

monochromator

detector & amplifier

meter

J | j
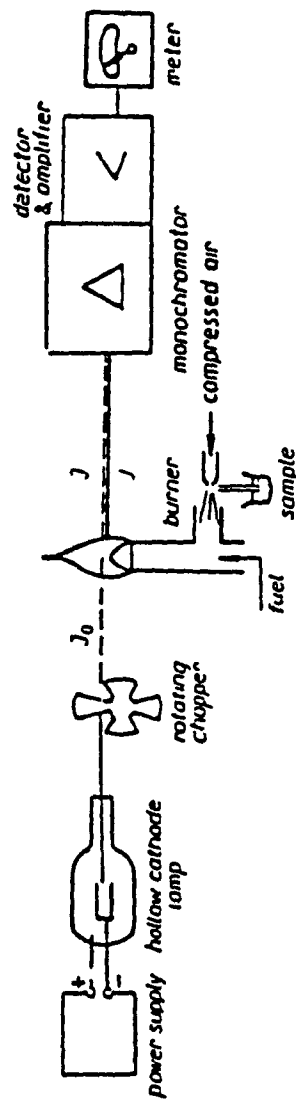
Fig. 3-6 Schematic Diagram of an Atomic Absorption Spectrometer

J_0 — modulated light beam from a hollow cathode lamp, J — the beam after absorption in the flame, j — unmodulated light emitted by the flame

3.4.2. F⁻ Analysis

Fluoride ion analysis was carried out using a model 94-09 fluoride ion selective electrode manufactured by Orion Research Laboratories, and a digital pH meter built at the Concordia University Science Technical Centre. The pH meter is switched to its mV position and all readings are in millivolts. Equal volumes of the sample solution and buffer solution, TISAB II, were mixed and then a reading was taken using the fluoride electrode. The TISAB II (Total Ionic Strength Adjustor Buffer) was added to provide a constant background ionic strength and adjust the solution pH. TISAB II can be purchased or prepared in the laboratory as described in Appendix I.

Standard solutions in the range 1×10^{-1} to 1×10^{-4} M in F⁻ were made by dissolving NaF in 10% (v/v) HCl. The sample solutions were made by dissolving each powdered sample in 10% (v/v) HCl. Ten millilitres of sample (or standard) solution and 10 ml of TISAB II were mixed in a Teflon beaker, and then a millivolt reading was taken. Glass vessels are never used for this analysis because F⁻ etches glass. In order to verify that the pH meter was operating correctly, we controlled that a ten-fold increase in concentration of F⁻ resulted in an increase of 59 mV at 25 °C. This value is obtained from the NERNST equation,

$$E = E_0 - \frac{RT}{nF} \ln [F^-]$$

at 25 °C,

$$E = E_0 - 0.059 \log [F^-]$$

ie, at 25 °C and n=1 the slope of the NERNST equation should be 0.059 V/decade or 59 mV/decade.

In practice, the ten-fold increase in concentration of F resulted in an increase of 58 ± 1 mV at the working temperature (20-25 °C).

A potential of 511 (±2) mV for the 1×10^{-1} mole standard F⁻ solution, 452 (±1) mV for 1×10^{-2} mole, 393 (±2) mV for 1×10^{-3} mole and 335 (±2) mV for 1×10^{-4} mole standard solution was obtained. The calibration curve of mV versus F⁻ concentration was drawn on semi-log paper to give a straight line with a slope of 58 ± 1 mV/ mole. Interpolation was used to get the concentration of the sample solutions. With a sample

Table 3-1. Absorption of Tin Standard Solutions

Concentration	Absorption (Standard Deviation)
100 ppm	0.097 (±0.004)
200 ppm	0.228 (±0.004)
300 ppm	0.316 (±0.003)

Slope: 0.097;

Correlation Coefficient: 0.998;

Intercept: 0.006.

Table 3-2. Absorption of Calcium Standard Solutions

Concentration	Absorption (Standard Deviation)
2 ppm	0.090 (±0.003)
3 ppm	0.139 (±0.002)
5 ppm	0.226 (±0.003)

Slope: 0.045;

Correlation Coefficient: 0.999;

Intercept: 0.001.

weight of 100-200 mg, the F⁻ concentration was in the linear range of the electrode.

3.4.3. NO_3^- Analysis

NO_3^- analysis was carried out by the Ultraviolet Spectrophotometric Screening Method. The UV absorption spectrum is obtained by the spectroscopic analysis of the light transmitted by an absorbing medium which is placed between the light source and the spectrometer. When a molecule, which is in the ground state, absorbs UV radiation, its energy increases and electrons will be excited to a higher electronic level.

A Spectrophotometer of Fisher Scientifique Spectronic, Model 1001 was used at 220 nm and 275 nm with matched silica cells of 1-cm light path. The 150-250 mg unknown sample was dissolved in 10 % (v/v) HCl. The measurement of UV absorption at 220 nm enables rapid determination of NO_3^-. Because dissolved organic matter also may absorb at 220 nm and NO_3^- does not absorb at 275 nm, a second measurement made at 275 nm was used to correct for organic impurities. Acidification with 1 N HCl is designed to prevent interference from the carbonate ion which also absorbs at 275 nm. The standard nitrate solutions were prepared by dissolving potassium nitrate (dried in an oven at 105 °C for 24 h) in distilled water. Solutions with concentrations of 0, 10, 20, 30, 40, 50 (NO_3^-, µg/ ml) were measured to obtain the standard curve which followed Beer's law.

3.4.4. Bulk Density measurements

The bulk density was obtained using Archimedean's method of displacement in a liquid. The liquid used for measurements was CCl_4 because it is non-reactive and non-solvent for the powders being tested, and it has a low viscosity. The principle of this method is based on measuring the volume or weight of liquid, CCl_4, displaced by the powder. For this purpose, a specially designed apparatus and a modified analytical balance were used (Fig. 3-7). The sequence for a measurement is:

(1) measure the weight of the empty crucible, m_1;

(2) measure the weight of the empty crucible immersed in CCl_4, m_2; this is done in the special

29

Balance

V_1

V_2

Sample

CC14
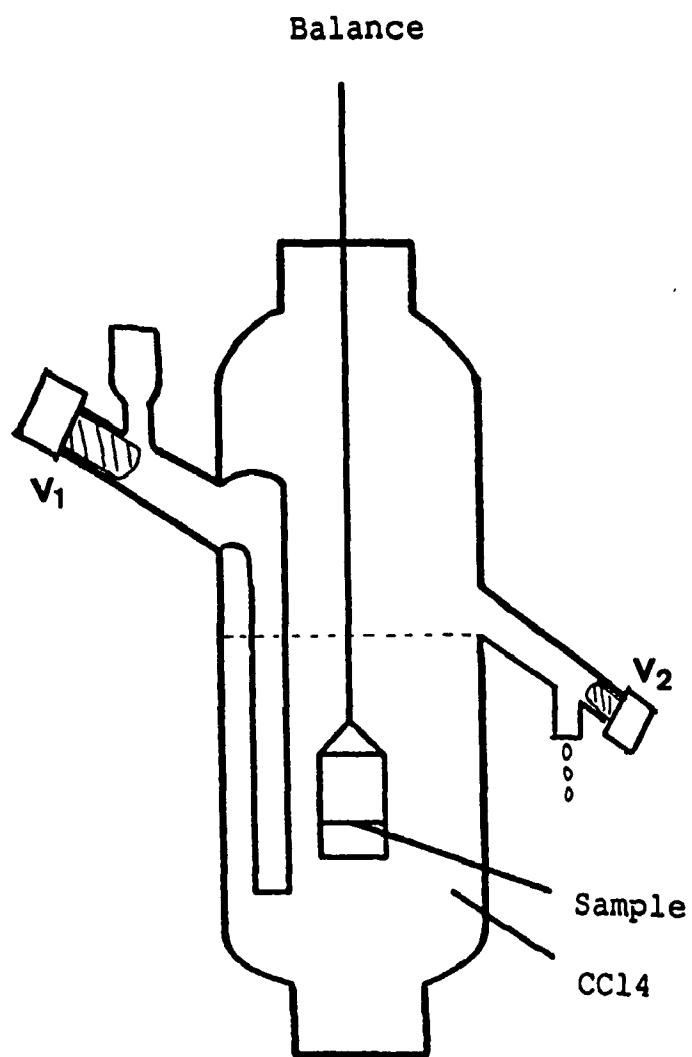
Fig. 3-7. Apparatus for Density Measurements

CHAPTER 4.

ELECTROCHEMICAL CHARACTERIZATION,

THEORY AND PRACTICE

As described earlier, the class of materials known as solid electrolytes are never fully ionic conductors although the ionic transport number t_i, usually approaches unity. It is, thus, necessary to determine the magnitude of both the ionic and the electronic conductivities; the relative proportions of which determine the transport number. The thermodynamic properties of the system are also important in determining the usefulness of the materials. These properties can be approximately measured by using electrochemical techniques. Finally it is necessary to determine the kinetics of the reactions which can occur at the electrode/electrolyte interfaces. It is the purpose of this chapter to discuss the theory and practice behind the electrochemical techniques used to perform this characterization.

4.1. Cell Design

The cell design used to carry out the electrochemical measurements is shown in Fig. 4-1. This design allows the electrochemical parameters to be measured as a function of temperature at a constant pressure. Thus the inner compartment is loaded with the electrolyte powder and two appropriate electrodes in the configuration shown (Fig. 4-1). A pressure is applied between the stainless steel cylinders which also act as current collectors. The screw arrangements at each end allow the cell to be removed from the hydraulic press without relaxation of the pressure. The cell is then placed in a furnace and the temperature dependence measurements carried out. This cell was operated in three modes (Fig. 4-2) depending on the type of measurement required. For routine ionic conductivity and approximate electronic conductivity measurements, two copper discs are inserted to act as ionically-blocking electrodes (Fig. 4-2 a). In contrast, to obtain more accurate values of electronic conductivity and to determine the thermodynamic properties, one of these copper electrodes is replaced by a tin electrode which is prepared 'in situ' by simultaneously

apparatus shown on Fig. 3-7;

(3) measure the weight of the crucible with the sample, m_3;

(4) evacuate the sample on a vacuum line for at least 30 minutes with a rotary and diffusion pumps, then immerse the sample still under vacuum in CCl_4 and measure the weight, m_4.

Since there is air trapped between the powder particles, evacuation is very important to remove the trapped air and the sample must be covered with CCl_4 while still under vacuum. In this technique, it is necessary to keep the CCl_4 level and temperature the same for the m_2 and m_4 measurements; the vessel shown on Fig. 3-7 ensures a constant level of CCl_4 and allows wetting the sample while still under vacuum, i.e. without letting air in the system. The density of the powder is then defined as

$$\rho = \frac{m}{V}$$

where $m = m_3 - m_1$

$$V = \frac{(m_3 - m_1) - (m_4 - m_2)}{\rho_{CCl_4}}$$

Since the volume of the sample is equal to the volume of CCl_4 it displaces, provided no air remains trapped between the particles, and since the density of CCl_4 is equal to its mass divided by its volume. It results that the density of the sample is

$$\rho = \frac{(m_3 - m_1)\, \rho_{CCl_4}}{(m_3 - m_1) - (m_4 - m_2)}$$

About 1-2g of samples were used. The zero of the balance was checked before each weighing. A reproducibility error of 0.1% - 1% was obtained. The density of CCl_4 versus temperature was taken from[24].

electrodes

stairless steel

teflon   sample

Fig. 4-1 CELL DESIGN

bridge

33
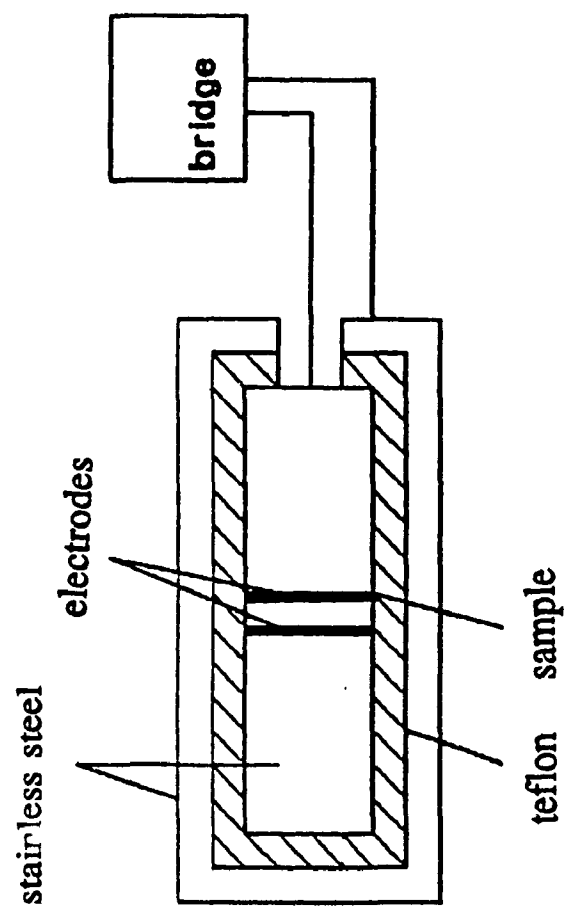
pressing tin powder into a disc (Fig. 4-2 b). This is theoretically an ionically non-blocking electrode but, in the mode used in these type of measurements, the tin electrode is always polarised so that the tin electrode is negative and no net ionic current can flow below the decomposition potential. (Essentially the copper electrode blocks the ionic flow.) To determine the electrode kinetics, a second symmetrical arrangement (Fig. 4-2 c) is used with two non-blocking, tin electrodes. The theory and practice behind these measurements are described in the following sections.

4.2. Conductivity Measurements

4.2.1. A.C. Methods

4.2.1.1. Theory

If an alternating voltage given by

$$V = V_m \sin \omega t$$

is applied to a pure resistance, then the resulting current through the resistance R follows Ohm's law:

$$I = \frac{V_m}{R} \sin \omega t = I_m \sin \omega t$$

If a sinusoidally time dependent voltage $V_m \sin \omega t$ is applied across the cell containing reactive components a sinusoidal current $I_m \sin(\omega t + \phi)$ will flow, where $\omega = 2\pi f$ (f is the frequency of the applied voltage), and ϕ is the phase angle. The impedance Z is defined by

$$Z = \frac{V_m}{I_m}$$

34

Cu | electrolyte | Cu

(a)

Ionically blocking, electronically
non-blocking electrodes

(-) Sn | electrolyte | Cu (+)

(b)

Ionically blocking, electronically
non-blocking electrodes
(when polarized with the tin as
the cathode)

Sn | electrolyte | Sn

(c)

Ionically and electronically
non-blocking electrodes
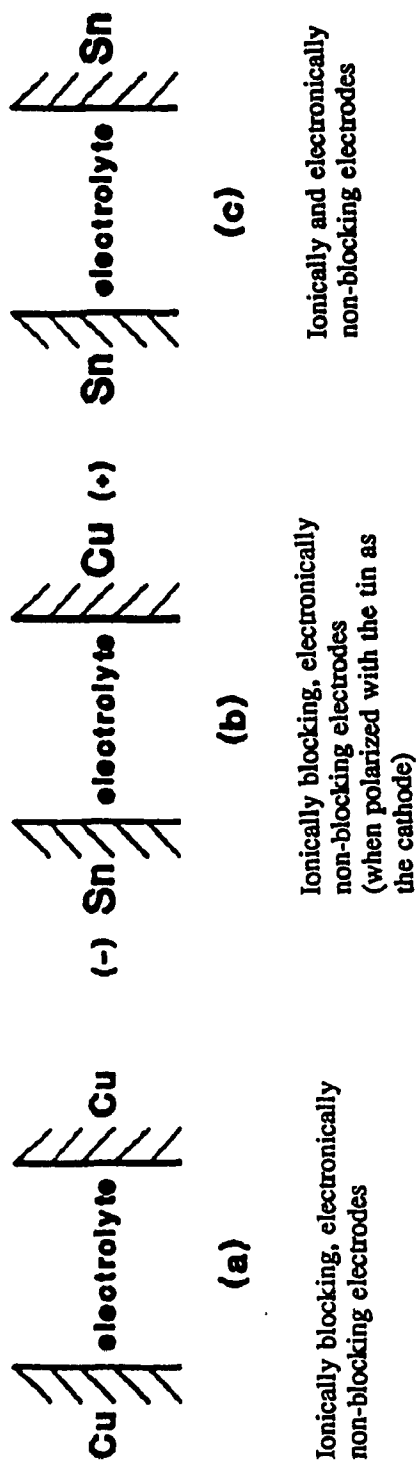
Fig. 4-2 CELL OPERATION MODE

$$Z' = |Z| \cos \phi$$

$$Z'' = |Z| \sin \phi$$

the Z' is the real part of impedance and the Z'' is the imaginary impedance. This is a vector quantity and can be represented by a point in the complex plane characterised by $|Z|$ and θ or by its real and imaginary components Z' and Z'', projected on the X and Y axes. Unless the cell is a pure resistance, its impedance is frequency dependent and an impedance spectrum is described in the complex plane. Figure 4-3 shows some simple equivalent circuits and their impedance spectra.

Typically a cell containing a solid electrolyte is represented by a more complicated equivalent circuit and yields a more complicated spectrum. It is the object of the investigator to find the appropriate equivalent circuit and to determine the size and significance of the individual components.

4.2.1.2. Experimental

The polycrystalline ionic conductors can be electrically characterised by measuring their impedance as a function of frequency and temperature. The A.C. impedance measurements are used to separate the ionic conductivity of bulk material from intergranular effects. The measurements were made of the complex impedance diagram at a frequency range from 100 KHz to 100 Hz. The data was taken and plot performed automatically using a Solartron 1174 Frequency Response Analyzer controlled by a Zenith P.C.

The A.C. impedance of $BaSnF_4$ and CaF_2-SnF_2 system were measured. Figure 4-4 shows the impedance spectra of $BaSnF_4$. These spectra suggest an equivalent circuit as shown in Fig. 4-4 (a), where R_1 is the electrolyte bulk resistance, R_2 the grain boundary resistance, C_1 the bulk capacitance, C_2 the intergranlar capacitance and C_3 the double layer capacitance. Theoretically, this circuit will produce the spectra as shown in Fig. 4-4 (b). Since in the dash line part the frequency required is too high to be measured with the available equipment. So the experimental spectra is obtained in the frequency of the solid line part (100 Hz - 100 KHz). The results show, in the $BaSnF_4$, $R_1 > R_2$. So the ionic conductivity is mainly due to the electrolyte.

The impedance measurements on CaF_2-SnF_2 system suggest that the system is in the circuit as shown

36
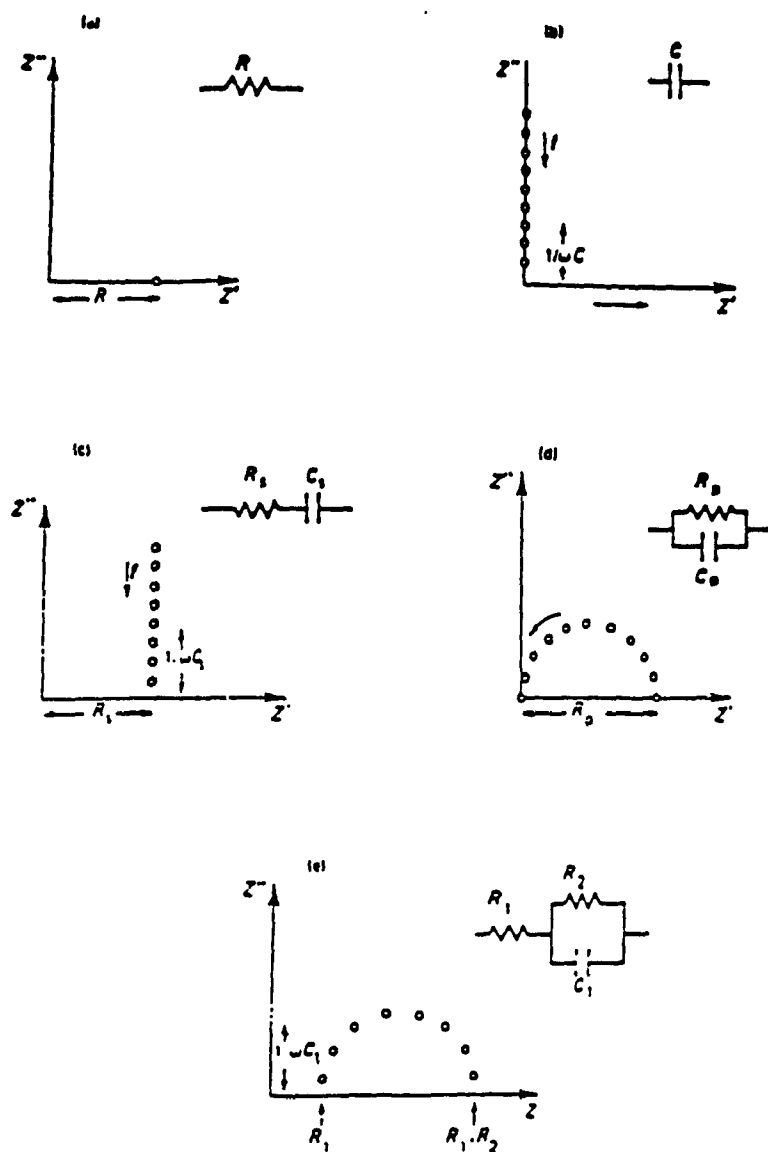
Fig. 4-3. Complex-plane impedance spectra with their

associated equivalent circuits

37

Z" IMAGINARY

T = 25 °c
f = 100 Hz-100 KHz

.100

.

.

.

.1k

.... .10 k

Z' REAL

z"IMAGINARY

f

f

Z' REAL
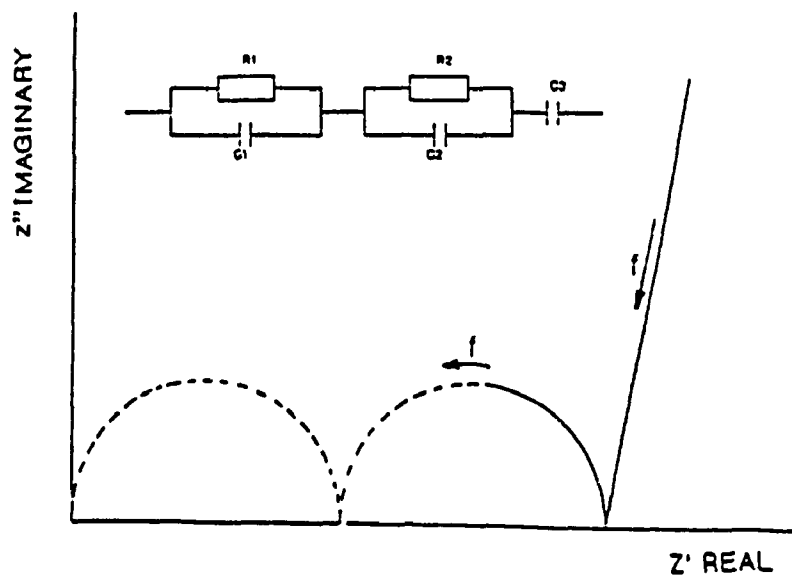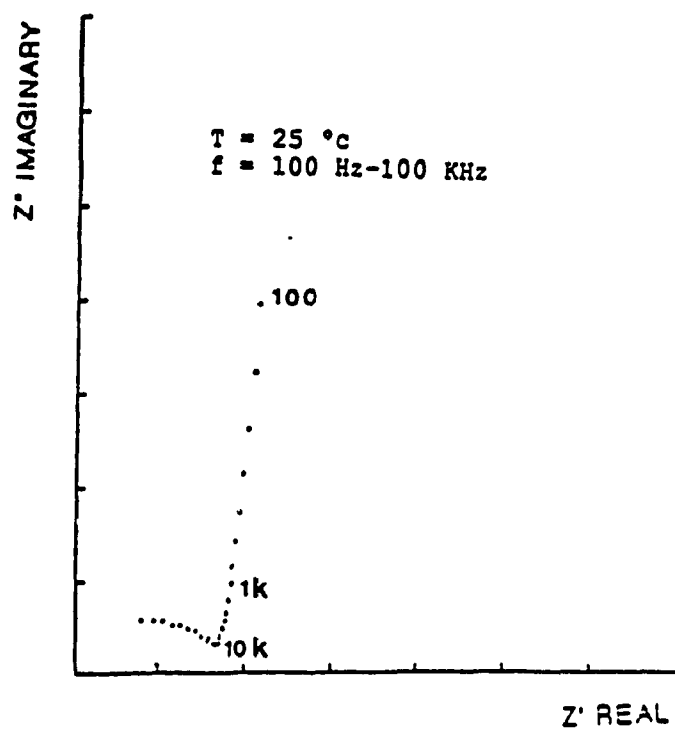
R1 = electrolyte bulk resistance
R2 = grain boundary resistance
C1 = bulk capacitance
C2 = Intergranular capacitance
C3 = double layer capacitance.

Fig. 4-4. Complex Impedance Plot of BaSnF4

38

in Fig. 4-5 (a). The theoretical spectra is shown in Fig. 4-5 (b). In the dash line part, the frequency required is too low to measured. So only the solid line part was measured. The impedance measurement results suggest that the bulk resistance of the system is much larger than the grain boundary resistance. So $R \sim R_1$. In other words, the ionic conductivity measured at 1kHz is again due to the electrolyte only. These results show that, although the compounds behave differently, the use of a single frequency Wheatstone bridge method described below is adequate for determining the ionic conductivity in these systems.

The bulk conductivity was calculated from the measured resistance and the dimensions of the sample determined after removal from cell. In general, the electrode area was 2.0 cm² and the thickness was about 0.1-0.2 cm.

4.2.2. Ionic Conductivity

Ionic conductivity measurements were carried out at a frequency of 1 kHz using blocking copper electrodes which blocked the ionic current flow, on a Fluke impedance bridge, Model-710B. The cell which used in the conductivity measurements shown in Fig. 4-1. The powder was contained between two stainless steel dies which fitted within a ceramic sleeve and pressed under 6000-12000 p.s.i pressure. This pressure was established by noting the minimum value required to give a sample resistance which was independent of pressure at any temperature (see chapter 6, Fig. 6-1. pressure dependence). The sample was heated in a furnace. The temperature of the sample was measured with a chromel-alumel thermocouple held against the ceramic sleeve, with a temperature controller being employed to maintain the temperature constant over any necessary period of measurement. The furnace calibration was carried out using a MICRONTA Auto-range Digital Multimeter. All the readings of resistance were taken at 30-45 minutes after temperature selection (see chapter 6, Fig 6-2. time dependence). The ionic activation energy was calculated from the straight line of the log σT vs. 1/T because it is expected that the concentration and the mobility of defects are temperature dependent (Note that plotting log σ vs 1/T would only result in a small difference in the measured activation energy over the temperature range employed).
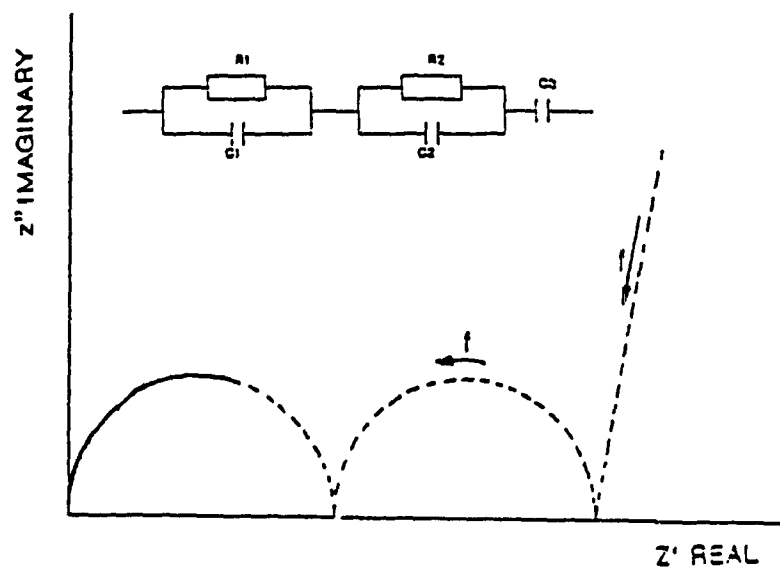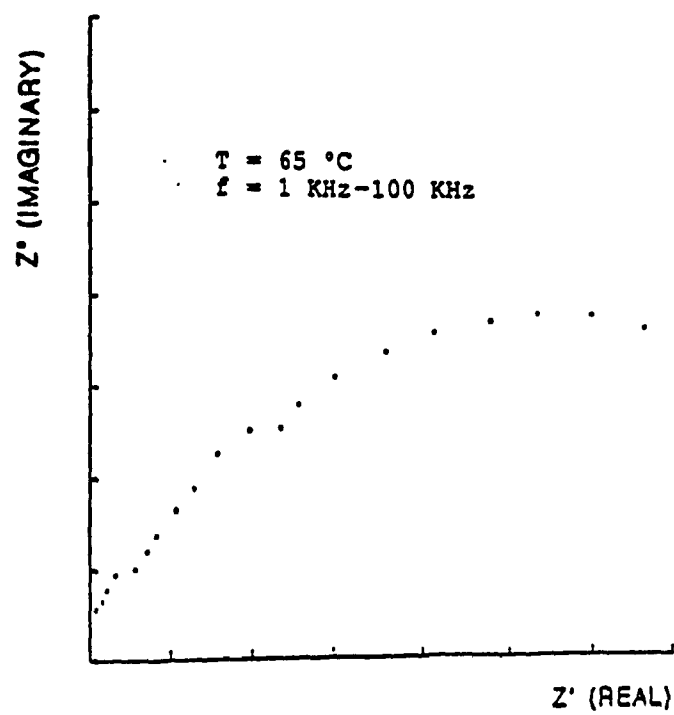
Fig. 4-5. Complex Impedance Plot of CaF$_2$-SnF$_2$ System

4.2.3. Electronic Conductivity

The electronic conductivity of a solid electrolyte can be determined in either of two ways. The polarization cell method and galvanic cell method. The polarization measurements offer one means of separating the electronic and ionic contributions to the total conductivity [25]. The measurement techniques involve an intelligent selection of electrode conditions to suppress either the electronic or the ionic part of the conduction.

4.2.3.1. Approximate Method

Using ionically-blocking electrodes an approximate value of electronic conductivity was obtained by measuring the I-V curve using a Princeton Applied Research polarographic analyzer, Model 364, with a constant potential scan rate of 5 mV/sec. The current was measured using a Fisher Y-t (Recordall Series 5000) recorder. The electronic conductivity was calculated from the resistance and the sample dimensions. this was used for routine analysis.

4.2.3.2. Polarization Cell Method

To obtain more accurate information, a number of samples were selected for determinations using Hebb-Wagner Polarization.

a. Hebb-Wagner Polarization

The time dependence of the concentration is given by Fick's second law:

$$\frac{\partial c}{\partial t} = D\frac{\partial^2 c}{\partial x^2}$$

and the flux,

$$j = -\frac{\sigma}{F^2}\frac{\partial \eta}{\partial x}$$

where η is the electrochemical potential, σ is the conductivity, c is the concentration and x is the coordinate respectively. The kinetic property of the cell is the fact that the current I passing through the cell is a measure of the flux j, ie. I= nFj.

Considering the boundary conditions:

$c(x=0, t) = c'$ at $t > 0$

$c(x, t=0) = c''$ at $0 < x < 1$

$(\partial c/ \partial x)_{x=1} = 0$ at $t > 0$

it follows that the electric current I at small times $(t << l^2/D)$ equals

$$I = \frac{\sqrt{D}Q}{1\sqrt{\pi t}}$$

where Q is the total charge flowing during the relaxation process and 1 is the distance between two electrodes.

For long times, $(t > l^2/4D)$

$$\log I = \log \frac{4eqD(c''-c')}{1} - \frac{1.071Dt}{1^2}$$

From the slope of the straight line in the I-1/√t or log I-t diagram the electron diffusion coefficient can be determined without knowing the concentration difference c''-c'. This will be used to determine the diffusion of the electronic conductivity.

The electron diffusion coefficient is proportional to the electron mobility. So that D can be expressed as

$$D = D^\circ\, e^{-Eq/kT}$$

This expression predicts that D depends exponentially on the temperature. D° is called the frequency factor and is independent of temperature.

b. Experimental

In this work, two electrodes, one copper electrode was used to block the ionic species, and a, tin electrode, was used to maintain unit activity by controlling the ionic strength of the system (Fig. 4-2 b). A current was passed through the cell with a positive external D.C. potential which is smaller than the decomposition potential of the electrolytes being examined. The cell arrangement is that of an electrolyte between a reversible and an ideally polarized electrode. Under these conditions, there is no voltage drop in the electrolyte, but a small electronic diffusion current is observed [26]. The electronic conduction was measured as a function of the temperature.

This work was carried out with a Hokuto Denko Ltd. GPIB Potentiostat / Galvanostat, Model HA-501 G. The output current was monitored using a Fisher recordall recorder, Series 5000. The diffusion coeffic-ient is obtained by plotting I vs. $t^{\frac{1}{2}}$ (Fig. 4-6) and then calculating the slope of the straight line. The electronic activation energy was calculated from the slope of the plot log D vs. 1/T.

4.3. Electrode Kinetics

4.3.1. Theory

In order to understand the reaction at electrodes, it is necessary to see the basic electrode kinetics of the simple reaction. It is very important to realise that the elementary analysis given below is for neutral species in aqueous solution but can be applied qualitatively to ionic species [27][28] in solid.

Consider the simple reaction

$$O + ne = R$$

in which the species O is reduced to R by the transfer of n electrons from the inert electrode. This process can be made to occur by passing a current between the electrodes in a cell, such as

Pt | O and R in excess inert electrolyte | Pt
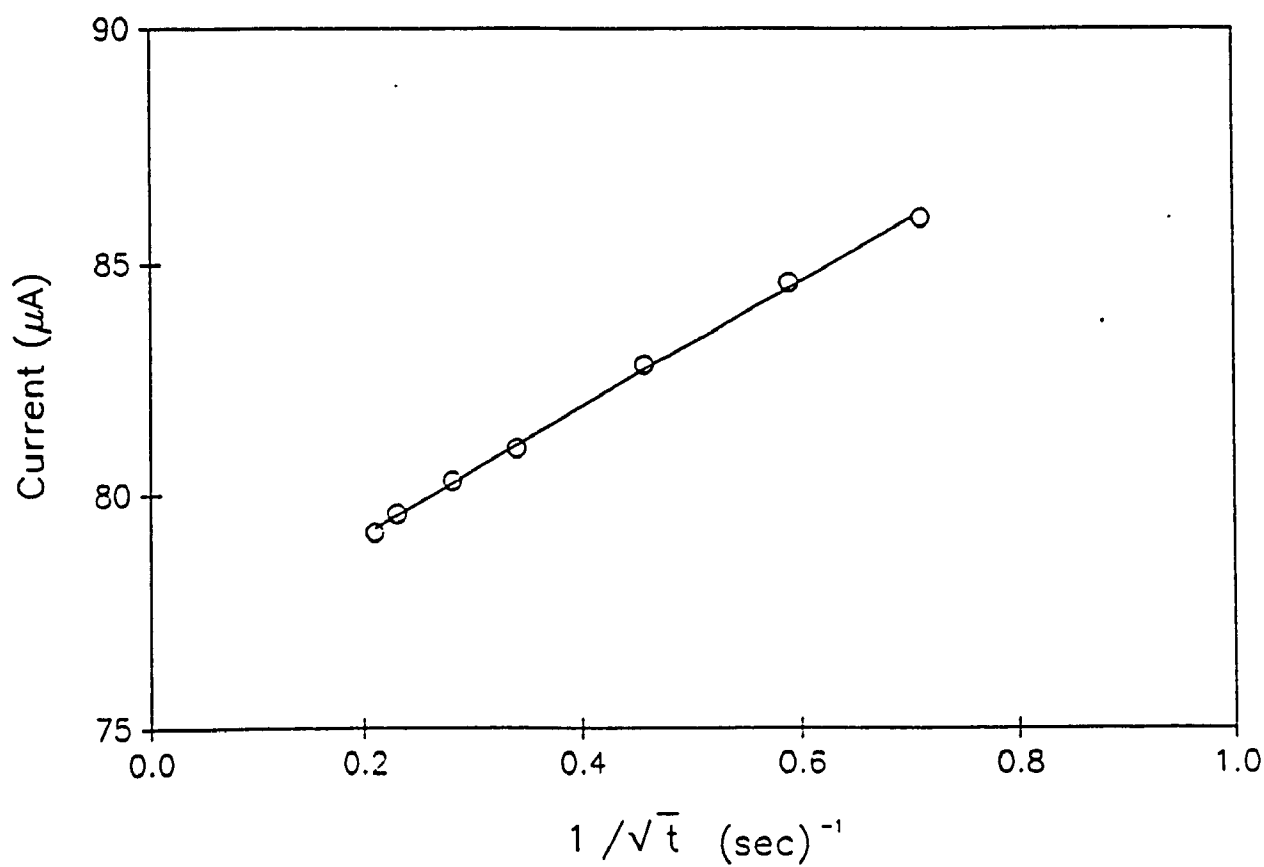
Fig. 4−6 Typical I v.s. $1/\sqrt{t}$ Curve

It is customary to call the electrode at which the reaction of interest occurs the working electrode (W.E.) and the other electrode the counter electrode (C.E.).

At the working electrode, the rate of consumption of O (in mole / sec) is given by Faraday's law

$$-\frac{dN_0}{dt} = \frac{I}{nF} \quad \ldots \ldots 4.1$$

where I (Amp) is the current flowing and F (Coulomb /equiv.) is the Faraday constant. Consequently the magnitude of the current gives a direct measure of the rate of the electrode reaction.

The voltage needed to cause a current I to flow through the cell may be considered as made up of three parts:

1) that to pass the current through the electrolyte;

2) that to drive the reaction at the working electrode

and 3) that to drive the reaction at the counter electrode.

To obtain the relation between the current and the voltage required to drive the reaction at the working electrode, a third electrode (the reference electrode, R.E.) which has a stable and reproducible potential is required. The change in potential of the working electrode needed to cause the current to pass the W.E. interface, can be found by measuring the potential between the working and reference electrodes.

The description given below is for a working electrode in a typical three electrode system. In the case of powder solid electrolytes, it is difficult to provide a third electrode. To obtain the relation between the current and voltage required to drive the reaction at the electrodes, a two electrode system was used in this work. The basic theory however is valid for a two electrode system.

Consider a more general form of the reaction

$$O + ne = R$$

According to transition state theory [30], for a reaction occurring in a single step, the rate of the reaction is

$$\frac{dN_0}{dt} = \frac{AlkTa_0}{h\gamma\pm} \exp\frac{-dG^\bullet}{RT} \quad\ldots\ldots 4.2$$

where A (cm^2) is the electrode area, l (cm) the thickness of the layer containing the ions about to be discharged, a_0 (mole/cm^3) the activity of O$^{\bullet+}$ in the initial state, $\gamma\pm$ the activity coefficient of the activated complex, R the gas constant and dG$^\bullet$ (J/ mole) the standard free energy of activation. Since the current density i = I/A, this equation can be rewritten

$$i = \frac{nFlkTa_0}{h\gamma\pm} \exp\frac{-dG^\bullet}{RT} \quad\ldots\ldots 4.3$$

The Free Energy is the work done in transferring one mole of the substance from an infinitely dilute state at zero potential to the position it occupied in the given phase. This work may be considered as composed of two parts; a chemical part, the chemical potential (u) and an electrical part equal to zFE. i.e.

$$G^0 = u_0 + zFE \quad\quad\quad 4.4$$

Suppose at a potential E_1, the standard free energy is

$$G_1 = u_0 + zFE_1 + nu_e - nFE_1 \quad\quad 4.5$$

where u_0 and u_e are the standard chemical potentials of O$^{\bullet+}$ and the electron respectively. If the potential of the electrode is altered to E_m, the potentials of the ions remaining unaltered, the free energy becomes

$$G_2 = u_0 + zFE_1 + nu_e - nFE_m \quad\quad 4.6$$

So the free energy change is given by (assuming uncharged species)

$$G_2 - G_1 = -nF (E_m - E_1)$$

or $\quad\quad\quad \Delta G^\bullet = -nF\Delta E \quad\quad\quad 4.7$

where ΔE is the potential difference between the electrode and the ion about to be reduced. Substituting $\Delta G^\bullet$ into equation (4.3) and introducing the term of α, transfer coefficient, $0 < (1-\alpha) < 1$, the current density is

$$i = nFk'a_0 \exp-\frac{\alpha nF\Delta E}{RT}$$

when the activity coefficients in a constant, for the reduction reaction,

$$\overleftarrow{I} = nFk_1c_o^0 \exp{-\alpha nf\Delta E} \qquad (4.8)$$

$$and \qquad \overleftarrow{I} = nFk_{-1}c_R^0 \exp(1-\alpha)nf\Delta E \qquad (where f = \frac{F}{RT}) \qquad (4.9)$$

The net rate of the reduction reaction is given by

$$i = \overrightarrow{I} - \overleftarrow{I}$$

At the reversible potential of the system, $i = 0$, so that,

$$\overrightarrow{I} = \overleftarrow{I} = i_0$$

where i_0 is exchange current density,

$$i_0 = nFk_1c_0^b \exp{-\alpha nfE_r}$$

$$= nFk_{-1}c_R^b \exp(1-\alpha)nfE_r \qquad (4.10)$$

where E_r is rest potential, c^b is bulk concentration. So the equation 4.8, 4.9 can be rewritten as

$$\overleftarrow{I} = i_0 \exp{-\alpha nf\eta}$$

$$and \qquad \overrightarrow{I} = i_0 \exp(1-\alpha)nf\eta \qquad (4.11)$$

where, η is called overpotential, $\eta = E - E_r$.

When $n\eta < -60$ mV,

$$i \approx \overrightarrow{I} = i_0 \exp{\frac{-\alpha nF\eta}{RT}} \qquad (4.12)$$

Taking logarithms of eq. (4.12) and rearranging gives Tafel equations

$$\eta = -\frac{RT}{(1-\alpha)n_a F}\ln i_0 + \frac{RT}{(1-\alpha)n_a F}\ln|i|$$

47

$$\text{or} \qquad \eta = a + b \log i \qquad (4.13)$$

Electrochemical systems can therefore be described in terms of the exchange current density i_0 and the Tafel slope b.

4.3.2. Experimental

To investigate the electrode behaviour, two non-blocking Sn electrodes, were used. The I-V curve was measured using a Princeton Applied Research polarographic analyzer, Model 364, with a constant potential rate 5 mV/sec. The current was monitored by using a Y-t recorder (Fisher recordall, Series 5000). The electrolyte resistance R was measured in order to correct the applied Va,

$$V = V_a - IR$$

where

V = the sum of the voltages across both interfaces;

Va = the applied voltage across the whole cell;

I = the current passing;

R = the electrolyte resistance.

The obtained plot of log I-V was linear. The transfer coefficient (α) may be obtained from the slope of this graph, and the exchange current density i_0 from the value of the Tafel equation at V=0. However, in this two electrode system it is impossible to identify the process (either cathodic or anodic) with which these values are associated although certain qualitative conclusions can be proposed (see Section 6.4).

4.4. Thermodynamics Properties of Solid Electrolytes

4.4.1. Definitions

All matter has energy arising from the motion and the configuration of its internal particles. Such

48

energy is called the internal energy, U [29]. The heat, Q, is energy transferred, without transfer of mass, across the boundary of the system because of a temperature difference between the system and surroundings. The work, W, is the energy transferred, without transfer of mass, across the boundary of a system because of an intensive property difference other than temperature that exists between the system and surroundings.

The enthalpy H of a system is defined as

$$H = U + PV$$

where P is pressure and V is volume of the system. The enthalpy change of the system is

$$\Delta H = \Delta U + \Delta PV$$

The entropy of a pure substance is the property of matter held constant in a reversible adiabatic process and it increases in all real processes. In other words, the entropy change is zero for a reversible process ($\Delta S = 0$) and greater than zero for an irreversible process ($\Delta S > 0$) according to the second law of thermodynamics. The third law of thermodynamics enables the absolute entropies of substances to be determined. "The entropy of a pure substance in complete thermodynamic equilibrium becomes zero at the absolute zero temperature"; this is the third law of thermodynamics. The entropy (pure substance in equilibrium) can also be defined as

$$S = \int_0^T \frac{d\,Q_{rev}}{T}$$

where: ΔQ is the heat capacity change, T is absolute temperature.

4.4.2. The Gibb's Free Energy, ΔG

From the relation

$$\Delta Q = \Delta U + \Delta W$$

The work done by the system is the force PA times the distance dx under a constant pressure, P is the pressure applied and A is the area of the system. Since the Adx is the change in volume ΔV,

$$\Delta Q = \Delta U + P\,\Delta V$$

$$= \Delta U + \Delta PV$$

Thus at a constant pressure,

$$\Delta Q = \Delta H$$

According to the Second Law for a spontaneous process,

$$\Delta S_{syst} + \Delta S_{surr} > 0$$

Even though a process itself is proceeding irreversibly, heat may however be transferred to the surroundings in a reversible fashion.

$$dS_{surr} = \frac{\Delta Q \text{ (to surr)}}{T}$$

$$= \frac{-\Delta Q \text{ (from surr to syst)}}{T}$$

under isobaric conditions $\Delta Q = \Delta H$

$$\Delta S_{surr} = -\Delta H / T \text{ (to syst)}$$

$$\Delta S_{syst} > \Delta H / T \text{ (to syst)}$$

or $\qquad \Delta H - T \Delta S_{syst} < 0$

So, for a spontaneous reaction, the enthalpy change of the system is less than zero. Similarly for a reaction at equilibrium,

$$\Delta H - T \Delta S_{syst} = 0$$

And for a process that cannot proceed

$$\Delta H - T \Delta S_{syst} > 0$$

Consequently the quantity (ΔH - T ΔS) can be used as an index as to whether or not a process is spontaneous. The relation (ΔH - TΔS) is known as the Gibb's free energy ΔG. That is

$$\Delta G = \Delta H - T \Delta S$$

For a reaction with charge transfer, eg.

$$Sn^{2+} + 2F^- \longrightarrow Sn + F_2$$

$$Sn^{2+} + 2e \longrightarrow Sn \qquad E_1 \text{ cathodic}$$

$$2F^- - 2e \longrightarrow F_2 \qquad E_2 \text{ anodic}$$
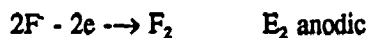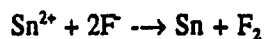
The Gibb's free energy for each process can be also expressed as

50

$$\Delta G = -nFE_d = -nF (E_1 - E_2)$$

where F is the Faraday constant and E_d is the decomposition potential.

4.4.3. The Electrochemical Determination of ΔH, ΔS and ΔG

When an increasing potential pass through blocking electrodes, the electrolyte will be decomposed at a certain potential and a large charge in current will occur. The measurement of decomposition potential of electrolytes was performed using a Princeton Applied Research Polarographic Analyzer, Model 364, with 5 mV/sec potential rate as a function of temperature. The ΔS was calculated from the slope of E_d vs. T.

$$\Delta G = -nFE_d = \Delta H - T \Delta S$$

$$\Delta S = nFdE_d /dT$$

The values of ΔG and ΔH at 25 °C were calculated using

$$\Delta G = -nFE_d$$

and $\qquad \Delta G = \Delta H - T\Delta S$

therefore $\qquad$ Slope $= \Delta S/nF$

(n is assumed to be equal to 2)

CHAPTER 5.

RESULTS AND DISCUSSION (1)

Chemical Analyses and Physical Characterization

of the Compounds Formed in the CaF_2-SnF_2 System

The chemical analyses and physical properties of the compounds obtained in the CaF_2-SnF_2 system are discussed in this chapter. Elemental analyses provide the overall chemical composition of the products. X-ray powder diffraction results give information on the crystallinity of the materials and allow for identification of some of the phases. The oxidation state of Sn and an insight into its environment is obtained from Mössbauer Spectroscopy. Bulk density measurements give the packing efficiency of the ions in the solids and provide some educated guess on the stability of the phases obtained. Based on these results, a tentative interpretation of the nature of the phases in this system will be given.

5.1. Yield

The product of the reaction of SnF_2 and $Ca(NO_3)_2$ in aqueous solutions is a white powder at all values of n, where n is the reaction mole fraction, i.e, n = moles of $Ca(NO_3)_2$ / [moles of $Ca(NO_3)_2$ + moles of SnF_2]. Since the calcium nitrate solution was added to the SnF_2 solution, and not vice-versa, and since under these conditions, the product obtained with Pb and Sr nitrates was always free of nitrate ions (i.e. the only anion in the solid was the fluoride ion)[13, 15], it is assumed at this point that our product is a mixed fluoride of tin and calcium that is nitrate free. Assuming the above (which is justified by the elemental analyses presented in section 5.2 below) and considering that SnF_2 is the only source of fluoride ions in the reaction of SnF_2 and calcium nitrate in aqueous solutions, the yield of product was calculated relative of the mass of SnF_2 used in the reaction, therefore:

$$\text{Yield (\%)} = \frac{\text{mass of solid collected}}{\text{mass of } SnF_2 \text{ used}} \times 100$$
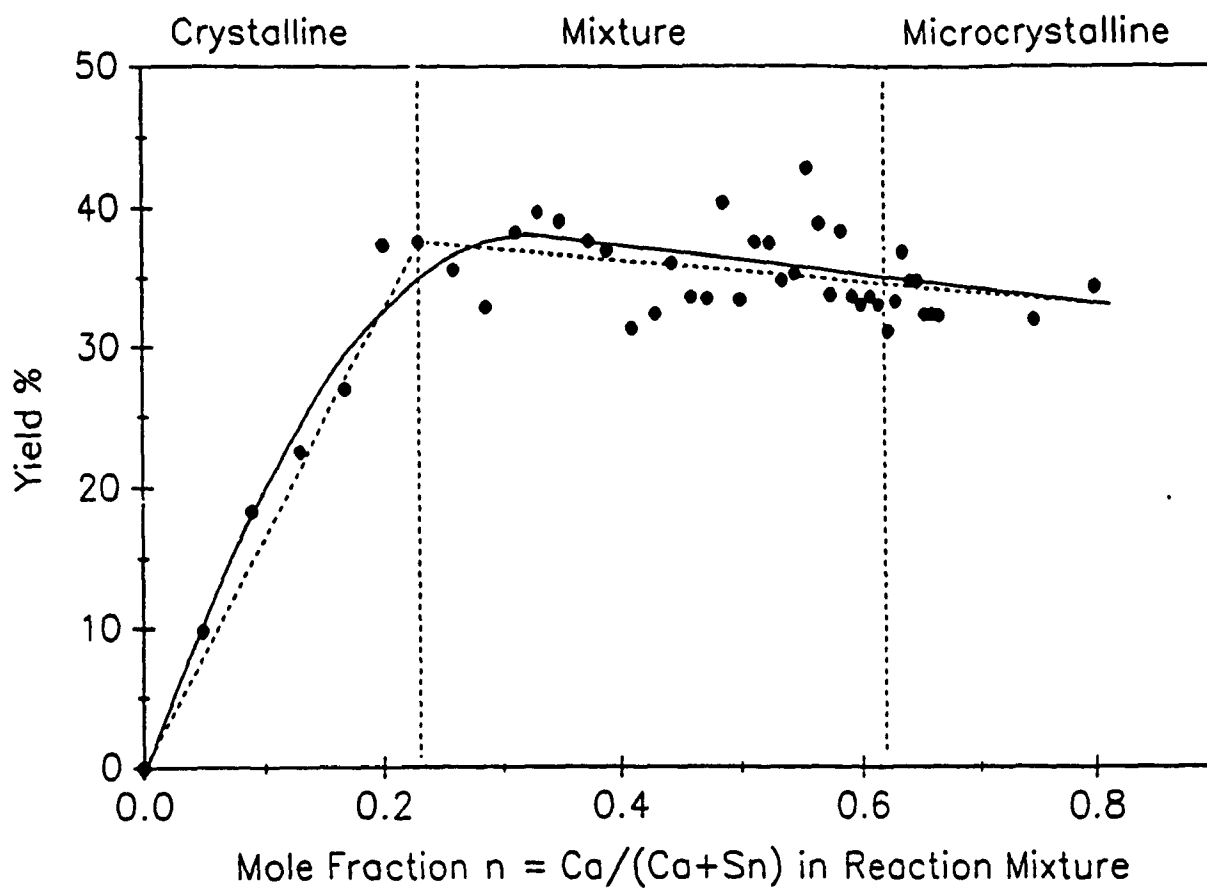
Fig. 5-1 Yield % of the Product of the Reaction of
SnF$_2$ and Ca(NO$_3$)$_2$·4H$_2$O in Aqueous Solution

53

The results are given in Appendix II and Fig. 5-1. The yield increases sharply with the percent molar ratio of calcium nitrate and seems to level off at around a molar fraction of 0.2. for higher molar fractions, the results are much more scattered. However, a general trend of a slow decrease of yield is apparent. It is obvious that the yield increases as the Ca content increases until the exact stoichiometry of the reaction is reached. Beyond, the yield should decrease. However, this simplistic behaviour would be observed only if one solid phase, of constant composition, was produced for all values of the molar fraction in the reaction mixture. The chemical analyses and X-ray diffraction results given below show that two phases are produced, often in variable amounts, therefore the yield versus molar fraction is a more complicated function. The yield will be discussed further after interpretation of the X-ray diffraction data.

5.2. Elemental Analysis

The elemental analysis results for Ca^{2+}, Sn^{2+}, F^-, and NO_3^- are shown in Fig. 5-2 and Fig. 5-3. The experimental data are listed in Appendix III. As can be seen in Fig. 5-2, the content of Ca^{2+} increases as n increases, while the Sn^{2+} content decreases. Therefore, the metal composition of the product varies with the composition of the reaction mixture in such a way that reaction mixtures rich in tin give products rich in tin and poor in calcium, and vice-versa. Figure 5-3 shows that the F^- content is not significantly dependent on n and that only a minor amount of NO_3^- is present in the sample, and it does not change significantly with n. This justifies our earlier assumption that the product is a fluoride, and not a fluoronitrate, and it is slightly contaminated by NO_3^- ions.

Figures 5-2 and 5-3 show that the amount of fluoride and the sum of the amounts of calcium and tin are slightly below the theoretical values of 66.7% for F, and 33.3% for (Ca + Sn), however, if one does not take the nitrate impurity into account in the calculation (since it does not belong to the fluoride phase), the experimental values are in excellent agreement with the hypothesis of a nitrate-free mixed fluoride of tin(II) and calcium: the average of the eleven points is 67.1% F and 33.2% (Ca + Sn) which gives a fluorine/metal ratio of 2.02 (theoretical value = 2). Since the nitrate ion is present only as a minor impurity, the material obtained can be formulated as a mixed fluoride of tin and calcium, $Ca_{1-x}Sn_xF_2$, or a mixture of such mixed

54
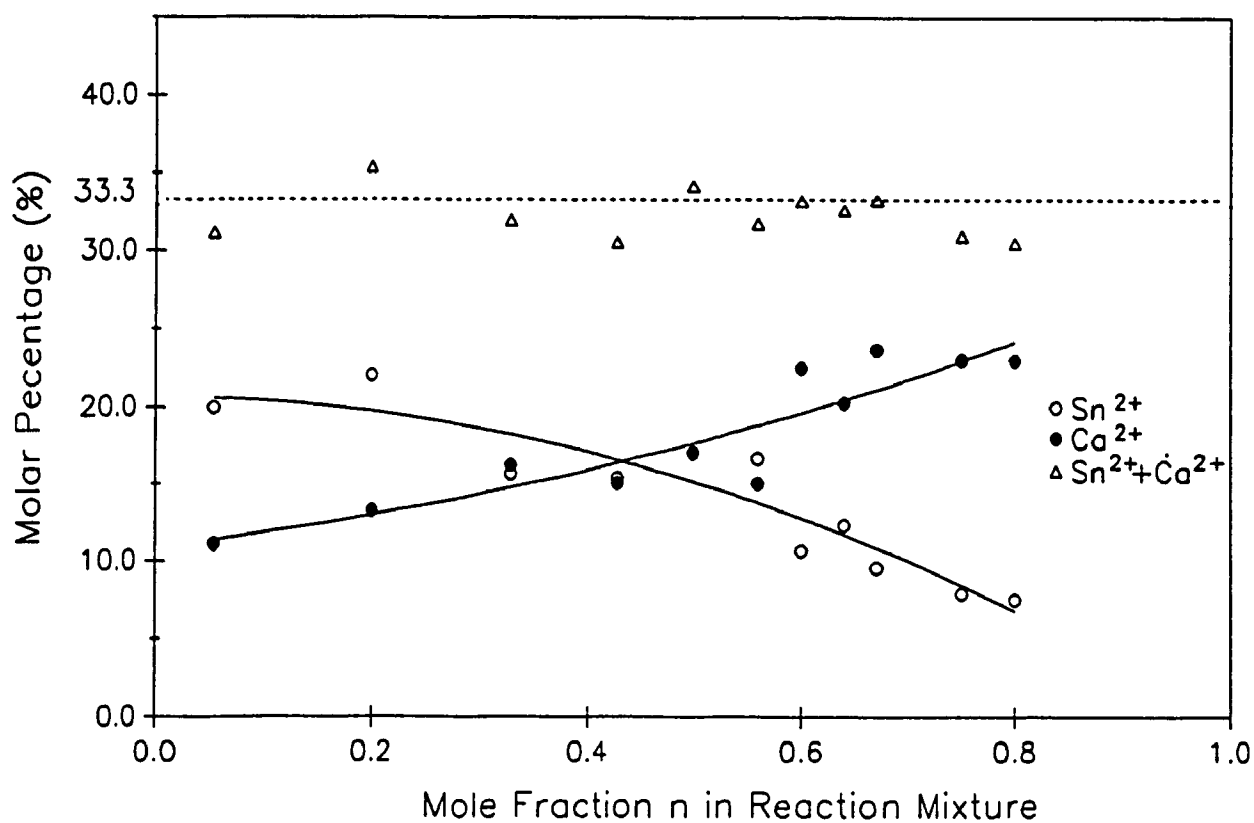
Fig. 5−2. Elemental Analysis of the Metals in the CaF2−SnF2 System
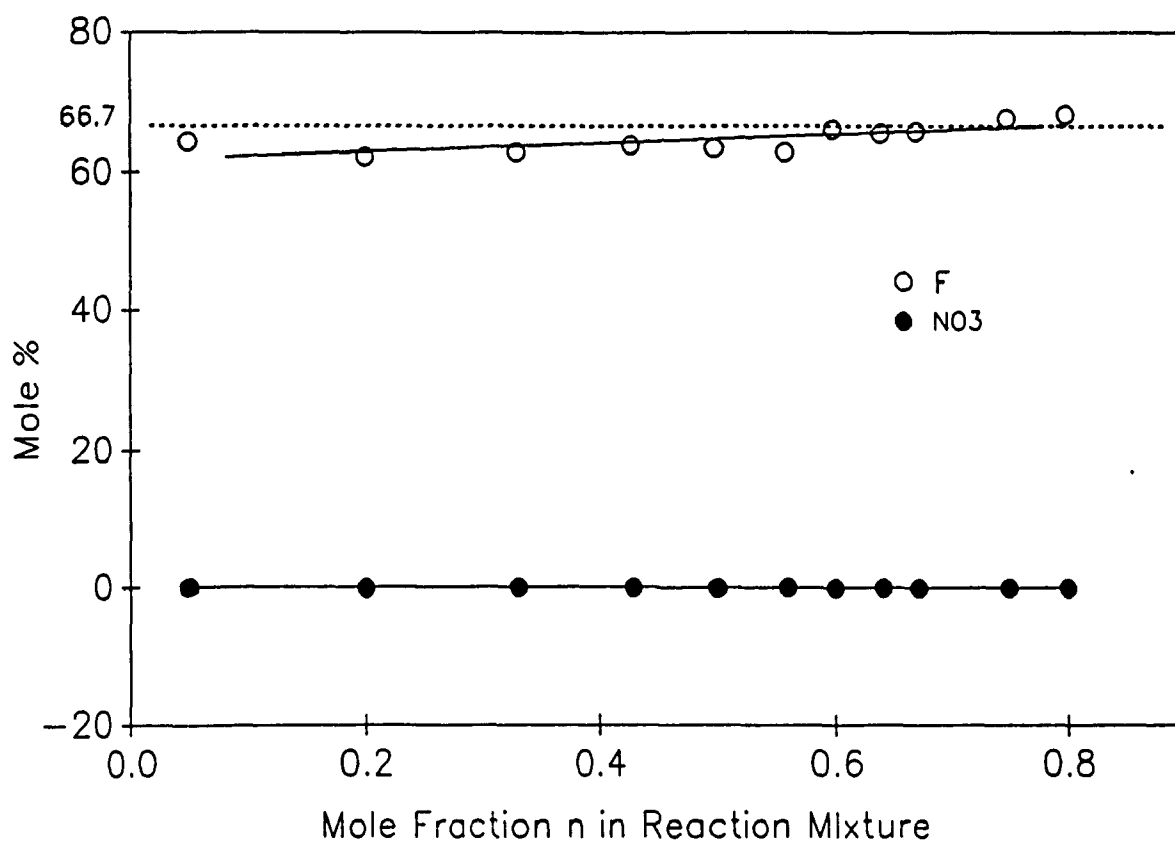
Fig. 5–3. Elemental Analysis of F^- and NO_3^- in the CaF2–SnF2 System

fluorides, each with a different substitution ratio, x. This explains why this assumption was made when calculating the yield. Figure 5-4 shows the tin substitution ratio versus the molar ratio of the reaction mixture. This figure will be discussed in greater details in the interpretation of the X-ray diffraction results. However, at this point, it is noteworthy to mention the following:

(i) For reaction mixtures poor in calcium (n<0.23), the product contains less tin and therefore more calcium than the reaction mixture. From n=0 to 0.23, the tin content is quasi-constant and, within experimental error, the formula of the product is $CaSn_2F_6$ (ie. Sn/Ca =2);

(ii) For medium values of the composition of the reaction mixture (ca. n=0.23 to 0.55) the metal content is constant (Sn/Ca =1) and implies the product has the formula $CaSnF_4$;

(iii) For n≥0.60, the tin content decreases linearly with the increasing stoichiometry of Ca in the reaction mixture;

(iv) For n<0.5, the product is poor in tin and richer in calcium than the reaction mixture, whereas for n≥0.5, the metal composition of the product is close to that of the reaction mixture.

It should be pointed out that the formulation of compositions of $CaSn_2F_6$, $CaSnF_4$ and Ca_2SnF_6 does not necessarily mean that such phases exist. One must first analyze the X-ray diffraction results in order to identify the crystalline phases that are present.

5.3. X-ray Powder Diffraction

X-ray powder diffraction was performed in order to identify the crystalline phases in the product and carry out their structural study. The results of the influence of the stoichiometry of the reaction and the influence of stirring rate, together with the stability of the phases obtained are described in the following sections.

5.3.1. Influence of the Stoichiometry of the Reaction

5.3.1.1 Reaction Mixtures Rich in Tin
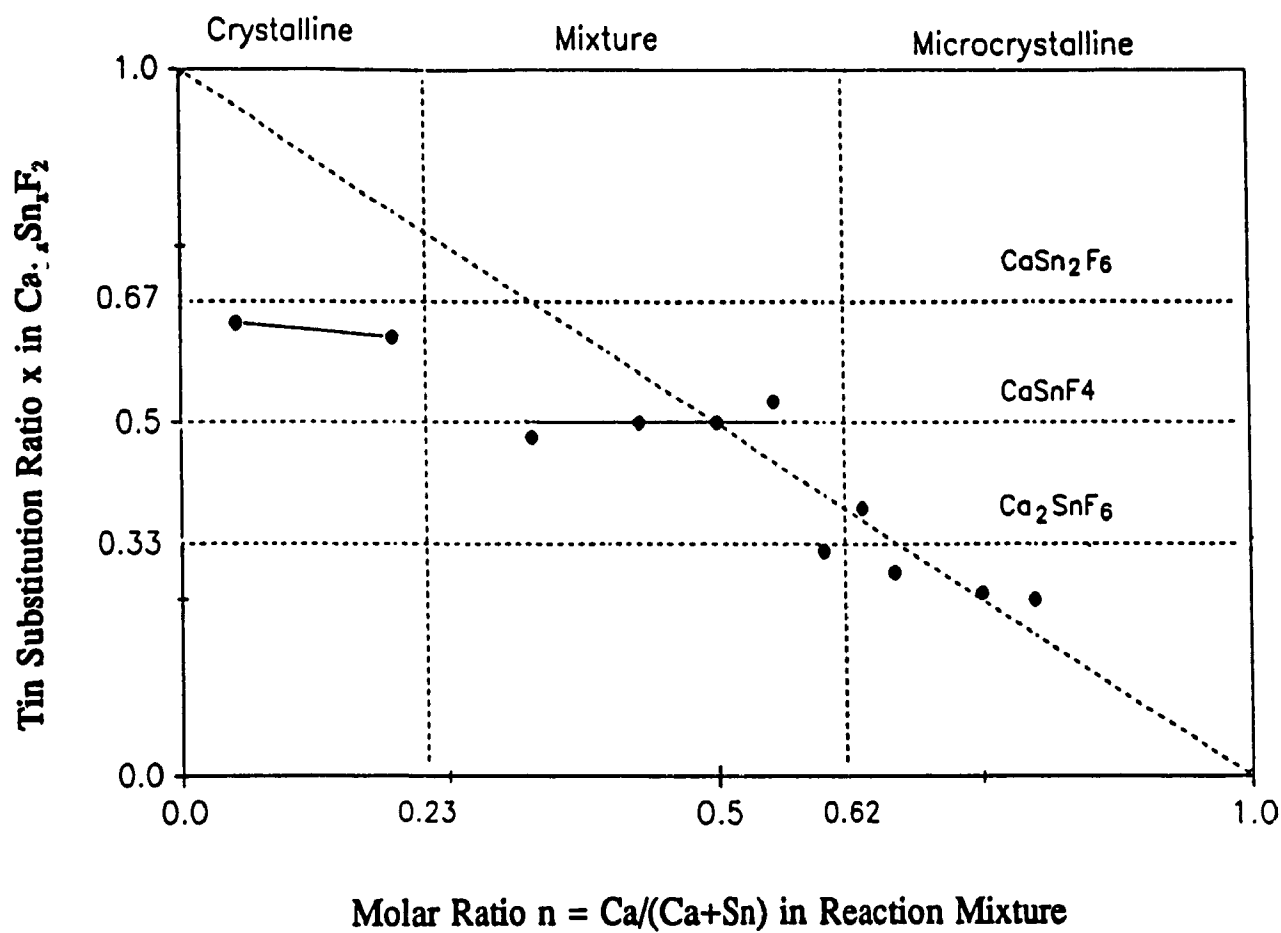
Fig. 5-4 Tin Substitution Ratio in $Ca_{1-x}Sn_xF_2$ Versus the Composition of the Reaction Mixture

The product obtained using a reaction mixture very rich in tin (n<0.2) gives a large number of sharp Bragg peaks (Fig. 5-5(a) and Appendix (IV) which indicates that the sample is crystalline. These peaks do not match those of α-SnF$_2$ [31] or CaF$_2$[32], therefore a new product has been obtained. A search match of the JCPDS powder file using the Micro Powder Diffraction Search Method (μPDSM) from Fein Marquat Associates Inc. did not yield any satisfactory match, therefore, the new product we obtained has not been reported yet. Table 5-1 shows that Sn$_7$F$_{16}$ was the best match found with the JCPDS data base, however, this is not a good match:

(i) the similarity index SI=82: this is not very high; a good match gives a SI =150 to 200 or higher. All other compounds in Table 5-1 give matches that are even poorer, and for some, are chemically impossible;

(ii) ML/X = 9/4: only 9 lines of Sn$_7$F$_{16}$ are matched by the lines of the samples, and 4 lines are unmatched. This would be acceptable only if the four unmatched lines were weak. However, Table 5-2 shows that the 4 missing lines have the intensities 16, 11, 8.9 and 8.9, respectively , relative to the most intense line having the intensity 44. Therefore, if the intensity of the most intense line of Sn$_7$F$_{16}$ is normalized to 100, the missing lines have an intensity of 36, 25, 20 and 20, respectively. These intensities are too high to be ignored. Subtracting the pattern of Sn$_7$F$_{16}$ from the experimental pattern leaves 15 lines unaccounted for and 67.5% of the original total intensity of the Bragg peaks remains (Table 5-3). The unsatisfactory match makes it highly unlikely that Sn$_7$F$_{16}$ is present in the sample. In addition, chemical analysis shows that the sample contains 12-13% (mol.) Ca, which would not be accounted for by Sn$_7$F$_{16}$.

Attempts were made to index the powder pattern of Fig. 5-5 in the tetragonal system (the number of peaks being too high for a cubic system). With the help of a calculator, several solutions were tried, in a trial-and-error method for relatively simple indexation for the first two peaks. However, this did not lead to any successful solution. Therefore, it must be concluded that the symmetry is most likely lower than tetragonal. Since no single crystal could be obtained, an automatic indexing program on a computer would be required for a successful indexation of the powder pattern. Such a program was not available to us. Therefore, we were not able to obtain the indexation of the Bragg peaks, the unit-cell parameters and crystal

Table 5-1. Search Match for the Crystalline Phase

```
┌JCPDS#───SI───ML/X──At%──Identity . . . . ──────────────
│F1
├─────────────────────────────────────────
│F2
│──Search Results [17 Entries]─
 28-1389    82   9/4   44   Tin Fluoride = Sn7F16
 15-0744*   55   9/6   79   *Tin Fluoride = SnF2
 29-0388C   26   2/1   38   Calcium Tin = CaSn3
 25-1259    20   4/5   45   *Tin Oxide = Sn2O3
 10-0348    19   2/2   46   Calcium = Ca
 7-0195     19   3/4   20   Tin Oxide = SnO
 18-1386D   15   4/7   71   Tin Oxide = Sn5O6
 16-0737    13   4/7   29   *Tin Oxide = Sn3O4
 30-1374O   12   3/2   24   Tin Oxide Fluoride = Sn4O2F4
 36-1868O   10   2/4   55   C.I. Pigment Yellow 151 =
 30-1375C   10   9/7   46   Tin Oxide Fluoride = (Sn2O2F4)Sn2
 16-0687I    9   3/3   27   Ice / Ice, syn = H2O
 36-0766     7   3/3   30   Ice = H2O
 36-1792O    4   2/7   34   C.I. Pigment Red 223 =
 13-0745     2   4/5   80   Yeast Uridylic Acid =

       Ierr:50,150    derr:4.0   Bground:7    dmax/min:14.68/1.541
  ─Test Results [ 0 Entries]─
└Plot Shift+F8──Hold F1 F2──Copy Ins──Test F7──Match F8──Subtract F9──Exit Esc┘
```

Table 5-2 Matching Table of Sn$_7$F$_{16}$ with the Crystalline Phase

JCPDS#	SI	ML/X	At%	Identity . . .
28-1389	82	9/4	44	Tin Fluoride = Sn7F16

Ierr:50,150   derr:4.0   Bground:7   dmax/min:14.68/1.541   * Obscured Lines

28-1389 @ 44.4%

d	I	User Pattern d	I	derr	Resid I
4.46	6.2	Below Background			
3.62	40	3.618	85	-0.2	None
+ 3.60	44			+1.4	
		3.529	100	-5.5	
3.41	36	3.410	38	0.0	None
3.24	40	3.279	52	+3.7	None
		3.075	59	+8.3	
3.00	4.4	Below Background			
2.877	1.3	Below Background			
2.546	16	Missing			
		2.3730	10	+7.3	
2.333	1.8	Below Background			
2.313	1.8	Below Background			
2.232	2.7	Below Background			
		2.2040	12	+4.4	
2.183	11	Missing			
2.129	2.2*	2.1300	12	+0.2	10
2.090	8.0	2.1060	7	+3.7	None

28-1389 @ 44.4%

d	I	User Pattern d	I	derr	Resid I
2.046	8.9	2.0630	14	+4.1	
2.033	13	Missing			
1.990	16	2.0280	10	-1.2	None
1.936	2.7	1.9900	8	0.0	None
1.908	3.6*	Below Background			
1.886	2.2	1.9090	28	+0.3	24
1.864	8.9	Below Background			
1.836	2.7	Missing			
1.822	1.3*	Below Background			
1.789	5.3	1.8140	17	-2.4	16
1.774	8.9	Below Background			
1.752	11	1.7720	14	-0.6	None
1.702	1.8*	1.7580	14	+2.0	None
1.654	1.3	1.7080	11	+2.1	9
1.636	1.3	Below Background			
1.605	6.2	Below Background			

Plot Shift+F8   Return to Tables Esc

Table 5-3 Result of the Substraction of the Powder Pattern of Sn_7F_{16} from the Observed Pattern

```
JCPDS#____SI____ML/X____At%____Identity . . .
28-1389   82    9/4    44   Tin Fluoride = Sn7F16
     Ierr:50,150    derr:4.0  Bground:7    dmax/min:14.68/1.541
Subtraction

Lines removed: 3.618  3.410  3.279  2.1060 2.0280 1.9900 1.7720
               1.7580

Lines reduced (d=Inew): 2.1300=10    1.9090=24    1.8140=16
               1.7080=9

  8 lines removed.    4 lines reduced.    15 lines left.
67.5% of the original total intensity remains.
Use MODIFY to make manual adjustments.



                      Press Esc when ready to proceed
```

system for the crystalline material, $CaSn_2F_6$. The narrow linewidth of the bragg peak shows that the diameter of the particles is larger than ca. 1000 Å.

5.3.1.2. Reaction Mixtures rich in Calcium.

For reaction mixtures with a molar ratio $Ca/(Ca+Sn) > 0.62$, the X-ray powder pattern of the product changes dramatically. Figure 5-5(b) and Appendix V-A show that there are very few peaks, only four in the angular range 12-60 (2θ)° explored. These peaks are easily indexed in a cubic F lattice, with the Miller indices (111), (200), (220) and (311), respectively. This gives a unit-cell parameter a, which varies from ca. 5.44 to 5.67 Å, depending on the composition of the reaction mixture. This powder pattern has the same peak sequence (in d-spacing, indexation and intensity) as that of CaF_2 (Appendix V-B) with a similar unit-cell parameter (CaF_2 : a=5.4626 Å)[33]. Our measured value for the unit-cell parameter of crystalline commercial CaF_2 (a=5.4592 Å) is in good agreement with literature. Comparison of Fig. 5-5(a) and 5-5(b) shows that the peaks of the latter are much broader, which indicates that the CaF_2-type phase obtained when the reaction mixture is rich in calcium is microcrystalline. The average particle diameter of a microcrystalline phase can be calculated using Scherrer's formula [34]:

$$t = \frac{0.9\lambda}{B\cos\theta} \quad \ldots \ldots (5.1)$$

Where t= Average particle diameter (in Å)

λ= Wavelength of the radiation (1.54178 Å for $K_\alpha Cu$)

B= Broadening due to small partial size

θ= Bragg angle.

The contribution of microcrystallinity to linebroadening is obtained from the experimental linewidth after correction by Warren's method [34]:

$$B^2 = B_m^2 - B_s^2 \quad \ldots \ldots (5.2)$$
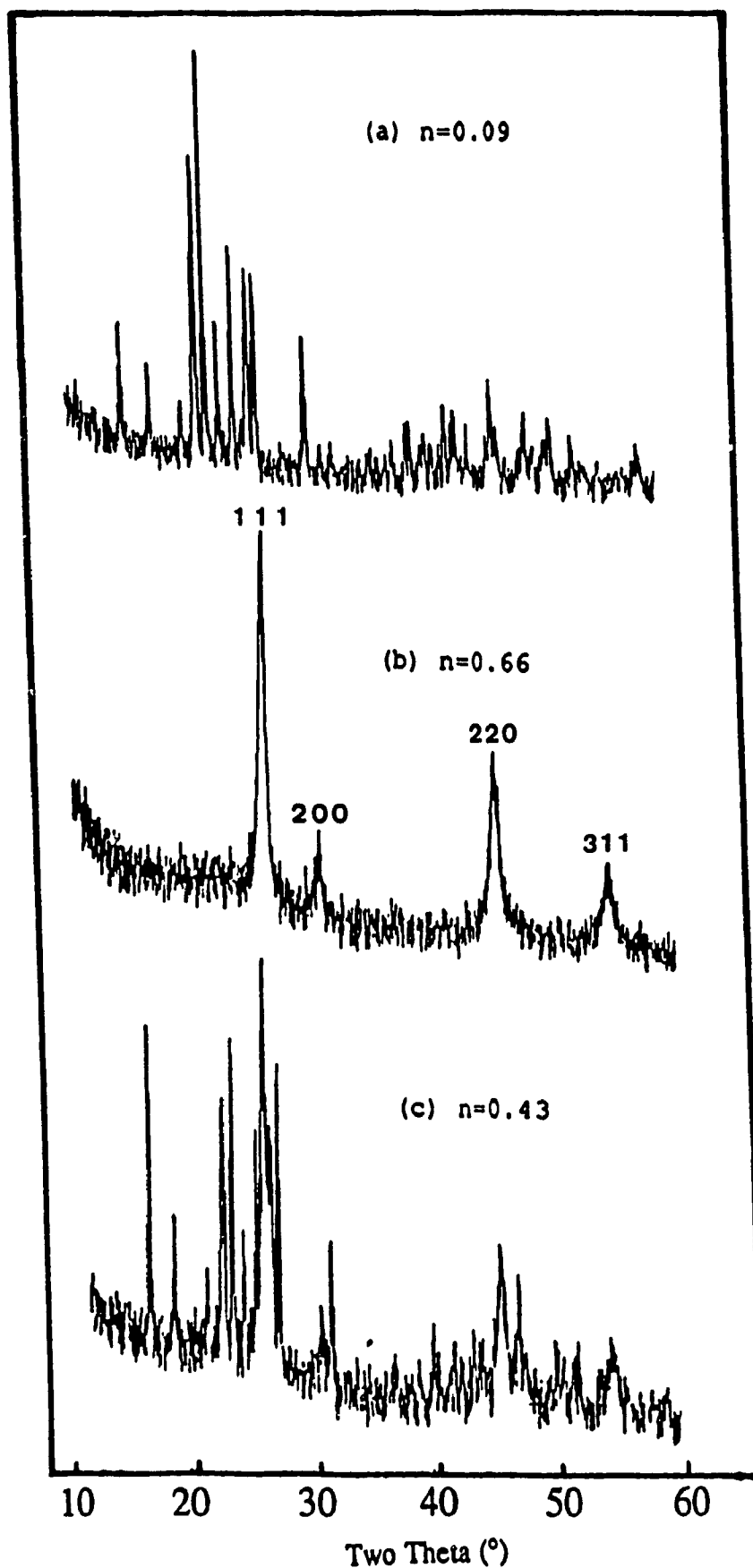
Fig. 5-5 Influence of the Stoichiometry of the Reaction Mixture
on the X-ray Powder Diffraction Pattern of the Product

where B_M and B_s are the linewidth at half height for the sample and for a well-crystalline standard, respectively, in radians. α-SnF$_2$ was used as a standard for crystallinity. The average particle size of most microcrystalline CaF$_2$-type phases was found to be 350-400 Å, which confirms the presence of a significant degree of microcrystallinity. When the average particle diameter of a solid material is smaller than ca. 1000 Å, broadening of the Bragg peaks occurs. As the particle size decreases, the linewidth increases, up to ca. 30-40 Å, at which point the Bragg peaks become so broad that they become undistinguishable from the background and no powder pattern is obtained.

5.3.1.3. Reaction Mixtures Containing Similar Amounts of Calcium and Tin

When the molar ratio n=Ca/(Ca+Sn) is larger than 0.2 and lower than 0.6, a mixture of the crystalline phase, CaSn$_2$F$_6$, and of the microcrystalline solid solution Ca$_{1-x}$Sn$_x$F$_2$ (CaF$_2$-type) is obtained. A typical X-ray powder pattern is given in Fig.5-5(c) (molar ratio n=0.43 in the reaction mixture). The experimental diffraction pattern contains both the narrow peaks of crystalline CaSn$_2$F$_6$ and the broad peaks of the microcrystalline Ca$_{1-}$Sn$_x$F$_2$ solid solutio.

The limits of each zone (crystalline, mixture or microcrystalline) is given on Fig. 5-1 and 5-4.

5.3.2. Influence of Stirring Rate

In all sample preparations described above, a medium speed setting of the magnetic stirrer was used while the solution of calcium nitrate was being added to the solution of SnF$_2$. However, it was found that, despite our efforts to use identical reaction parameters, the results obtained were not perfectly reproducible in the range $0.20 \leq n \leq 0.60$, where n is the molar ratio Ca/(Ca+Sn) in the reaction mixture. One of the reaction parameters difficult to control is the speed of the magnetic stirrer. In order to check for its influence on the nature of the product, the stoichiometric ratio n=0.46 (i.e. about in the middle of the range that gives a mixture of crystalline and microcrystalline phases) was used at three clearly different stirring speeds, si.e. low, medium, and fast. The results shown in Fig. 5-6 and Appendices VI to VIII are striking:

(i) At a fast stirring rate, only the crystalline phase is obtained;

(ii) At a medium stirring rate, the product contains a major part of crystalline phase and a minor part of microcrystalline phase.

(iii) At a slow stirring rate, the major constituent is the microcrystalline phase (average particle diameter: 391 Å) whereas the crystalline phase is a minor component.

This experiment shows the extreme sensitivity of the nature of the product to reactions parameters. Small variations in the stirring rate from one synthesis to another can probably account for the scattering of the results obtained in the range where a mixture of the two phases were found, i.e. the yield (Fig. 5-1) and the elemental analysis (Appendix III). This probably reflects local concentrations in the reaction mixture. Thus the influence of the stirring rate shows that the product obtained depends on the metal ions in excess at the nucleation site:

(i) At a slow stirring rate, Ca^{2+} is locally in excess, and it results in the production of the CaF_2 -type $Ca_{1-x}Sn_xF_2$ as the major product obtained. This is not surprising since, when Ca^{2+} and F^- are present in aqueous solutions, highly insoluble CaF_2 is precipitated. This is a well-known procedure for removing fluoride ions from aqueous solution, which consists in adding a soluble salt of calcium, in order to precipitate the fluoride ions in the form of CaF_2. As a practical application, the insolubility of CaF_2 is used to treat HF burns, by injection of a solution of a calcium salt in tissues burned with HF. In our case, the presence of a limited amount of tin (II) at the precipitation site leads to the incorporation of divalent tin in the CaF_2 structure, to give a $Ca_{1-x}Sn_xF_2$ solid solution.

(ii) At a fast stirring rate, mixing of the two solutions is more efficient and crystalline $CaSn_2F_6$ is obtained.

(iii) For medium stirring rates, a mixture of the two phases is produced.

5.3.3. Unit-cell Parameter of the Microcrystalline Phase

Since the microcrystalline phase crystallizes in the cubic crystal system, the unit-cell parameter "a" can be easily calculated from the d-spacing "d" from any of the (hkl) Bragg peaks, using the equation

66
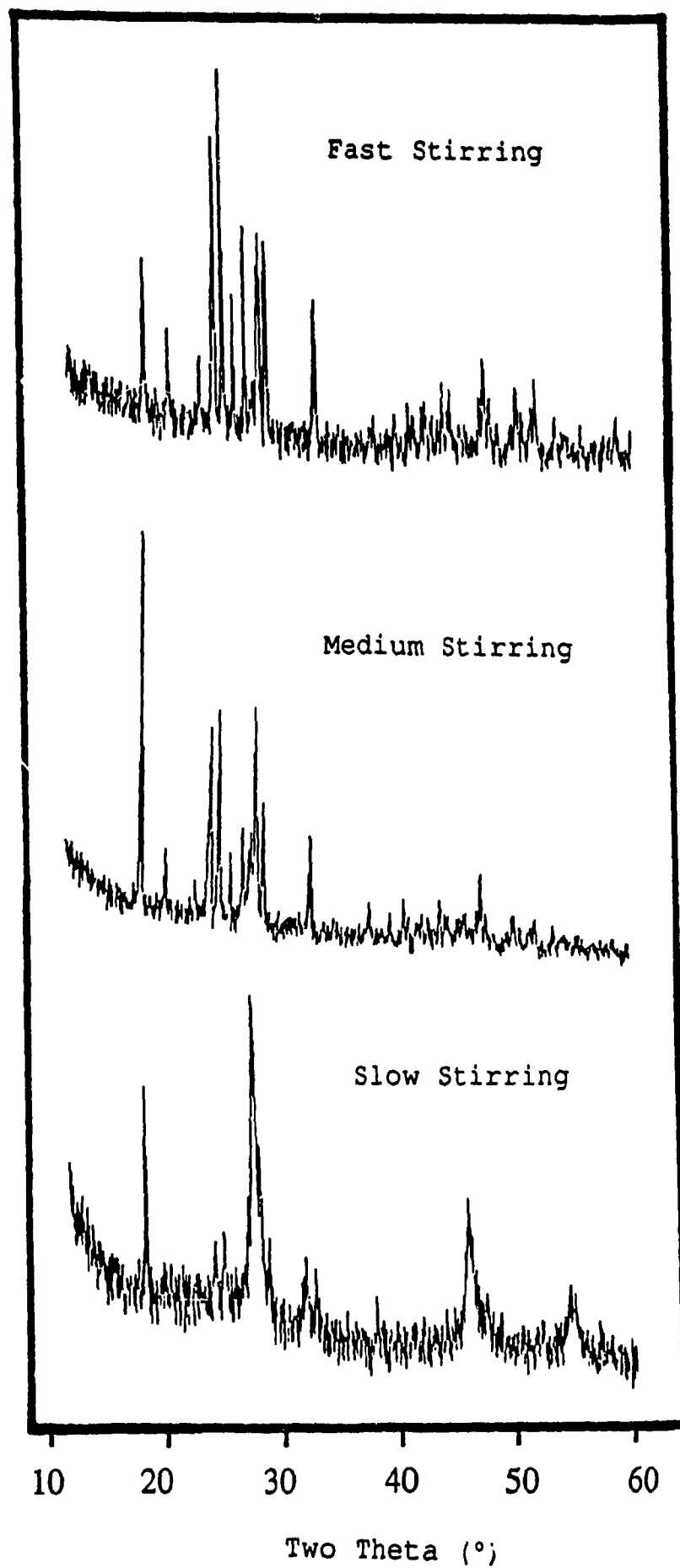
Fig. 5-6. Influence of Stirring Rate on the Nature of the Product for n=0.46

67

$$a = d\sqrt{h^2 + k^2 + l^2} \quad \ldots \ldots (5.3)$$

The unit-cell parameter plotted versus the molar fraction n of calcium in the reaction mixture shows no significant trend (Fig. 5-7 and Appendix IX). To the contrary, the results are highly scattered. One can expect the substitution of a fraction x of Ca^{2+} by x Sn^{2+} to result in an increase of unit-cell parameter since tin (II) is larger than Ca(II); the molar volume of CaF_2 and SnF_2 being the following:

$$V_{(CaF2)} = 40.75 \text{ Å}^3/CaF_2 \text{ unit } [32]$$

$$V_{(SnF2)} = 53.29 \text{ Å}^3/SnF_2 \text{ unit } [35]$$

However, in the range 0.23 to 0.62 molar ratio in the reaction mixture, the composition of the mixture varies widely and, as discussed in the paragraph 5.3.2., it is a function of the stirring rate. Therefore, it is not surprising that the unit-cell parameter, which is a function of the composition of the microcrystalline phase, gives highly scattered values. A plot of the unit-cell parameter versus the substitution ratio x of calcium by tin is shown in Fig. 5-8. Unfortunately, the chemical analysis of only a few pure microcrystalline samples was carried out. It shows that the CaF_2 structure can substitute only about one third of Ca by Sn, i.e. the upper limit of the solid solution is about $Ca_{0.67}Sn_{0.33}F_2$, (which can be also written as Ca_2SnF_6). At the limit of the solid solution, i.e. for x ~ 0.33, an increase of ca. 2% of the unit-cell parameter, with the respect to CaF_2, is observed.

5.4. Mössbauer Spectroscopy

All spectra consisted of a quadrupole doublet characteristic of divalent tin with a hybridized lone pair of electrons. The Mössbauer parameters, δ chemical isomer shift relative to $CaSnO_3$ at room temperature, and Δ quadrupole splitting for both kinds of samples are given in Table 5-4, together with literature values for α-SnF_2, α-$PbSnF_4$ and $BaSnF_4$, for comparison. The isomer shift and quadrupole splitting for microcrystalline $Ca_{1-x}Sn_xF_2$ are close to the values obtained for α-SnF_2, α-$PbSnF_4$ and $BaSnF_4$, whereas the
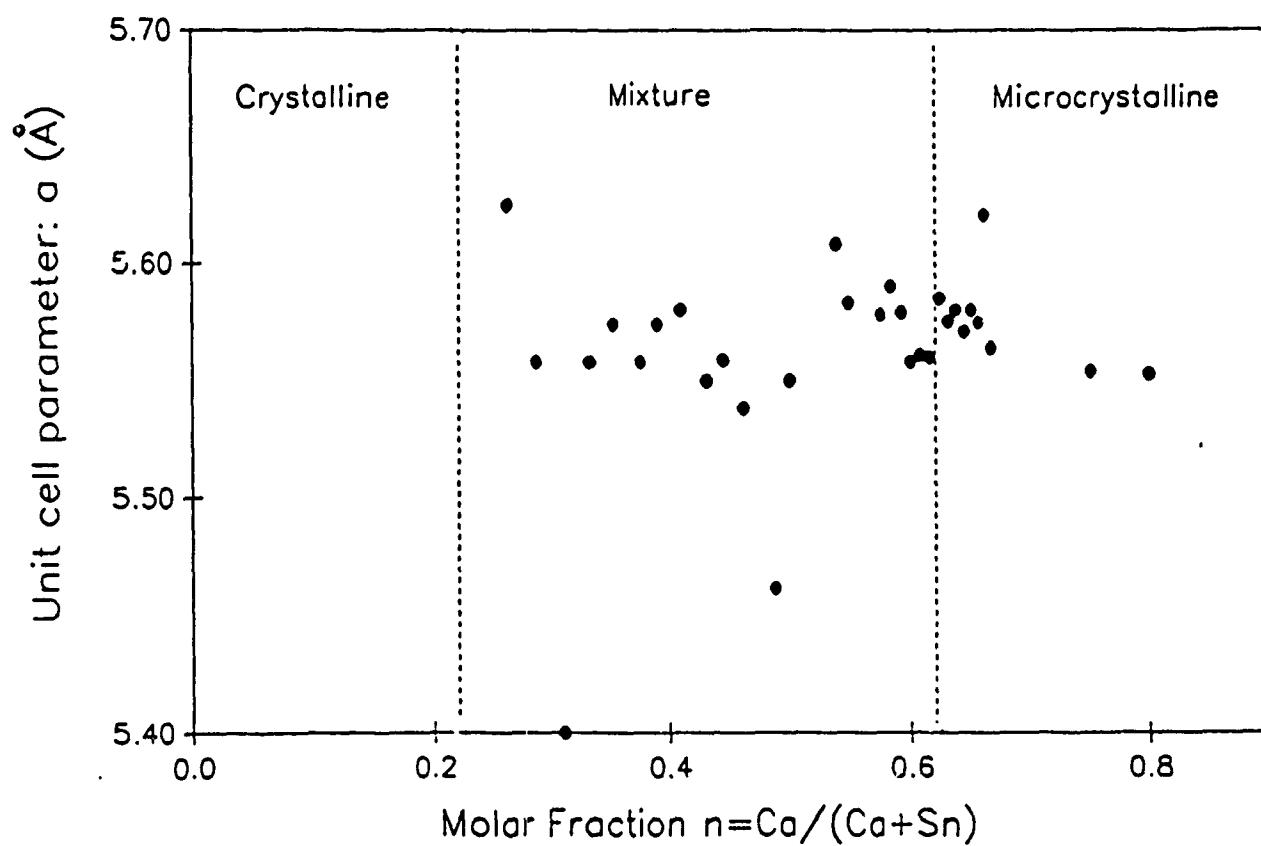
Fig. 5-7. Unit-cell Parameter of the $Ca_{1-x}Sn_xF_2$
Microcrystalline solid solution as a Function
of the Molar Fraction in the Reaction Mixture
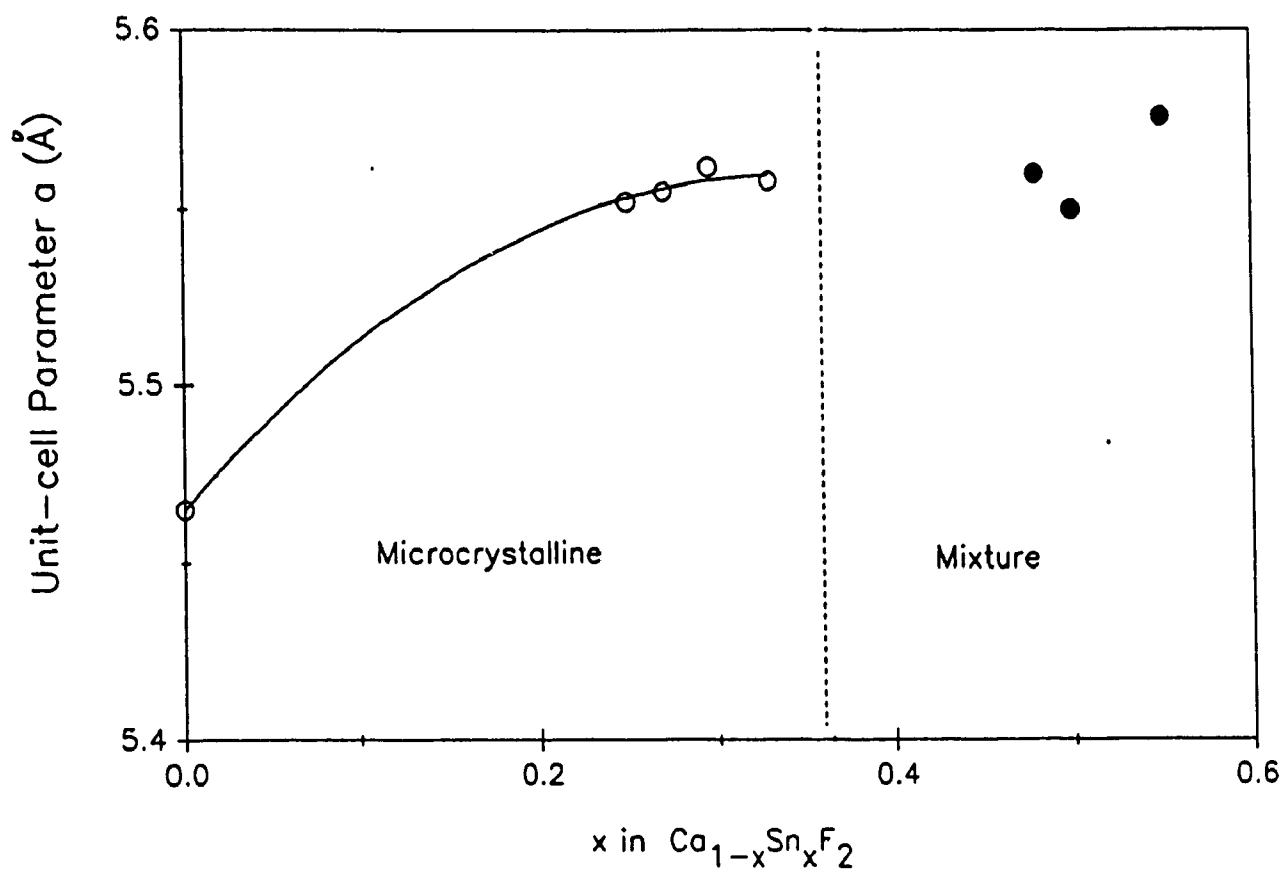
**Fig. 5-8 Unit-cell Parameter a of the Microcrystalline $Ca_{1-x}Sn_xF_2$
Fluorite-type Phase as a Function of the Tin Substitution Ratio**

Table 5-4. Mössbauer Parameters in the SnF_2/CaF_2 System

Compound	δ(mm/s)	Δ(mm/s)	Reference
$CaSn_2F_6$(n=0.048)	3.18	1.90	This work
$Ca_{1-x}Sn_xF_2$(n=0.80)	3.32	1.60	This work
α-SnF_2	3.43	1.532	[36]
α-$PbSnF_4$	3.252	1.524	[14]
$BaSnF_4$	3.255	1.518	[14]

δ: ^{119}Sn Chemical Isomer Shift (Relative $CaSnO_3$ at room temperature).

Δ: ^{119}Sn Quadrupole Splitting.

values for $CaSn_2F_6$ show a smaller isomer shift and a larger quadrupole splitting. The values found for all samples are characteristic of a hybridized $5s^{2-x}5p^x$ tin(II) with a significant amount of p contribution to the lone pair, which is responsible for the large quadrupole splitting. $CaSn_2F_6$ has more p electron density in the lone pair, as shown by a larger value of the quadrupole splitting. This implies that more s electrons are used for bonding, and this is shown by a smaller isomer shift. Mössbauer spectroscopy shows unambiguously that the tin lone pair is hybridized, and this has two very important implications on the structures and the properties of these materials (see Appendix X):

(i) The lone pair of tin is not engaged in bonding, therefore one could be tempted to think that it can be used to populate the conduction band to give rise to electronic conduction (semiconduction). This situation, which is found only when tin is surrounded by large anions (Br or I) in a highly symmetrical environment, gives high isomer shifts ($\delta \approx 4$ mm/s) and very small quadrupole splittings ($\Delta \approx 0$ mm/s) due to the absence of p contribution to the lone pair and high-site symmetry at tin, such that the electric field gradient (e.f.g.) at tin is nearly zero[37]. Such a situation has never been found when fluoride is the ligand

71

and the Mössbauer parameters of both the crystalline and microcrystalline materials show that it is not the case. Therefore, in our products, the lone pair is highly localized on each tin(II) atom and does not give rise to electronic properties. It results that the conducting properties described in the next chapter are due to either ionic motion, or electronic motion not involving a mobile lone pair.

(ii) The significant non-s electron density of the lone pair, characterized by the large quadrupole splitting observed by Mössbauer spectroscopy, shows that the lone pair is located on a hybridized orbital. Hybridization involves the 5p orbitals and often also the 5d orbitals; the latter are empty and therefore bonding with 5d orbitals involves coordination bonds with Lewis base ligands. The most commonly encountered hybridizations and coordinations are (X are ligands and E is the lone pair):

- sp^3: SnX_3E pseudo-tetrahedral, such as for Sn(1) in α-SnF_2[35];

- sp^3d: SnX_4E pseudo-trigonal-bipyramidal, such as in γ-SnF_2[38];

- sp^3d^2: SnX_5E pseudo-octahedral, such as in α-$PbSnF_4$ and $BaSnF_4$[14].

The less common square pyramidal coordination SnX_4E was known until recently only in black SnO[39]. However, recent studies have shown that it also occurs in $PbSn_4F_{10}$[40]. It is most likely that the coordination of tin in crystalline $CaSn_2F_6$ is one of the above, with the possibility of a significant amount of distortion (i.e. unequal bond lengths and bond angles). In the absence of single crystals, it is difficult to say more about the structure of $CaSn_2F_6$ at the present time. On the other hand, more information can be derived about the microcrystalline phase:

a) Since the X-ray diffraction pattern of the microcrystalline $Ca_{1-x}Sn_xF_2$ solid solution contains the same lines as the powder pattern of CaF_2, characteristics of the F lattice of the fluorite-type, and since the general formula of the material is MF_2 (M=a mixture of Ca and Sn), the structure of the microcrystalline phase is the MF_2 fluorite-type as in CaF_2, β-PbF_2 and BaF_2. Figure 5-9 (a) shows a projection of the fluorite type structure onto one of the faces of the cubic unit-cell. Only the ions located in the range of coordinates y=-¼ to y=+¼ are shown for clarity (layer A). An identical layer, layer B, shifted by $\vec{a}/2$ (or $\vec{c}/2$) is located below and above the layer A shown on the figure, and the whole structure is built up by the stacking of these alternating layers, all identical but shifted relative to one another, to give the layer sequence ...A B A B...

Figure 5-9 (a) shows that the fluorite structure is made of F_8 cubes of fluoride ions forming rows by sharing of faces, along the $\bar{a}$ and c axes. Stacking of the layers gives also rows of F_8 cubes along b, which makes these materials perfectly three-dimensional and isotropic (since their symmetry is cubic). It should be pointed out that the fluorite structure consists of rows of alternating MF_8 cubes and $\square F_8$ cubes ($\square$=vacancy, i.e. $\square F_8$ cubes have no metal ion in their center), and these rows are parallel to the three axes of the unit-cell.

b) Chemical analysis and Mössbauer spectroscopy show the microcrystalline phase contains tin and therefore, it is not simply pure microcrystalline CaF_2. However, the material could be a mixture of microcrystalline CaF_2 and an amorphous tin(II) fluoride containing phase. Such a mixture would show the presence of tin in chemical analysis, would give a tin-119 Mössbauer spectrum and, by X-ray diffraction, it would give only broadened Bragg peaks for the microcrystalline CaF_2 component and no peak for the amorphous tin(II) fluoride containing phase. However, if the microcrystalline phase was unsubstituted CaF_2, its unit-cell parameter would be the same as that of crystalline CaF_2. Appendix IX shows that our measured value of the unit-cell parameter of CaF_2 agrees well with literature, and that most of the values for the microcrystalline phase are about 2% higher. This clearly proves that the microcrystalline phase, although it has the overall periodicity of CaF_2, is doped with tin, i.e. some of Ca is replaced by tin, and a $Ca_{1-x}Sn_xF_2$ solid solution of variable composition has been prepared.

c) In the CaF_2 fluorite-type structure, Ca is in a regular cubic environment, i.e. each Ca is surrounded by eight F located at the apices of a cube, and Ca is located at the center of this cube (Fig. 5-9 (a)). If tin is substituted for some of the Ca ions in the undistorted CaF_2 type structure, one would expect Sn to be also located at the center of a cube of eight fluorides ions. However, the Mössbauer spectroscopic results show that the tin lone pair is hybridized, i.e. stereoactive, and therefore, tin cannot take a regular coordination. To the contrary, it will most likely take one of the highly distorted coordinations described earlier, i.e. SnF_3E pseudo-tetrahedral, SnF_4E pseudo-trigonal-bipyramidal, SnF_4E square-pyramidal or SnF_5E pseudo-octahedral, with the lone pair E occupying one of the apices of the polyhedron of coordination. The two contradictory requirements, i.e. the cubic sublattice of fluorine and the highly distorted and low coordination

73
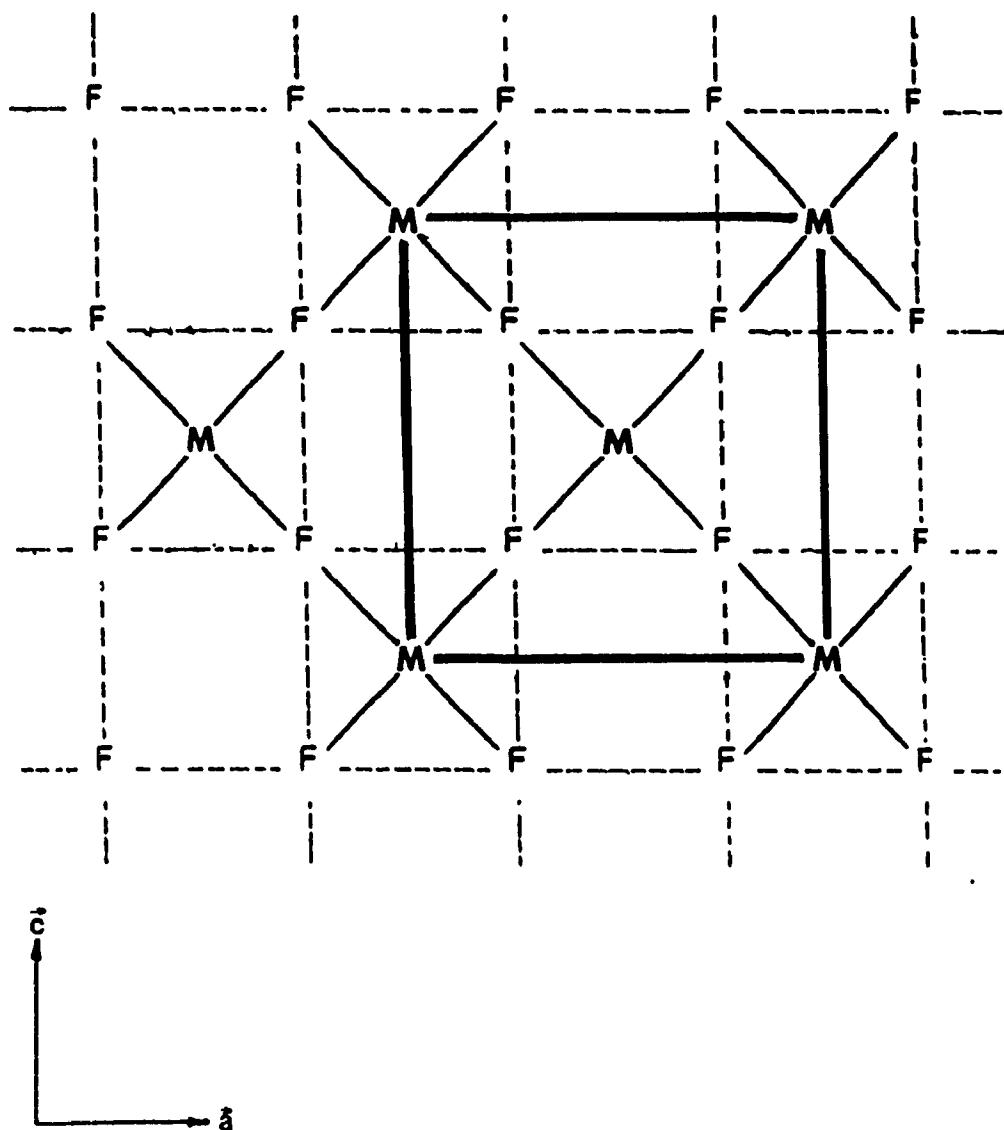
Fig. 5-9(a) Projection of a Layer , Half a unit-cell Thick (from y=-¼ to +¼), of the MF Fluorite-type (M=Ca, Pb and Ba) onto the (a, c) Plane

The dashed lines show the sublattice of fluoride ion cubes, the solid line represent the M-F bonds and the thick lines give the unit-cell. All M's shown on the figure are at y coordinates 0, and all F's at y=-¼ and +¼.

74

(3 to 5) of tin, seem to indicate that the substitution of metal ion (in regular cubic coordination) by tin(II) with it stereoactive lone pair, is simply impossible. However, Denes et al [41] have found that it can occur in at least two different ways:

c.1.) Tin (II) and the other metal can order: case in the α-PbSnF$_4$ type structure. In isostructural α-PbSnF$_4$ and BaSnF$_4$, tin and the metal order perpendicularly to the c axis of the unit cell [14,41]. The metal sequence is ...Sn Sn M M ... . Fig. 5-9(b) shows that the structure consists of a double layer of alternating MF$_8$ cubes and F'F$_8$ cubes sandwiched between two layers of tin and its lone pair,. This assembly makes a [ESnF$_2$(F'M)F$_2$(MF')F$_2$SnE] sheet parallel to ($\vec{a}$, b), which has no connection to neighbouring sheets, since the fluoride ion layer that would have linked them if tin had a cubic coordination has moved into the F$_8$ cubes non-occupied by a metal M, forming F'F$_8$ cubes. The tin atoms of two adjacent layers experience very little attractive interactions; on the other hand, they experience lone pair repulsions from neighbouring tin atoms of adjacent layers. This type of metal ordering gives very highly anisotropic structures and is easily detected by X-ray powder diffraction because the metal ordering gives superstructure Bragg peaks and the symmetry break (cubic symmetry is not possible in these anisotropic structures) results in splitting of many Bragg peaks. Since no new Bragg peak (superstructure or symmetry break) is observed in microcrystalline Ca$_{1-x}$Sn$_x$F$_2$, the tin and calcium atoms cannot be ordered.

c.2) Tin(II) and the other metal can be disordered: as in the case of the Pb$_{1-x}$Sn$_x$F$_2$ solid solution (0<x≤0.30) and PbSn$_4$F$_{10}$. In the case of the Pb$_{1-x}$Sn$_x$F$_2$ solid solution (0<x≤0.30) and PbSn$_4$F$_{10}$, X-ray powder diffraction shows that these compounds crystallize in the F cubic lattice of the fluorite-type [40,42]. Disorder on the metal sublattice is characterized by the absence of superstructure and of peak splitting, yet Mössbauer spectroscopy shows that tin(II) is hybridized in the $5s^{2-x}5p^x$ form. Therefore the tin lone pair is stereoactive and tin(II) cannot take the cubic coordination of lead [40, 41]. This is similar to the situation of the microcrystalline Ca$_{1-x}$Sn$_x$F$_2$ solid solution. In the absence of order and of symmetry break, three types of disorder must be present:

- disorder of the metal sites where substitution by tin takes places;
- disorder of orientation the tin-lone pair axis;

75
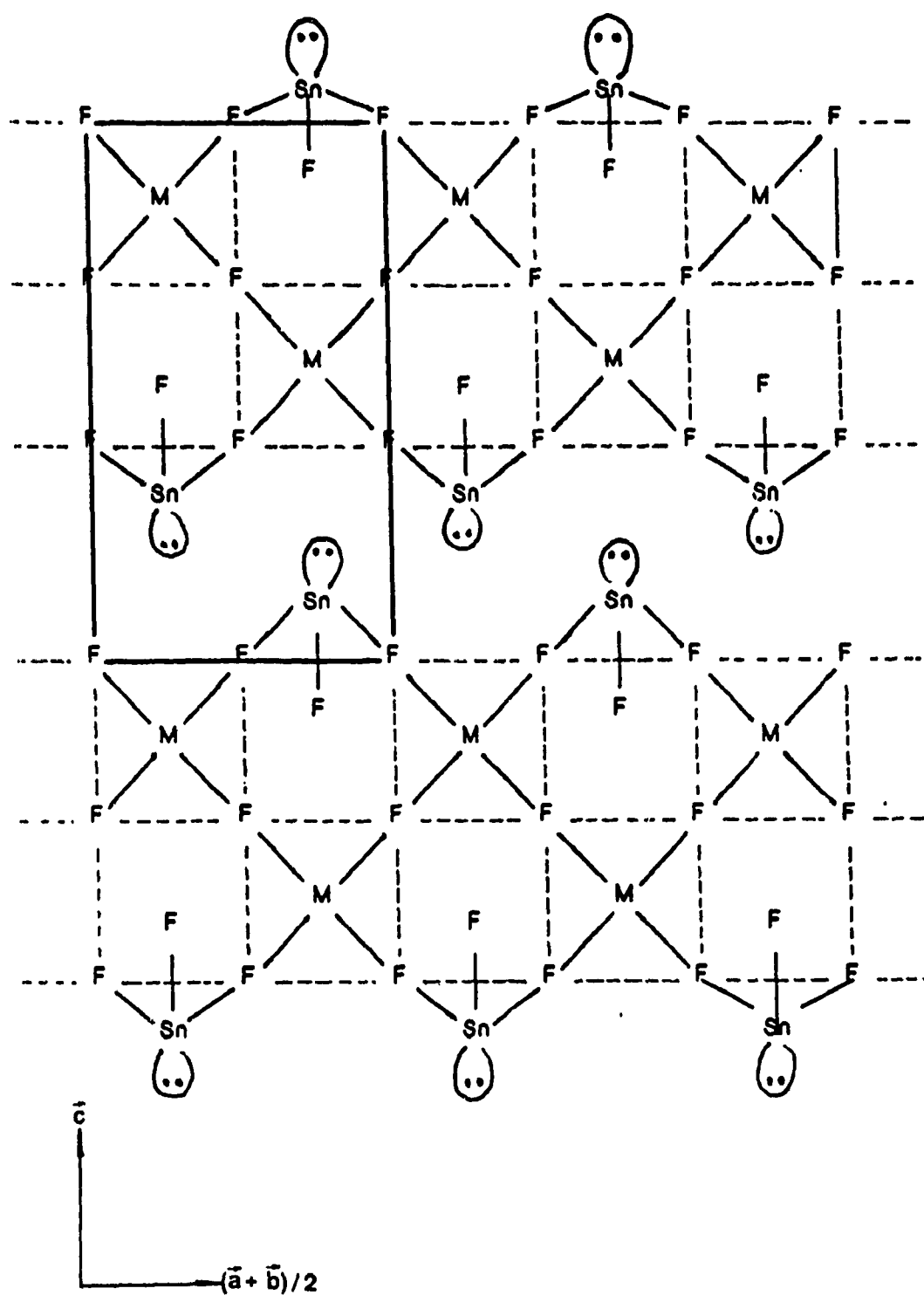
Fig. 5-9(b). Projection of the Structure of $MSnF_4$ (M=Pb, Ba) onto the $(\vec{a'}, \vec{c})$ Plane, where $\vec{a'} = (\vec{a} + \vec{b})/2$

- disorder of the local distortion of the concerned F_8 cubes.

Figure 5-9 (c) shows the structural model proposed by Denes et al [43]. for the $Pb_{1-x}Sn_xF_2$ cubic solid solution. It is proposed that the fluoride ion sublattice remains cubic, identical to that present in the fluorite-type. Tin and lead are randomly disordered and the number of sites where substitution has taken place is determined by the substitution rate x of the solid solution $M_{1-x}Sn_xF_2$. However, tin possesses a stereoactive lone pair of electrons, as shown by Mössbauer spectroscopy, therefore it cannot be located in the center of the F_8 cubes. Instead, Denes et al. [43] have proposed that tin is shifted from the center of the fluoride cube, towards one of its faces, and form four equal Sn-F bonds. This gives tin a SnF_4E square pyramidal coordination similar to that found in SnO [39]. The tin lone pair is located at, or near, the center of the F_8 cubes. This creates strains within the concerned F_8 cubes and most likely results in local distortion of the cube. However, these distortions are disordered over all the cubes where substitution takes place, which are themselves disordered. In addition, the tin-lone pair axis, which can take six different orientations (tin can form bonds with any of the six faces of the cube) must be orientationally disordered in order to conserve, on average, all the symmetry elements of the Fm3m space group of the fluorite-type, and without superstructure.

c.3) The case of the microcrystalline cubic $Ca_{1-x}Sn_xF_2$ solid solution: Since the $Ca_{1-x}Sn_xF_2$ solid solution has the same X-ray powder diffraction pattern as that of the fluorite-type and Mössbauer spectroscopy shows that the tin(II) lone pair is stereoactive, it is most likely that Ca and Sn are disordered as in the $Pb_{1-x}Sn_xF_2$ solid solution and $PbSn_4F_{10}$. When lead is the other metal, the fluoride cubes are large enough to accommodate the presence of tin(II) and its lone pair, although it is a tight fit[40]. However, in CaF_2, the edge of the F_8 cube is 8% smaller and therefore the cubes cannot accommodate tin(II) and its lone pair without serious local distortion. A model of the structure of $Ca_{1-x}Sn_xF_2$ is shown on Fig.5-9(d). The tin substitution sites and the orientation of the tin lone pair axis are disordered. Because of the small size of the F_8 cubes, the tin lone pair pushes neighbouring fluoride ions away, which creates much more distortions than in the case of $Pb_{1-x}Sn_xF_2$. Of course, these local distortions are also disordered since no cell distortion, symmetry break or superstructure is observed by X-ray powder diffraction.
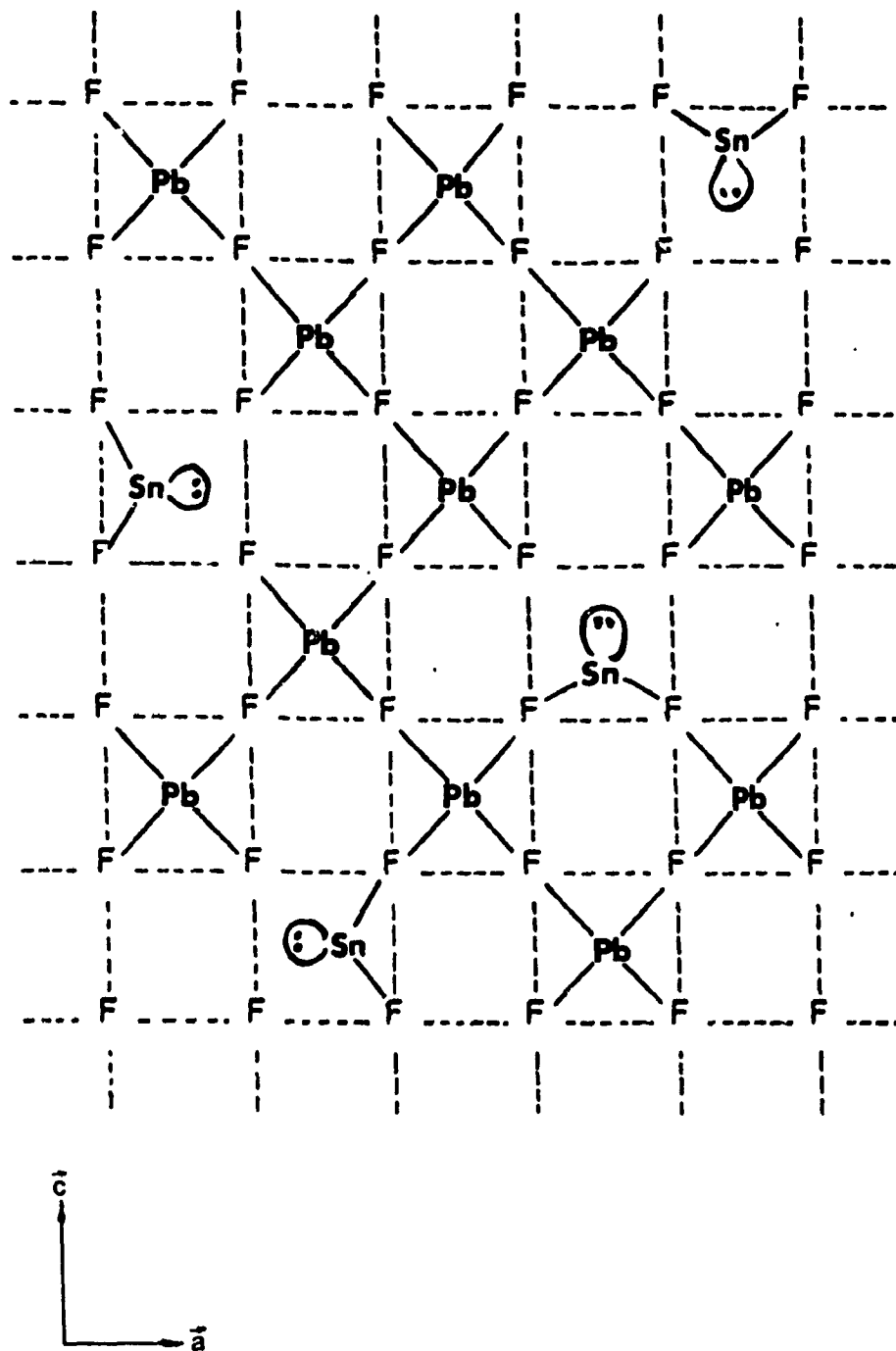
Fig. 5-9(c) Projection of a Model of the Structure of the
$Pb_{1-x}Sn_xF_2$ Cubic Solution onto the $(\vec{a}, \vec{c})$ Plane
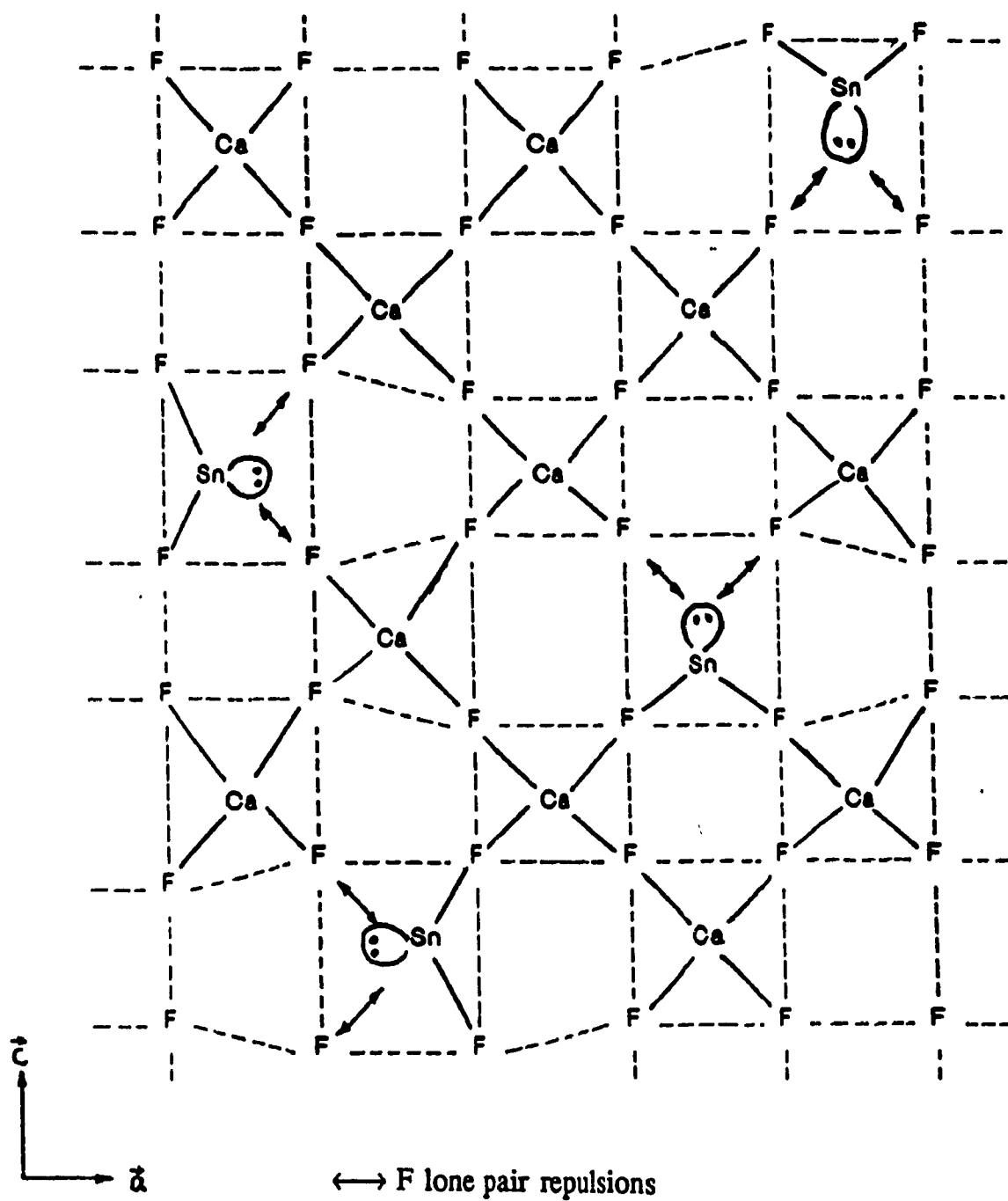
Fig. 5-9(d) Projection of a Model of the Structure of the
$Ca_{1-x}Sn_xF_2$ Cubic Solution onto the $(\bar{a}, \bar{c})$ Plane

5.5. Bulk Density

Bulk density measurements are very useful because the density contains information about the degree of packing of a solid and therefore it gives an insight into the packing efficiency, which can be related in some cases to the stability of solid structures. It also makes possible the calculation of the number of molecular formulas per unit-cell when the volume of the unit-cell is known, which is very useful for solving crystal structures.

The bulk density results for some of the samples are given in Fig. 5-10 and in Appendix XI. Figure 5-10 shows that the density of the crystalline phase is constant within experimental error. This is expected since the composition of the phase is constant (Fig. 5-4). For all values of the molar fraction in the reaction mixture, the density is lower than the average of the densities of α-SnF_2 and CaF_2 (dashed line). However this may not be significant since the composition of the product is not the same as that of the reaction mixture that produces it. The plot of the bulk density versus the substitution ratio x in $Ca_{1-x}Sn_xF_2$ (Fig. 5-11) is much more informative. The density for three of the pure microcrystalline samples and for the crystalline phase are shown by closed circles ($\cdot$). For the microcrystalline phase, one can calculate the theoretical density, since the unit cell parameter has been measured by X-ray diffraction and the chemical composition is known from chemical analysis.

$\rho = m/V$ by definition   (5.4)

ρ = density

$V = a^3$ is the volume of the cell, in a cubic lattice   (5.5)

$m = MZ/N$ is the mass of one unit-cell   (5.6)

M = molecular weight

Z = number of molecular formulas per unit-cell; $Z=4$ in the fluorite structure

N = Avogadro's number = 6.023×10^{23} molecules/mole.

Combining (5.4), (5.5) and (5.6), the theoretical density ρ_c can be written as:
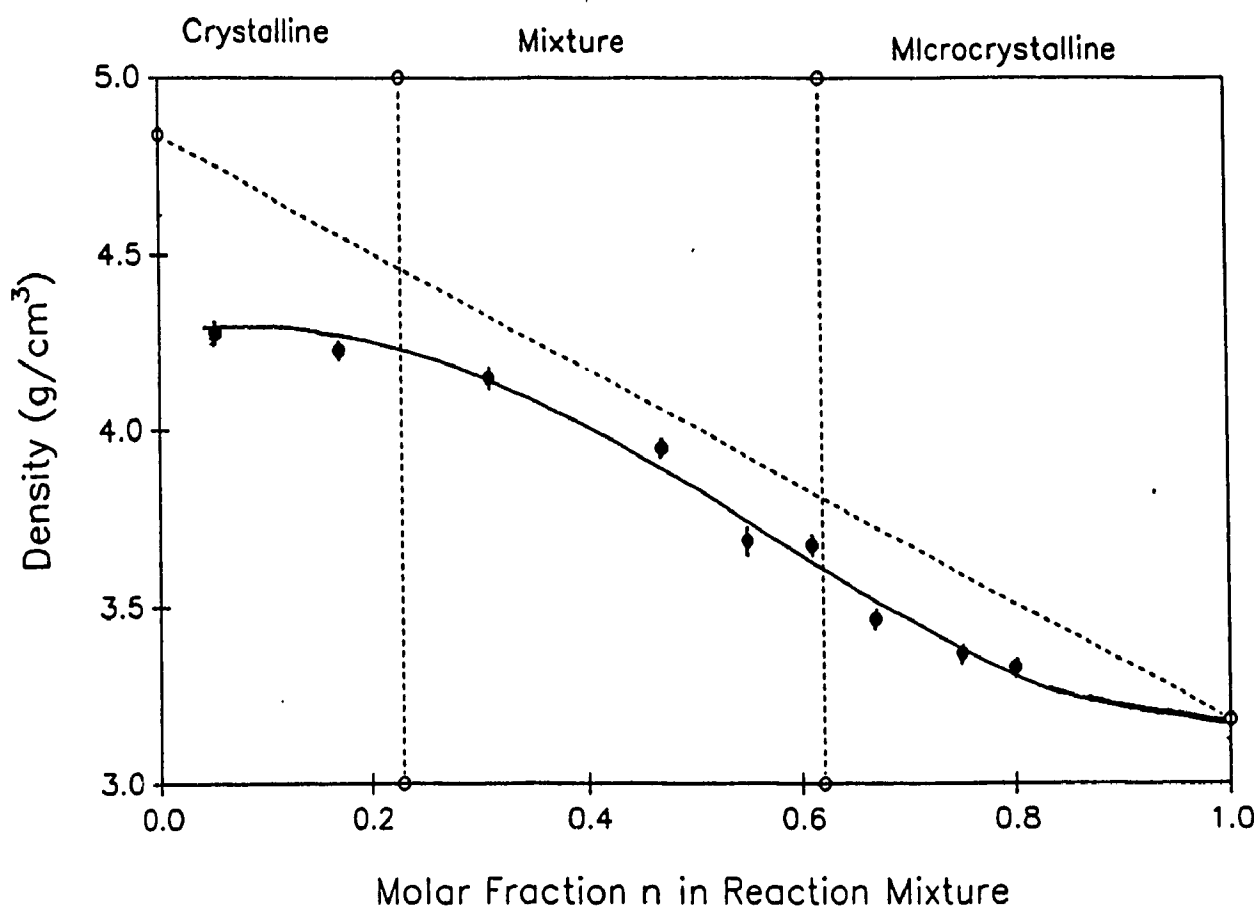
Fig. 5-10. Density of the SnF_2-CaF_2 System versus the

Ca Molar Fraction in the Reaction Mixture
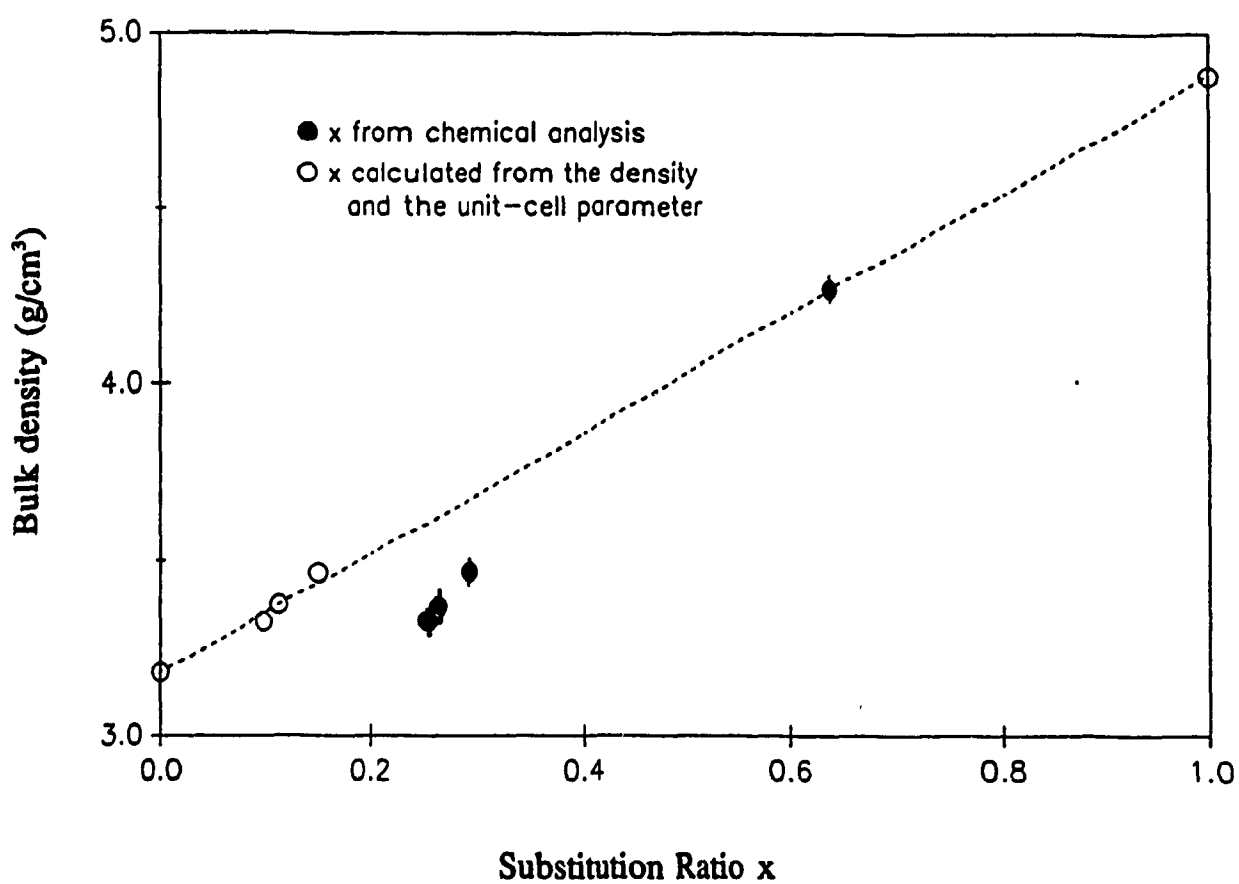
Fig. 5-11 Bulk Density of the CaF_2-SnF_2 System versus the Tin Substitution Ratio x in $Ca_{1-x}Sn_xF_2$

$$\rho_c = \frac{MZ}{NV} = \frac{4M}{0.6023a^3} \quad \ldots \ldots (5.7)$$

where ρ_c is in g/cm^3, M in g and a in Å.

Calculation of ρ_c for the three microcrystalline samples gives values which are 12 to 14% higher than the measured densities (Appendix XI). The difference is much higher than the dispersion of the three measured values for each sample (1-2%). It is also much higher than the difference between the measured and calculated values for α-SnF$_2$ (ρ_c = 4.88, ρ_m = 4.84, $\Delta\rho$ = 0.8%). Therefore, the difference between measured and calculated densities for the microcrystalline phase are not due to experimental errors. Since Z and V are accurately determined by X-ray powder diffraction, the only parameter in equation (5.7) that could be doubtful is the molecular weight M. As M was determined from chemical analysis, (and since no other Bragg peak than those of microcrystalline $Ca_{1-x}Sn_xF_2$ fluorite-type was observed (Fig. 5-5(b)), it is reasonable to assume that all the tin determined by chemical analysis had substituted calcium on the metal site of the fluorite structure, which is witnessed by the increase of the unit-cell parameter. However it must be emphasised that only a fraction of the tin present in the solid may have substituted for Ca in CaF$_2$ to give $Ca_{1-x}Sn_xF_2$. The rest of the tin could be present as an amorphous or microcrystalline fluoride, with or without calcium, and the absence of long range order (if amorphous) or the very small particle size ($\leq$ ca. 40 Å, if microcrystalline) would prevent detection by X-ray powder diffraction. This amorphous or microcrystalline phase could give a Mössbauer quadrupole doublet indistinguishable from that of $Ca_{1-x}Sn_xF_2$ since the Mössbauer parameters for divalent tin with a stereoactive lone pair are dominated by the electronic imbalance due to the lone pair and the nature of the ligand. This has already been observed, for example in α-SnF$_2$, where the two kinds of tin(II), crystallographically very different (one is in a SnF$_3$E pseudo-tetrahedron, the other in a SnF$_5$E pseudo-octahedron) give indistinguishable Mössbauer parameters [36]. The real substitution rate in the microcrystalline phase can be calculated from the measured density and the unit-cell parameter determined by X-ray diffraction. The real molecular weight of the $Ca_{1-x}Sn_xF_2$ phase, with an unknown substitution rate x can be derived from equation (5.7), using the measured density ρ_m instead of ρ_c, to give (5.8):

$$M = \frac{0.6023a^3\rho_m}{4} \quad \ldots \ldots (5.8)$$

The molecular weight M is related to the atomic weights of Ca, Sn and F, i.e. M_{Ca}, M_{Sn} and M_F, respectively:

$$M = (1-x)M_{Ca} + xM_{Sn} + 2M_F. \quad \ldots \ldots (5.9)$$

Applying the numerical values of the atomic weights to (5.9) gives (5.10):

$$M = 78.076 + 78.61x. \quad \ldots \ldots (5.10)$$

and combining (5.8) and (5.10) gives (5.11):

$$x = 0.0019155a^3\rho_m - 0.9932 \quad \ldots \ldots (5.11)$$

Applying the measured unit-cell parameter a and measured density ρ_m to each of the three microcrystalline samples gives the real substitution ratios (appendix XI). It is clear that the real substitution ratios are much lower than those calculated from chemical analysis and that for all three samples, at least half of the tin contained in the samples has not substituted Ca in the microcrystalline phase, and therefore is present as a much smaller particle sized microcrystalline or amorphous phase. The results, plotted on Fig. 5-11 (open circles), show that the three points are, within experimental errors, located on the straight line representing the average of the densities of CaF_2 and α-SnF_2. This indicates that these compounds are probably not thermodynamically very stable since there is no reduction of volume when Ca^{2+}, Sn^{2+} and F are packed together, relative to the volumes of α-SnF_2 and CaF_2.

5.6. Stability of the Two Phases

5.6.1. Stability in Aqueous Solutions

Immediately after reaction, the precipitates were filtered and washed with doubly distilled water, according to the procedure described in 3.1.1. Since the precipitates are obtained from aqueous solutions and washed with water, it is quite logical to assume that they are stable in the presence of water. However,

this does not rule out that there could be an effect of the ratio precipitate / water, the time of exposure to water and the efficiency of exposure (i.e. the effect of stirring). Such an effect could explain, in addition to the effect of stirring described in 5.3.2., some of the difficulties that we experienced in obtaining reproducible results, especially in the wide zone of reaction mixture ratios, where a mixture of the crystalline and the microcrystalline phases are obtained. However, since the study of the stability in the presence of water was not the goal of this project, only two tests were performed on crystalline $CaSn_2F_6$. A weighed amount of solid (0.7 to 0.8 g) was suspended in 100 ml of doubly distilled water and stirred at medium speed for 1 hour. The white precipitate was filtered, washed and dried according to the same procedure as that used after each synthesis. Then, the solid washed samples were characterized by elemental analysis and X-ray powder diffraction. The water used for washing was allowed to evaporate to dryness and the solid residue was also characterized by chemical analysis, Mössbauer spectroscopy and X-ray powder diffraction. The analytical results are summarized in Table 5-5. The two crystalline samples of $CaSn_2F_6$ (n=0.05 and 0.17) shows a drastic reduction of the tin content (about 50 % reduction), while

Table 5-5. Chemical Analysis of Washed $Ca_{1-x}Sn_xF_2$ Samples

n	Before Washing		Precipitate After Washing		Solid Residue After Evaporation	
	m (g)	x	m (g)	x	m (g)	x
0.05	0.8363	0.62	0.3053	0.35	0.4312	0.96
0.17	0.7129	0.62	0.2486	0.28	-	-

n = Ca/(Ca+Sn) in reaction mixture;

x = Substitution ratio of Ca by Sn in $Ca_{1-x}Sn_xF_2$, x was calculated

from the Sn and Ca analysis

the solid residue after evaporation of the water used for washing is basically free of calcium. Both samples

lost ca. 65% weight upon washing and the residue obtained after evaporation of the water used for washing

one of the sample (n=0.05) weighed 52% of the weight before washing. The analytical results are

corroborated by X-ray powder diffraction. Fig. 5-12 compares the diffraction pattern of crystalline $CaSn_2F_6$

with that of the products obtained after washing. The washed precipitate gives the X-ray powder pattern

(Appendix XII) of the fluorite type with a = 5.552 Å, which is similar to the values obtained for substitution

ratios of ca. x = 0.20 - 0.25. The average particle diameter for this phase is 504 Å, which is significantly

larger than the values of 350 - 400 Å obtained on unwashed microcrystalline sample, however, it is still a

clear sign of microcrystallinity. The precipitate after washing (Fig. 5-12) also shows a very broad peak in

the foot of the (111) microcrystalline Bragg peak. Hints of a similar peak at (200) are also visible, although

it is far less clear. This seems to indicate the presence of a second microcrystalline fluorite-type phase with

a ≈ 5.9 Å (not accurate because the peak position is hard to measure) and a particle diameter of 41 Å.

Therefore, it is obvious that $CaSn_2F_6$, when suspended in H_2O, looses SnF_2 (reaction 5.12) to give two

microcrystalline phases, one of which has very small particle size.

$$(1-x)\ CaSn_2F_6\ \dashrightarrow\ Ca_{1-x}Sn_xF_2 + (2-3x)SnF_2 \qquad (5.12)$$

Applying the measured Ca content (x=0.35, see Table 5-5) into the above equation leads to:

$$0.65\ CaSn_2F_6\ \dashrightarrow\ Ca_{0.65}Sn_{0.35}F_2 + 0.95\ SnF_2 \qquad (5.13)$$

which is very close to:

$$2\ CaSn_2F_6\ \dashrightarrow\ Ca_2SnF_6 + 3\ SnF_2 \qquad (5.14)$$

(for x=0.33). This substitution ratio is close to the limiting rate at the boundary between the pure

microcrystalline and the mixture of microcrystalline + crystalline regions observed on Fig. 5-4. Reaction

5.14 would give a weight loss of 57%, which is a little lower than the measured loss of 63% for the sample

with n=0.05. The loss of SnF_2 by $CaSn_2F_6$ in aqueous solutions probably explains why $CaSn_2F_6$ was found

to be slightly deficient in tin (Appendix III) which means that just 1 or 2% of it had lost SnF_2 to give

$Ca_{0.65}Sn_{0.35}F_2$. However, since the latter is microcrystalline, such an amount could not be detected by X-ray

diffraction. The loss of SnF_2 by the solid suggests that it may be possible to obtain α-SnF_2 as solid residue,

after evaporating to dryness the water used for washing. The X-ray powder pattern of the residue is not the same as that of α-SnF$_2$ [44]; it shows some similarity with that of CaSn$_2$F$_6$ (Fig. 5-12), however it would be surprising to obtain this compound since it contains almost no calcium (x=0.96 for the residue, x=0.67 for CaSn$_2$F$_6$). However, when the beginning of the powder pattern (15-35°(2θ)) is plotted at a larger scale (Fig. 5-13), it is obvious that the two patterns have little in common. Even the first two peaks, which look similar, are not located at the same position: 2θ = 18.56 and 20.55 respectively for the unwashed crystalline phase, and 2θ = 17.61 and 19.95 for the residue. The difference is much larger that the maximum peak shift (Δ(2θ) = 0.08) which has been observed and even if there were some shift, the difference between the position of the two peaks would not change. The difference is 1.99° for the unwashed crystalline phase, and 2.35° fro the residue. Therefore, it is clear the two patterns are different. This is also clear from the comparison of Appendices IV and XIII. A search-match carried out on the powder pattern (Appendix XII) yielded Sn$_7$F$_{16}$ as a very highly probable candidate (Table 5-6). Contrary to the result of the search match for CaSn$_2$F$_6$ (Table 5-1), the similarity index is very high (SI=295), 23 lines are matched and none of the peaks of Sn$_7$F$_{16}$ is unmatched. The quality of the match is shown in Table 5-7, and proves unambiguously that the residue contains Sn$_7$F$_{16}$. Table 5-8 gives the result of the substraction of the powder pattern of Sn$_7$F$_{16}$ from the pattern of the sample. Two thirds of the total intensity of the sample pattern has been removed and therefore belonged to Sn$_7$F$_{16}$. The peaks marked by an arrow on Fig. 5-13 (b) are accounted for by Sn$_7$F$_{16}$. The second best candidate selected by the μPDSM software is SnF$_2$, however, its similarity index (SI = 69) is much too low and there are 7 unmatched peaks. Therefore, there is no ambiguity between the first and second candidate. The main crystalline component in the residue is Sn$_7$F$_{16}$, and not SnF$_2$. This is not surprising since aqueous solutions of SnF$_2$ are known to oxidize slowly , however the product, a white precipitate, is usually amorphous hydrated tin dioxide, SnO$_2$.2H$_2$O [45], the oxidizing species being oxygen dissolved in water. In this case, only two tin (II) out of eight, ie. 25%, are oxidized to tin(IV). Therefore, the overall reaction of oxidation occurring in aqueous solutions is the following:

$$8 \text{ SnF}_2 + \text{O}_2 \longrightarrow \text{Sn}_7\text{F}_{16} + \text{SnO}_2 \qquad (5.15)$$
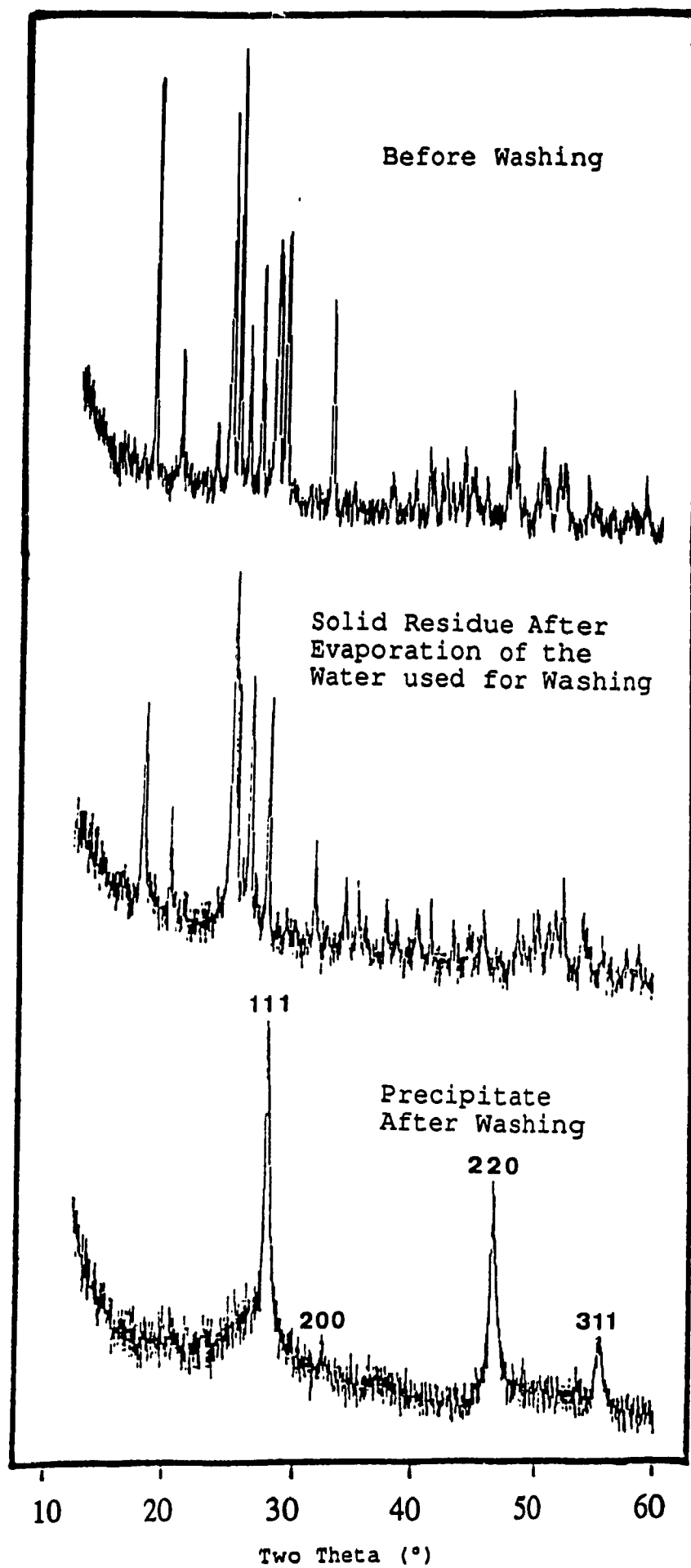
Fig. 5-12. Influence of Washing on the Crystalline Phase
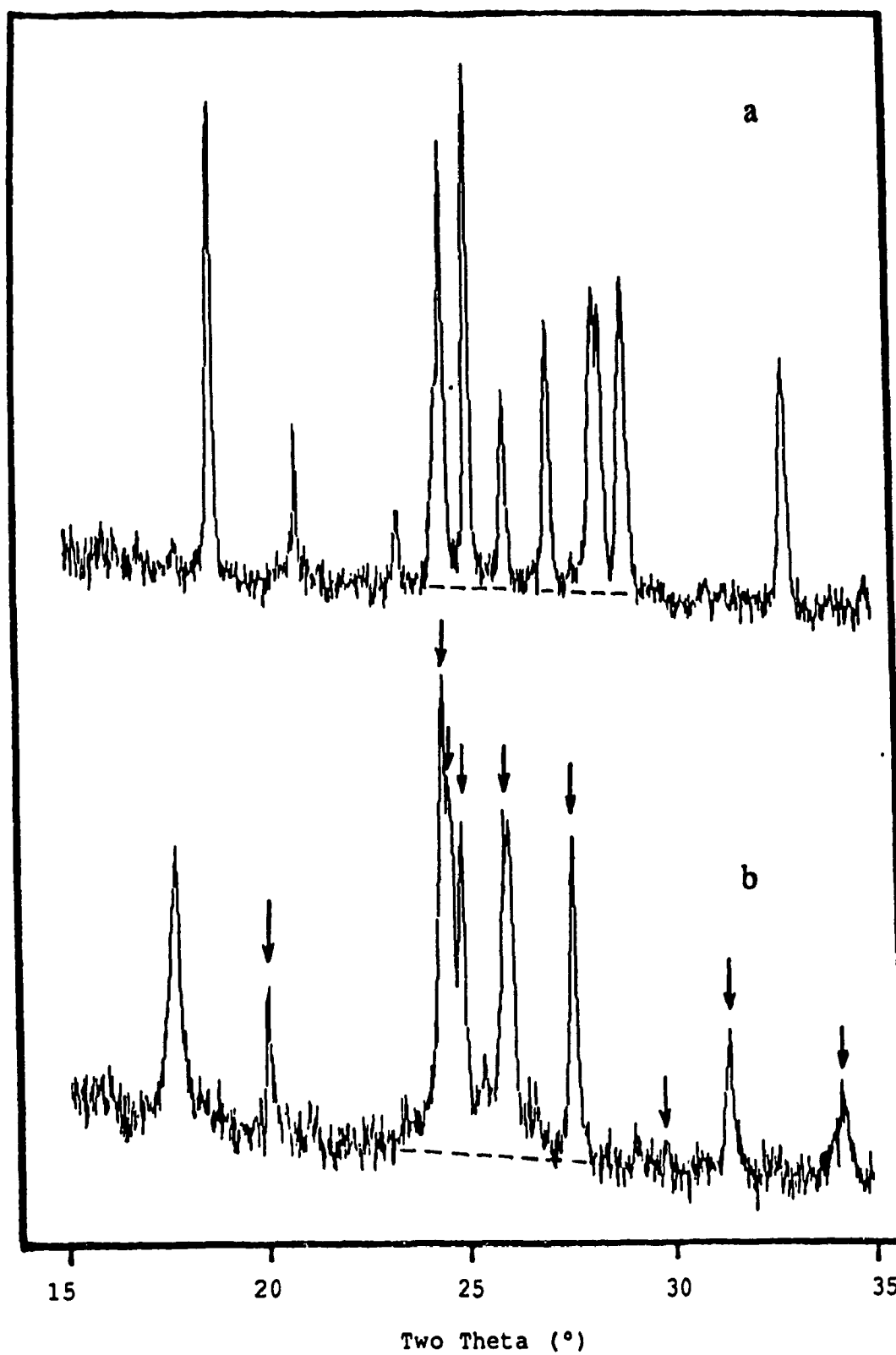
Fig. 5-13. X-ray Powder diffraction Pattern of:(a)Unwashed CaSn$_2$F$_6$; (b) Solid Residue
Obtained upon Evaporation to Dryness of the Water Used for Washing.
(The Peaks indicated by an Arrow are due to Sn$_7$F$_{16}$)

89

Table 5-6. Result of the Search Match for the Residue Obtained by

Evaporation of the Water used for Washing $CaSn_2F_6$

```
 JCPDS#——SI——ML/X——At%——Identity . . . .
F1

F2
    Search Results [21 Entries]
28-1389  295*  23/0  87  Tin Fluoride = Sn7F16
15-0744*  69   11/7  85  *Tin Fluoride = SnF2
24-1342   50    4/1  15  Tin Oxide = SnO
14-0140D  47   10/8  33  Tin Oxide Hydroxide / Hydroromarchite, syn = Sn3O▒
7-0195    32    8/2  31  Tin Oxide = SnO
21-0398   21    5/4  16  Ice = H2O
36-18670  21    4/5  51  C.I. Pigment Yellow 154 =
36-18800  19    4/1  23  C.I. Pigment Orange 52 =
36-18680  17    2/2  51  C.I. Pigment Yellow 151 =
3-0188    15    5/4  17  Ammonia Cellulose =
33-1374   14    2/1  22  Tin Oxide = SnO2
23-0430C  13    2/2  46  Calcium = Ca
1-0735D   13    2/3  52  Calcium = Ca
22-0623   13    5/3  25  Ice = H2O
22-0520D  12    2/2  46  Calcium = Ca
    Ierr:50,150  derr:4.0  Bground:6    dmax/min:7.358/1.540
    Test Results [ 0 Entries]
Plot Shift+F8——Hold F1 F2——Copy Ins——Test F7——Match F8——Subtract F9——Exit Esc
```

Table 5-7 Matching Table of Sn_7F_{16} with the Residue Obtained by Evaporation of the Water Used for Washing $CaSn_2F_6$

JCPDS#	SI	ML/X	At%	Identity . . .		
28-1389	295*	23/0	87	Tin Fluoride = Sn7F16		
	Ierr:50,150		derr:4.0	Bground:6	dmax/min:7.358/1.540	
						* Obscured Lines

28-1389 @ 86.8%		User Pattern			Resid
d	I	d	I	derr	I
4.46	12	4.446	28	-0.7	16
3.62	78	3.573	67	-3.6	None
3.60	87	3.633	100	+2.5	None
		3.484	16	+6.4	
3.41	69	3.411	68	+0.1	None
		3.333	12	-6.6	
3.24	78	3.220	62	-1.9	None
		3.056	7	+6.2	
3.00	8.7	2.9850	6	-1.7	None
		2.9130	8	+4.3	
		Below Background			
2.877	2.6	2.8440	29	-4.0	
		2.5380	18	-1.2	None
2.546	30	2.3350	9	+0.4	6
2.333	3.5				
		Below Background			
2.313	3.5	2.2370	14	+1.0	9
2.232	5.2	2.1790	17	-0.8	None
2.183					
2.129	4.3	Below Background			

28-1389 @ 86.8%		User Pattern			Resid
d	I	d	I	derr	I
2.090	16	2.0860	11	-0.9	None
2.046	17	2.0340	8	-2.9	None
2.033	26	2.0180	10	-3.6	None
1.990	30	1.9870	14	-0.8	None
1.936	5.2	Below Background			
1.908	6.9	1.9000	8	-2.2	None
1.886	4.3	1.8800	11	-1.7	7
1.864	17	1.8590	6	-1.4	None
		1.8440	6	+2.4	
1.836	5.2	1.8330	12	-0.9	None
+ 1.822	2.6			+3.3	None
1.789	10	1.8160	11	-1.8	
1.774	17	1.7860	11	-0.9	None
1.752	22	1.7700	15	-1.3	None
		1.7530	14	+0.3	None
		1.7070	18	+1.7	
1.702	3.5*	1.6980	14	-1.4	11
1.654	2.6*	1.6600	10	+2.2	7

Plot Shift+F8

Return to Tables Esc⌐

91

Table 5-8 Result of the Substraction of the Powder Pattern of Sn_7F_{16}
from the Pattern of the Residue Obtained by Evaporation
of the Water Used for Washing $CaSn_2F_6$

```
|JCPDS#____SI___ML/X__At%__Identity . . . :
|28-1389   295*  23/0   87  Tin Fluoride = Sn7F16
|      Ierr:50,150   derr:4.0  Bground:6   dmax/min:7.358/1.540
|Subtraction
|
|Lines removed: 3.633  3.573  3.411  3.220  2.9850 2.5380 2.1790
|               2.0860 2.0340 2.0180 1.9870 1.9000 1.8590 1.8330
|               1.7860 1.7700 1.7530 1.6020
|
|Lines reduced (d=Inew): 4.446=16      2.3350=6      2.2370=9
|               1.8800=7  1.6980=11    1.6600=7
|
|18 lines removed.     6 lines reduced.      19 lines left.
|34.1% of the original total intensity remains.
|Use MODIFY to make manual adjustments.
|
|
|
|
|                    Press Esc when ready to proceed
```

The redox reaction involved is:

$$2\ Sn^{2+} + O_2 \ \text{------>}\ 2\ Sn^{4+} + 2\ O^{2-} \qquad (5.16)$$
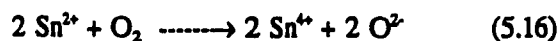
and, expressing the tin oxidation states, the overall reaction can be formulated as follows:

$$8\ Sn(II)F_2 + O_2 \ \text{------>}\ Sn_6(II)Sn(IV)F_{16} + Sn(IV)O_2 \qquad (5.17)$$

Four mixed oxidation states of tin fluorides are known: Sn_7F_{16}, Sn_3F_8, Sn_2F_6 and $Sn_{10}F_{34}$ [46]. All are prepared by reaction of the stoichiometric mixture of SnF_2 and SnF_4 in an inert container[46]. However, Sn_3F_8 has also been obtained upon partial oxidation of SnF_2, in anhydrous HF, with O_2, F_2 or SO_2 [47]. This is the first report of the synthesis of Sn_7F_{16} in an aqueous solution. It should also be pointed out that such spontaneous partial oxidation of SnF_2 in aqueous solution has not been reported earlier, since only complete oxidation to $SnO_2.2H_2O$ was previously known[45]. Crystalline SnO_2 is not observed in the X-ray diffraction pattern of Fig. 5-13(b), therefore one can safely assume that the oxide is the amorphous dihydrate $SnO_2.2H_2O$ previously reported[45], unless it is microcrystalline. A closer examination of Fig. 5-13(b) shows that when the background of the X-ray diffraction pattern from 20 to 30° (2θ) is interpolated underneath the group of peaks located around 25°, there is obviously a very broad peak centered at ca. 25°. Its width is similar to that of the finest particles (average diameter of 41 Å) fluorite type phase observed in washed $CaSn_2F_6$ (Fig. 5-12). In addition, the peak position is also very similar to that of the above mentioned phase. These similarities seams to indicate the presence of a very fine particle sized fluorite type $Ca_{1-x}Sn_xF_2$ rich in calcium, mixed with Sn_7F_{16}. However, chemical analysis (Table 5-5) shows that Ca is present only as an impurity (4% of the metals) and therefore $Ca_{1-x}Sn_xF_2$ (with x > 0.6) could not be responsible for the very broad Bragg peak observed at ca. 25° (2θ). A broad peak at the same position was also observed by M.C. Madamba in her study of the reaction of $Fe(OH)_3$ with SnF_2 [48] and it corresponds to microcrystalline SnO_2 (rutile structure). Therefore, X-ray diffraction, on Fig. 5-13, establishes the presence of the two solids produced, ie. Sn_7F_{16} and SnO_2. It is not known at the present time why some reactions of oxidation of SnF_2 give amorphous $SnO_2.2H_2O$ only, and other give microcrystalline rutile-type SnO_2 or a mixture of microcrystalline SnO_2 rutile and crystalline Sn_7F_{16}. The result of the oxidation is most likely a function of evaporation conditions (duration, temperature) which were not controlled. However,

in all cases, the temperature was ambient temperature and the duration was the time required for evaporation to dryness. Another technique that can easily reveal the presence of tin(IV) oxide is Mössbauer spectroscopy. Fig. 5-14 compares the tin-119 Mössbauer spectrum of crystalline $CaSn_2F_6$ before washing with that of the residue of evaporation; the literature spectrum [49] for Sn_7F_{16} is also shown for comparison. Two obvious major differences are observed between unwashed crystalline $CaSn_2F_6$ and the residue of evaporation: (i)there is a large increase of the tin(IV) line at ca. 0 mm/s, and (ii) the tin(II) doublet becomes strongly asymmetric and the splitting is smaller. These changes are further proof that the residue of evaporation is not $CaSn_2F_6$. In addition, it is clear that the spectrum of the residue is closely related to the literature spectrum for Sn_7F_{16}, i.e. the tin(II) doublet is identical, however, the tin(IV) line for the residue is much more intense. The tin(IV) resonances for Sn(IV) of SnO_2 and of Sn_7F_{16} are indistinguishable. All these observations can be easily interpreted in the light of the reactions that have taken place (eq. 5.15, 5.16 and 5.17). The results are summarized in Table 5-9, which shows the following features:

(i)There is a significant change of isomer shift and quadrupole splitting between the tin(II) sites of $CaSn_2F_6$ and of the residue of evaporation. However these parameters are very similar for the residue and literature for Sn_7F_{16}, which reinforces the diffraction result that Sn_7F_{16} is produced upon evaporation of the water used for washing $CaSn_2F_6$. The g_{11} Goldanskii-Karyagin parameter, which is the ratio of the intensities of the two Mössbauer lines in the case of quadrupole doublet (5.18)

$$g_{11} = \frac{I\pm1/2 \rightarrow \pm3/2}{I\pm1/2 \rightarrow \pm1/2} \quad \ldots\ldots 5.18$$

measures the anisotropy of the thermal vibrations of the Mössbauer nuclide being probed. The symmetric doublet for $CaSn_2F_6$ (Fig. 5-14(a)) gives g_{11} = ca.1, i.e. the tin nucleus vibrates quasi-isotropically. The g_{11} parameter of Sn_7F_{16} is reported in [49] to be equal to 1.42, and this seems correct in view of the strong asymmetry of the divalent tin doublet (Fig. 5-14(c)). This is the same as observed for the residue of evaporation (Fig. 5-14(b)). However, a close examination of Fig. 5-14(b) and (c) shows that the divalent tin line at lower velocity is clearly much broader than the other. Using line amplitudes estimated

Table 5-9. Tin-119 Mössbauer spectroscopic Parameters for Unwashed $CaSn_2F_6$,

the Residue of Evaporation, and Literature Results for Sn_7F_{16} and SnO_2

at Ambient Temperature (see text for details)

Tin Oxidation State	Mössbauer Parameter	$CaSn_2F_6$	Residue of Evaporation	Sn_7F_{16} from Literature[48,49]	SnO_2 from Literature[50,51]
Sn (II)	δ (mm/s)	3.18	3.64	3.696	-
	Δ (mm/s)	1.90	1.49	1.312	-
	g_{11}	ca.1	1.02	1.42	-
	% spectrum	87	33	70	0
	f_a	-	-	0.04	-
	% content:calculated	99	78	89	0
	% content:theoretical	100	75	85.7	0
Sn (IV)	δ (mm/s)	-0.32	-0.36	-0.325	0
	% spectrum	13	67	30	100
	f_a	-	-	0.14	0.44
	% content:calculated	1	22	11	100
	% content:theoretical	0	25	14.3	100
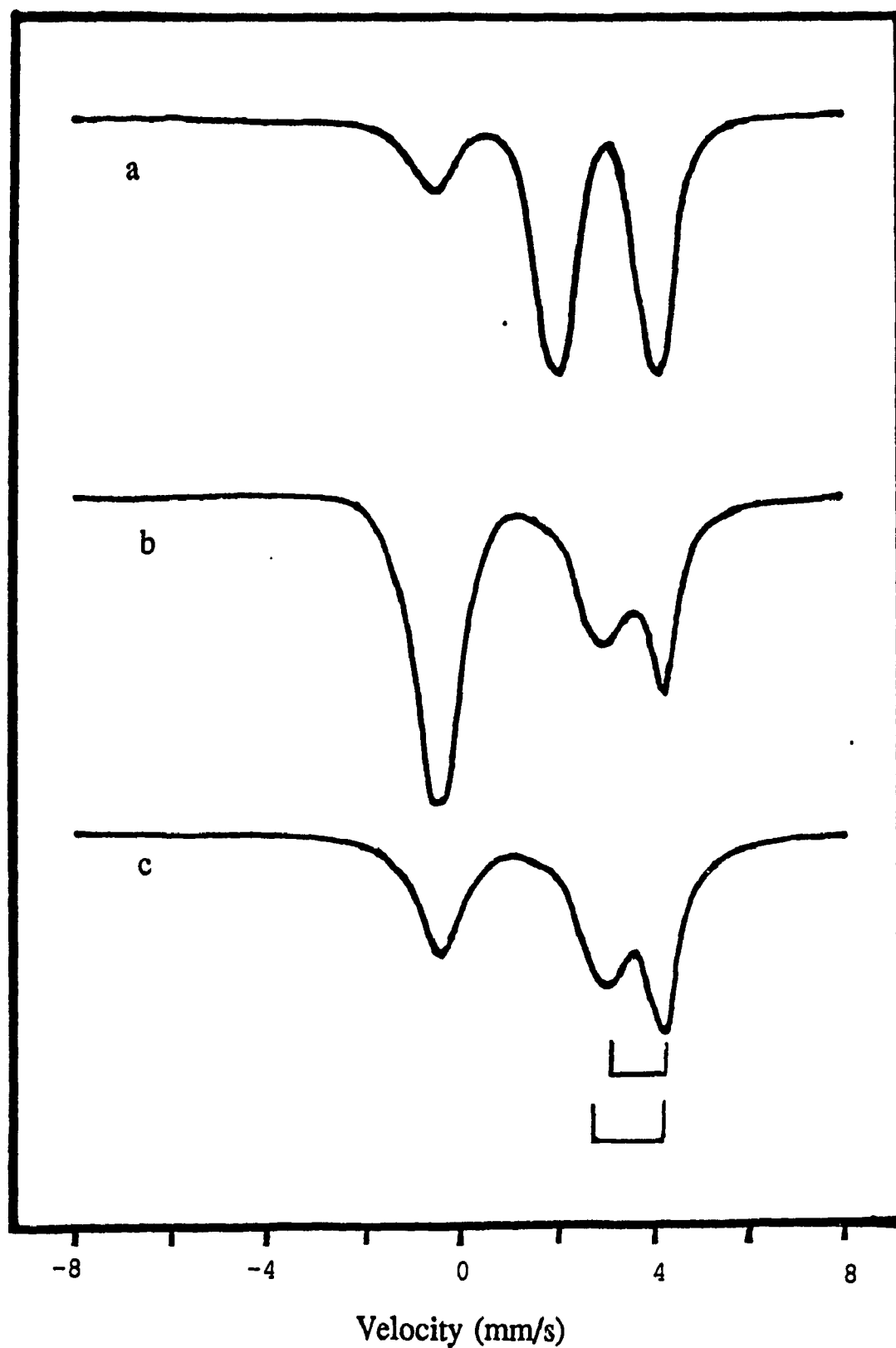
Fig. 5-14. Room Temperature Mössbauer Spectra of
        (a) Crystalline $CaSn_2F_6$ Before Washing;
        (b) the Residue after Evaporation of the Water Used for Washing $CaSn_2F_6$;
        (c) Sn_7F_{16} from literature

from Fig. 1 of [48], it is found that the reported g_{11} of 1.42 in [49] was calculated using line amplitudes rather than line intensities. The two methods yields the same result when the two lines have the same width, which is always the case when the doublet is unique, i.e. when it is the result of a non-spherical electric field gradient around one kind of tin only. The fact that one of the Sn(II) line is much broader for Sn_7F_{16} shows that the observed asymmetric doublet is the result of imperfect overlapping between at least two doublets, which have slightly different Mössbauer isomer shifts and quadrupole splittings. Quasi-perfect overlapping of the lines at higher velocity for each of the two doublets gives a narrow observed line with a high amplitude. Imperfect overlap between the two lines at lower velocity gives an observed broadened line with lower amplitude. An estimation of their intensity (amplitude multiplied by the linewidth) shows it is the same within experimental error (g_{11} = 1.02). Therefore, the apparent asymmetry is not a real Goldanskii-Karyagin effect since the observed doublet results from the partial overlap of at least two tin(II) quadrupole doublets, the asymmetry of which could add up or cancel each other or, they could simply be symmetric. Therefore, the present study has pointed out an error in the method of calculation of the Goldanskii-Karyagin parameter (g_{11}) in the literature [49].

Another parameter of interest in the spectra shown on Fig. 5-14 is the relative ratios of tin(II) and tin (IV). The parameter "% spectrum" in Table 5-9 refers to the % contribution of each tin species to the total Mössbauer spectrum, i.e.:

- for Sn(II):

$$\% spectrum = \frac{I[Sn(II)]}{I[Sn(IV)] + I[Sn(II)]} \times 100 \quad \ldots\ldots 5.19$$

- and for Sn(IV):

$$\% spectrum = \frac{I[Sn(IV)]}{I[Sn(IV)] + I[Sn(II)]} \times 100 \quad \ldots\ldots 5.20$$

with $I[Sn(II)]$ and $I[Sn(IV)]$ being the sum of the intensities of the two tin(II) lines, and the intensity of the tin(IV) line, respectively. It is well known that the contribution of each site to the total spectrum is usually not equal to its abundance, but, of course, it is proportional to it, and it must be corrected by its recoil-free fraction. Thus, the contribution of each tin site to the spectrum is proportional to the abundance of the site in the sample, multiplied by its recoil free fraction. The recoil-free fraction of tin(II) and tin(IV) in Sn_7F_{16} is known [49], and so is that of SnO_2 [51]. On the other hand, the recoil-free fraction of $CaSn_2F_6$ is not known. However, a rough estimate of the amount of tin(IV) impurity it contains can be obtained using the recoil-free fraction of α-SnF_2: $f_a(\alpha$-$SnF_2)=0.034$ [53], which is very close to the published value for Sn_7F_{16}: $f_a[Sn(II)$ in $Sn_7F_{16}] = 0.04$ [50]. Using the measured contribution of each site to the total spectrum and the recoil-free fraction for each site, the abundance of each kind of tin site in each sample has been calculated, and the results are compared to the theoretical values for the chemical formulae. The results are given in Table 5-9. It can be seen that the high recoil-free fraction of Sn(IV), especially SnO_2, makes its contribution to the Mössbauer spectrum much larger than its real abundance. For example, $CaSn_2F_6$ gives a tin(IV) line which contributes to 13% of the spectrum, although the sample contains no more than 1% SnO_2, which is already present in the α-SnF_2 used for the synthesis [36]. Using the literature data for Sn_7F_{16}, it can be found that the tin(IV) content calculated from the intensity of the tin(IV) line and its recoil-free fraction, to be equal to 11%, which compares well with the theoretical value of 14.3%. The case of the residue is more complex since the tin(IV) lines for Sn(IV) from Sn_7F_{16} and for SnO_2 are not resolved and the recoil-free fractions of the two tin(IV) species are not the same ($f_a[Sn(IV)] = 0.14$ for Sn_7F_{16} and 0.44 for SnO_2). However, using these two recoil-free fraction values and the stoichiometry of equation 5.17, we found a calculated amount of 22% Sn(IV) abundance in the sample, which is in excellent agreement with the theoretical value of 25%.

X-ray diffraction and Mössbauer spectroscopy show unambiguously that the residue of evaporation of the water used to wash $CaSn_2F_6$ contains crystalline Sn_7F_{16} and microcrystalline SnO_2, which are produced in the partial oxidation of SnF_2 by dissolved oxygen in aqueous solution, according to the reactions (eq. 5.15, 5.16 and 5.17). However, Table 5-8 shows that 19 lines are not accounted for by Sn_7F_{16}, and they

contrubute to 34.1% of the original total intensity diffracted. However the remaining intensity would decrease if the microcrystalline SnO_2 could be taken into account in this calculation. This cannot be done because the µPDSM software does not recognize its existence because of the very large peak-width due to the very small particle size (ca. 40 Å diameter). The first Bragg peak of the observed pattern is quite strong and unaccounted for by Sn_7F_{16} (Fig. 5-13(b)). It is clear from the Fig. 5-13 that this peak is broader than the first peak of $CaSn_2F_6$ which is located at an angle not far away. The average particle diameter, calculated from this unknown broadened peak, using Scherrer's method and Warren's correction, was found to be 361 Å. A search match was carried out in order to identify the Bragg peaks not accounted for by Sn_7F_{16}. Table 5-10 gives result of the search-match. No satisfactory match was found, since the best candidate, SnO, has two non-matched peaks and a similarity index of 50, which is much too low. In addition, SnO is black, therefore if it were mixed with white Sn_7F_{16} and SnO_2, the residue would be grey. Table 5-11 shows that the intensity of the two missing lines of SnO is far from being negligible, 17 and 6.3, with the strongest line of SnO being 21, which gives the two missing lines an intensity relative to 100 of 81 and 30. This shows unambiguously that SnO is not a satisfactory match, and it is further confirmed by the substraction of SnO, which removes only a negligible amount of intensity (34.1-27.9 = 6.2%) and still leaves 27.9% of the total intensity, and 15 lines unaccounted for (Table 5-12).

These results suggest that the residue of evaporation of the water used to wash $CaSn_2F_6$ contains crystalline Sn_7F_{16}, microcrystalline SnO_2 (average particle size ~40 Å) and at least another unidentified microcrystalline phase (average particle size = 361 Å).

5.6.2. Thermal Stability

The ionic conductivity measurements presented in Chapter 6 show that when crystalline $CaSn_2F_6$ is heated up to 200 °C, the curve of the conductivity ($log\sigma T$) versus temperature is reasonably reversible upon cooling. X-ray powder diffraction after the heating experiment shows no change of the powder diffraction pattern indicating that no irreversible transition took place. However, when the same sample is heated up

Table 5-10 Result of the Search-Match for the Residue Obtained by
Evaporation of the Water Used for Washing $CaSn_2F_6$,
after Substraction of the Powder Pattern of Sn_4F_{16}

```
JCPDS#——SI——ML/X——At%——Identity . . . ——————————
F1

F2
      Search Results [14 Entries]————————————
24-1342   50   5/2   21   Tin Oxide = SnO
21-0398   22   4/4   16   Ice = H2O
20-0241I  11   7/2   34  *Calcium Tin Oxide = Ca2SnO4
22-0623   10   3/1   18   Ice = H2O
36-1880O   8   3/1   26   C.I. Pigment Orange 52 =
36-1868O   8   3/4   62   C.I. Pigment Yellow 151 =
14-0140D   6   4/4   17   Tin Oxide Hydroxide / Hydroromarchite, syn = Sn3O
3-0188     6   4/3  9.9   Ammonia Cellulose =
36-1864O   5   2/1   48   C.I. Pigment Yellow 109 =
36-1867O   5   2/4   28   C.I. Pigment Yellow 154 =
4-0733I    1   2/2   21  *Calcium Hydroxide / Portlandite, syn = Ca(OH)2
15-0744*   0   4/1   29  *Tin Fluoride = SnF2
28-1389    0*  6/0   53   Tin Fluoride = Sn7F16
30-1374O  <0   2/1  9.9   Tin Oxide Fluoride = Sn4O2F4

      Ierr:50,150   derr:4.0   Bground:6      dmax/min:7.358/1.540
      Test Results [ 0 Entries]—————————————————
Plot Shift+F8——Hold F1 F2——Copy Ins——Test F7——Match F8——Subtract F9——Exit Esc
```

100

Table 5-11 Matching Table of SnO with the Residue, After Prior Removal of Sn_7F_{16}

```
JCPDS#      SI      ML/X      At%      Identity . . .
24-1342     50      5/2       21       Tin Oxide = SnO
            Ierr:50,150    derr:4.0    Bground:6       dmax/min:7.358/1.540
```
* Obscured Lines

24-1342 @ 21.1%		User Pattern		Resid	
d	I	d	I	derr	I
2.90	17	2.9130	8	+1.5	None
		2.8440	29	-6.7	
2.78	17	Missing			
2.63	21	2.6170	21	-1.9	None
2.24	2.1	2.2370	9	-0.6	7
2.12	2.1	Below Background			
1.95	6.3	Missing			
1.80	2.1	1.8160	11	+4.9	
1.75	4.2	Below Background			
1.66	11	Previously Removed			
1.572	11	1.6600	7	0.0	None
		1.5740	8	+0.8	None

24-1342 @ 21.1%		User Pattern		Resid	
d	I	d	I	derr	I

```
Plot Shift+F8                                        Return to Tables Esc
```

Table 5-12 Result of the Substraction of the Powder Pattern of SnO from the Residue, after Prior Substraction of Sn_7F_{16}

```
 JCPDS#      SI    ML/X   At%   Identity . . .
24-1342      50    5/2     21   Tin Oxide = SnO
          Ierr:50,150    derr:4.0  Bground:6      dmax/min:7.358/1.540
Substraction

Lines removed: 2.9130 2.6170 1.6600 1.5740

Lines reduced (d=Inew): 2.2370=7

 4 lines removed.   1 lines reduced.   15 lines left.
27.9% of the original total intensity remains.
Use MODIFY to make manual adjustments.
```

Press Esc when ready to proceed

102

to 250 °C, a break in the conductivity curve versus temperature is observed at ca. 220 °C which indicates a drastic decrease of activation energy. Upon cooling, the high temperature portion of the curve extends below 220 °C, down to ca. 180 °C, at which point the conductivity starts to decrease rapidly. However, down to ambient temperature, the activation energy is much higher than that of the initial $CaSn_2F_6$ at the same temperature (see Fig. 6-6 in Chapter 6, section 6.1.2) and is similar to that of SnF_2 [54]. X-ray powder diffraction patterns of the sample after cooling to room temperature (Fig. 5-15) shows that a complete structural change has taken place and only crystalline α-SnF_2 is detectable [44]. It can be hypothesised that at high temperature, decomposition of the sample to SnF_2 and CaF_2 took place to give liquid SnF_2 and solid CaF_2:

$$CaSn_2F_{6\,(s)} \longrightarrow 2SnF_{2\,(l)} + CaF_{2\,(s)} \qquad 5.21$$

Then, upon cooling, SnF_2 undergoes the following changes, which have been well characterized [44].

$$SnF_{2\,(l)} \xrightarrow{\sim 180^\circ C} \gamma\text{-}SnF_2 \underset{\longleftarrow}{\overset{66^\circ C}{\rightleftharpoons}} \beta\text{-}SnF_2$$

110 °C < T < 66 °C \qquad T < 66 °C \qquad\qquad 5.22

$$\alpha\text{-}SnF_2$$

The ionic conductivity of $CaSn_2F_6$ is much lower than that of α-SnF_2. However, because of its high activation energy, it reaches the conductivity of liquid SnF_2 at the decomposition point. Although the melting point of SnF_2 is 215 °C, on cooling, it can remain liquid (supercooled state) down to ca. 180 °C if undisturbed (no thermal or mechanical shock) [44]. At ca. 180 °C, the liquid solidifies at once, to give γ-SnF_2. This results in a rapid decrease in conductivity. The γ-phase is metastable below ca. 110 °C (there is a hysteresis to the $\alpha \rightarrow \gamma$ transition, the temperature of which is not well defined because of its grain size dependence) and can transform according to two pathways:

(i) 110 °C < T < 66 °C: irreversible transformation to stable α-SnF_2 ;

(ii) at 66 °C: second order phase transition to metastable β-SnF_2, which transforms spontaneously, irreversibly, and in an uncontrollable way, to stable α-SnF_2.

Therefore, after slow cooling, which gives the system enough time and enough thermal energy to relax to
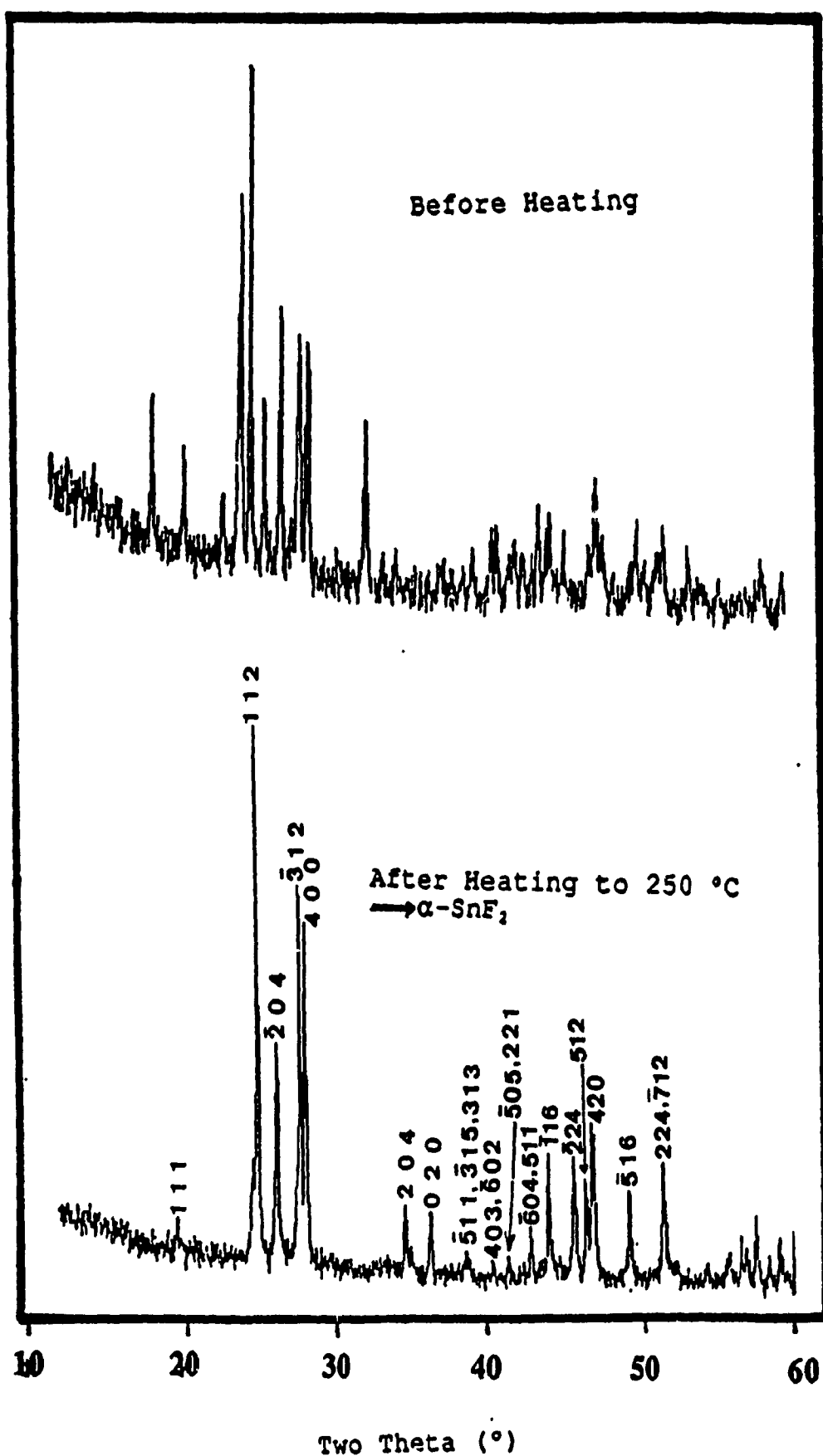
Fig. 5-15 Effect of Heating on Crystalline CaSn$_2$F$_6$ (n=0.05)

thermodynamic stability, α-SnF$_2$ is always the end phase. Since the samples were cooled slowly in the conductivity apparatus, X-ray diffraction after cooling shows only α-SnF$_2$. In order to stabilize temporarily β-SnF$_2$ at room temperature, rapid quenching from T > 110 °C would be required [38, 44, 55, 56, 57]. γ-SnF$_2$ cannot be stabilized below 66 °C because of the $\beta \to \gamma$ transition is of second order, and therefore cannot have any hysteresis, by definition.

The decomposition according to reaction 5.21 also produces CaF$_2$. Since no Bragg peak for CaF$_2$ is observed, it can be concluded that it is microcrystalline or amorphous or other reaction, possibly involving copper, have occurred.

The fact that CaSn$_2$F$_6$ is thermodynamically unstable at high temperature could have been predicted for two reasons:

(i) All earliers attempt to carry out reactions between CaF$_2$ and SnF$_2$ at high temperature failed, giving only the starting materials as end products [13, 15];

(ii) Bulk density measurements show that the density of CaSn$_2$F$_6$ falls exactly on the line joining the densities of CaF$_2$ and SnF$_2$ versus substitution rate (Fig. 5-11), i.e.

$$\rho_{[CaSn_2F_6]} = \frac{2\rho_{[SnF_2]} + \rho_{[CaF_2]}}{3} \quad \ldots \ldots 5.23$$

the density of CaSn$_2$F$_6$ is the average weighed densities of CaF$_2$ and α-SnF$_2$. In other words, there is no decrease of volume and no improved packing, due to the formation of CaSn$_2$F$_6$, relative to the starting materials. This is an indication that CaSn$_2$F$_6$ is not thermodynamically favoured by its lattice energy. However, since its density is not lower than that of the starting materials, it is also not thermodynamically unfavoured at room temperature. It results that heating, which supplies the energy required for ion diffusion to carry out a solid state reaction does not result in this product which is not energetically favoured. However, when all required ions are mixed in aqueous solution within an appropriate range of stoichiometries, the compound may be formed because it is energetically favoured at low temperature. The result is a metastable compound, which is trapped in a non-stable (but not really unstable) state at room temperature. However, heating affords sufficient energy to destabilize this fragile ionic arrangement.

105

Therefore, metastable $CaSn_2F_6$ cannot be prepared from reactions at high temperature. The lack of stability of the $CaSn_2F_6$ structure also explains its sensitivity to the reaction parameters: slight changes in the conditions (stoichiometry, stirring) produces mixtures of phases. It also explains its poor stability toward aqueous solutions. The microcrystalline $Ca_{1-x}Sn_xF_2$ fluorite-type phase showed no change of conductivity behaviour upon heating up to 220 °C, and its thermal stability was not investigated further. The electrochemical properties of crystalline $CaSn_2F_6$ and microcrystalline $Ca_{1-x}Sn_xF_2$ will be discussed in the following chapter.

CHAPTER 6.

RESULTS AND DISCUSSION (2)

--- Electrochemical Measurements on MF_2-SnF_2 Systems

.

In this chapter, the electrochemical measurements on material obtained in the CaF_2-SnF_2 system are

compared with those of known compounds in other MF_2-SnF_2 systems (M = Pb, Ba). To carry this out the

latter compounds were prepared either by solution or solid state synthesis and characterised under exactly

the same conditions as the CaF_2-SnF_2. These measurements lead to a description of the conduction and

thermodynamic characteristics.

6.1. Conductivity Measurements

As can be seen from Fig. 6-1, the resistance decreases sharply as the pressure increases and becomes

a constant after about 3000 p.s.i. Similarly, Fig. 6-2 shows that the temperature reaches a constant after

about 30 min following temperature selection. All measurements described below were therefore taken with

an applied pressure > 3000 p.s.i. and 30 mins after selecting the temperature.

6.1.1. Ionic Conductivity

In agreement with other workers [54, 58], conductivity measurements show that the SnF_2 undergoes a

phase transition at about 78 °C which, from X-ray powder diffraction studies [59], has been shown to be

associated with a change from monoclinic (α-SnF_2) to tetragonal (γ-SnF_2) symmetry. As can be seen from

Fig. 6-3, the activation energy for electronic conduction does not change during this transition, suggesting

that it is dependent on the electronic configuration of the Sn^{2+} lattice and not primarily on the crystal

structure. In contrast, curve-fitting of the temperature dependence of the total conductivity ($\sigma_i + \sigma_e$)

suggests that there is a decrease in activation energy for fluoride ion conduction from 0.4 eV to 0.1 eV.

This implies that the phase transition is associated with the disordering of the fluoride ion sublattice. As
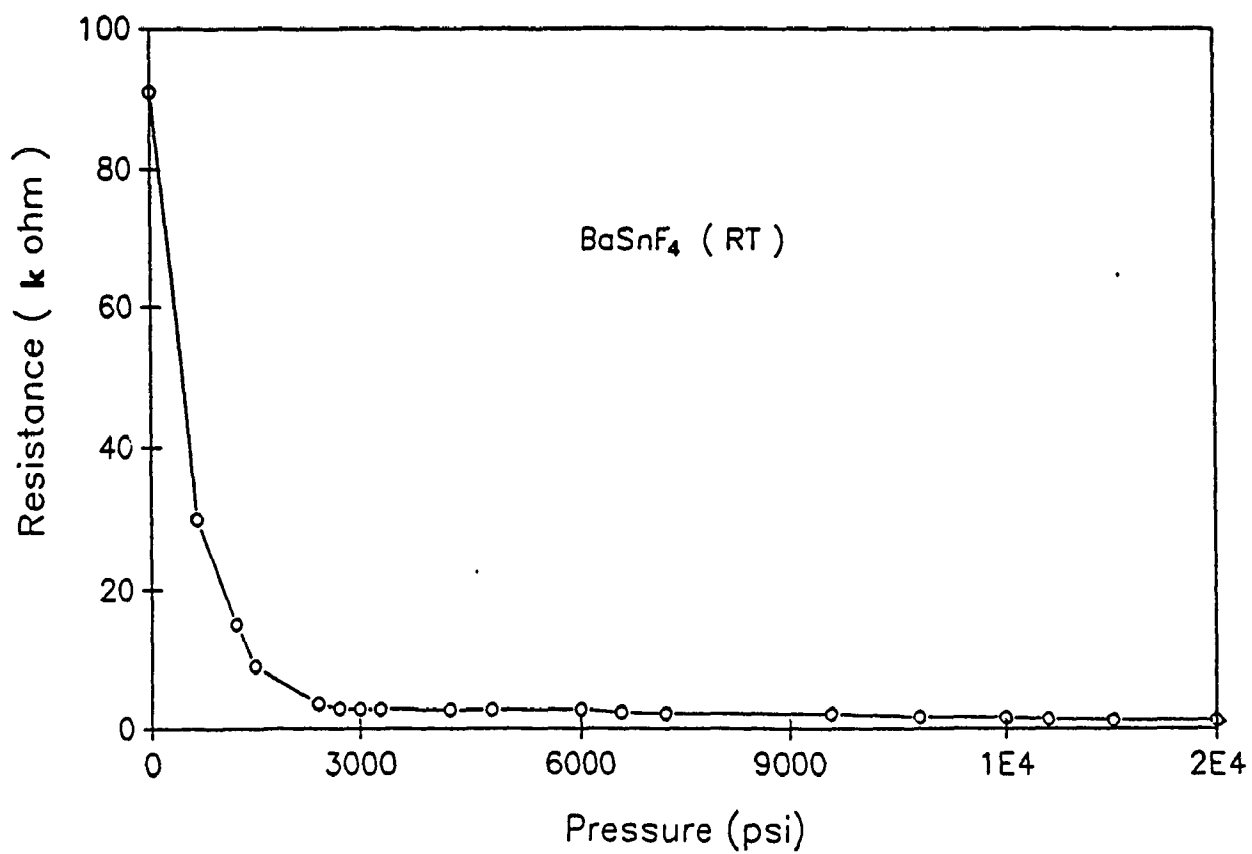
Fig. 6-1 Pressure Dependence

Fig. 6-2 Time Dependence

109
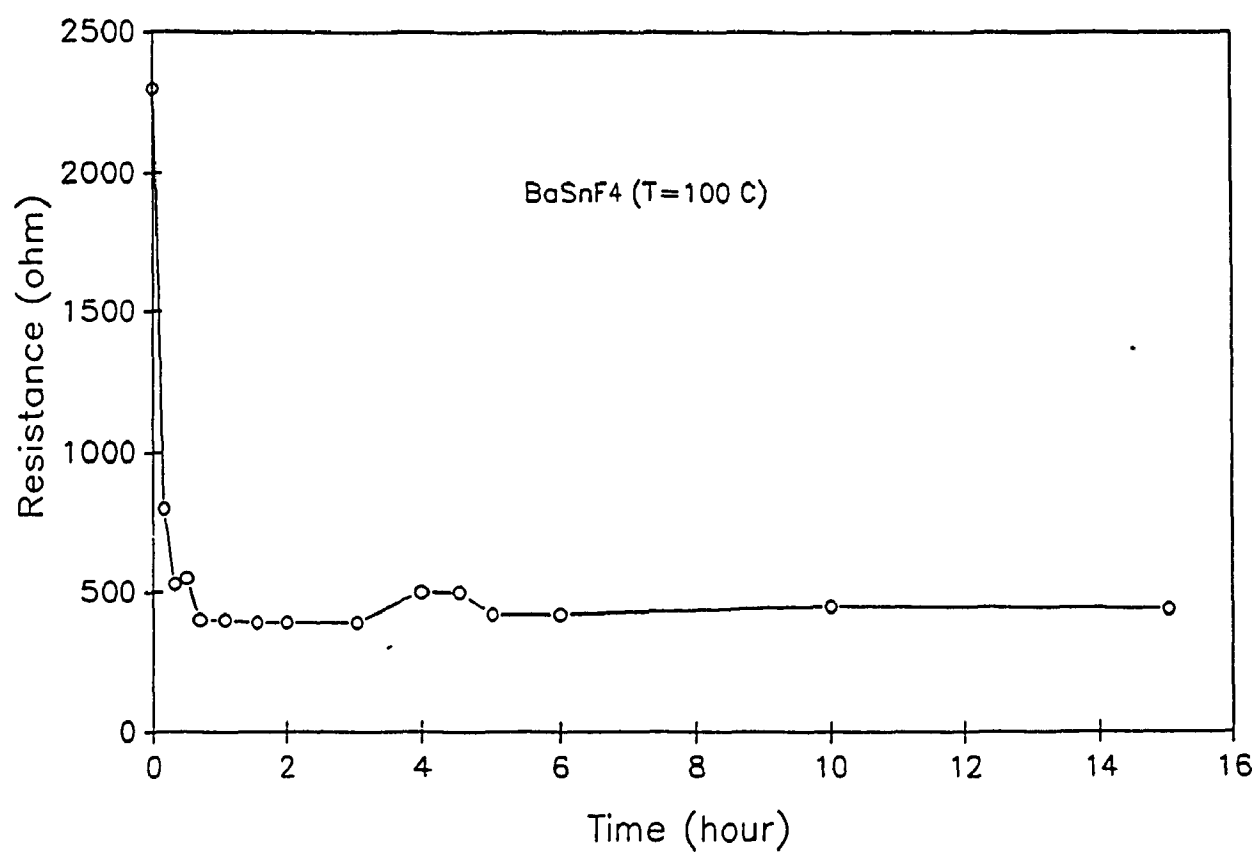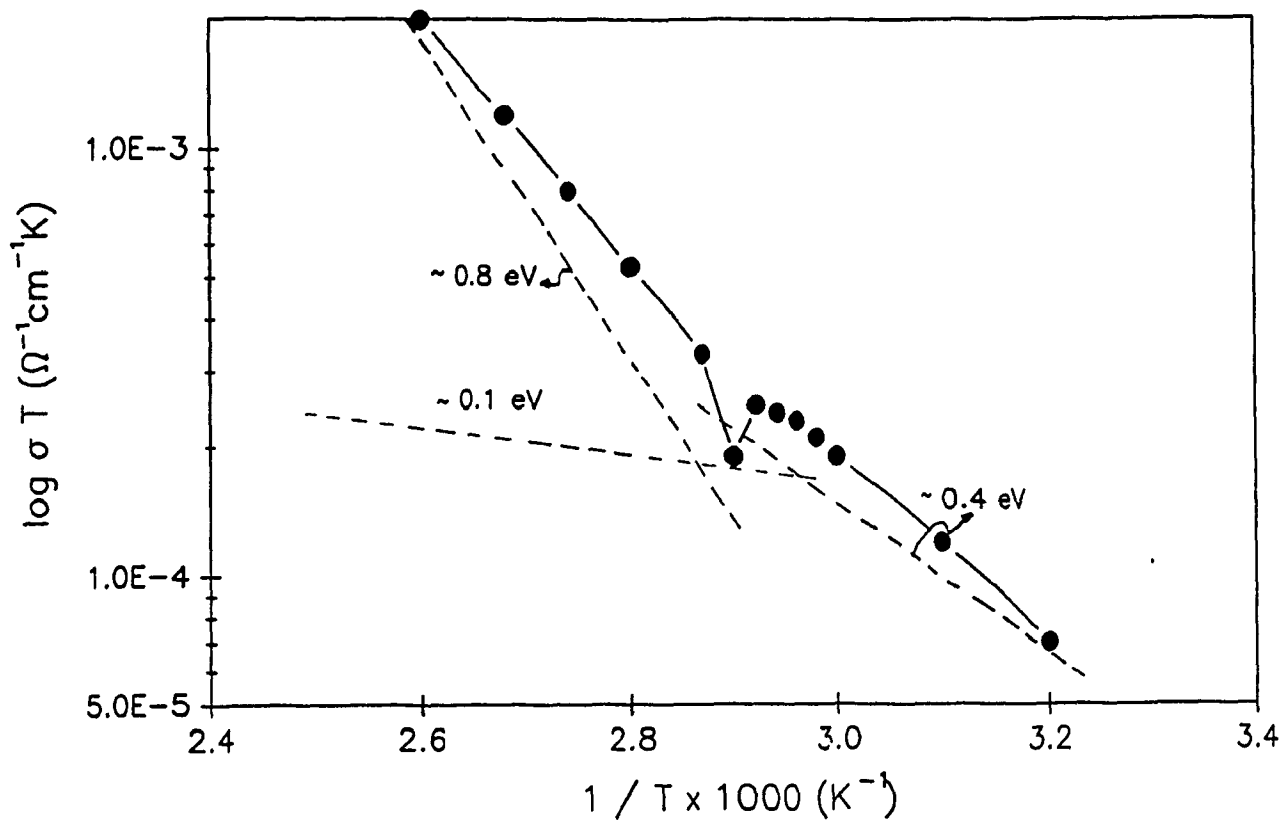
Fig. 6-3 Ionic Conductivity of SnF₂

(For clarity, high and low temperature points have been omitted)

will be shown later, this has important conclusions in the discussion of the $MSnF_4$ and the CaF_2-SnF_2 systems.

Table 6-1 Ionic and Electronic Conductivity

and Activation Energies (25°C)

Compound	Ionic		Electronic	
	$\sigma_i(cm^2/s)$	$E_a(eV)$	$\sigma_e(cm^2/s)$	$E_a(eV)$
α-SnF_2	1×10^{-7}	0.40	1.5×10^{-9}	0.71
γ-SnF_2*	3×10^{-7}	~0.1	1.0×10^{-9}	~0.8
$PbSnF_4$	8×10^{-6}	0.39	1.2×10^{-8}	0.54
$BaSnF_4$	5×10^{-6}	0.32	$< 5 \times 10^{-8}$	-
SnF_2-CaF_2 (n=0.67)	1×10^{-8}	0.64	4.5×10^{-10}	0.62
SnF_2-CaF_2 (n=0.10)	1×10^{-9}	0.86	1×10^{-9}	0.80
CaF_2[58]	$\sim1 \times 10^{-13}$	~1.3	-	-

*: Ionic conductivity results are obtained by extrapolation

Again in agreement with literature values [15, 59], both $PbSnF_4$ and $BaSnF_4$ exhibit high ionic conductivity and low activation energies (Fig.6-4 and Table 6-1). These measurements suggest little evidence of a phase transition in these systems although a small change (ΔE =0.02 eV) occurs in the $BaSnF_4$ at a temperature of 125 °C [59]. These results indicate that the ionic conduction mechanism is strongly influenced by the presence of Pb^{2+} and Ba^{2+} ions. As PbF_2 is also a good ionic conductor (but a different structure), it would be tempting to suggest that conduction mechanism is similar to that of PbF_2 rather than SnF_2. This remains to be proven.

111
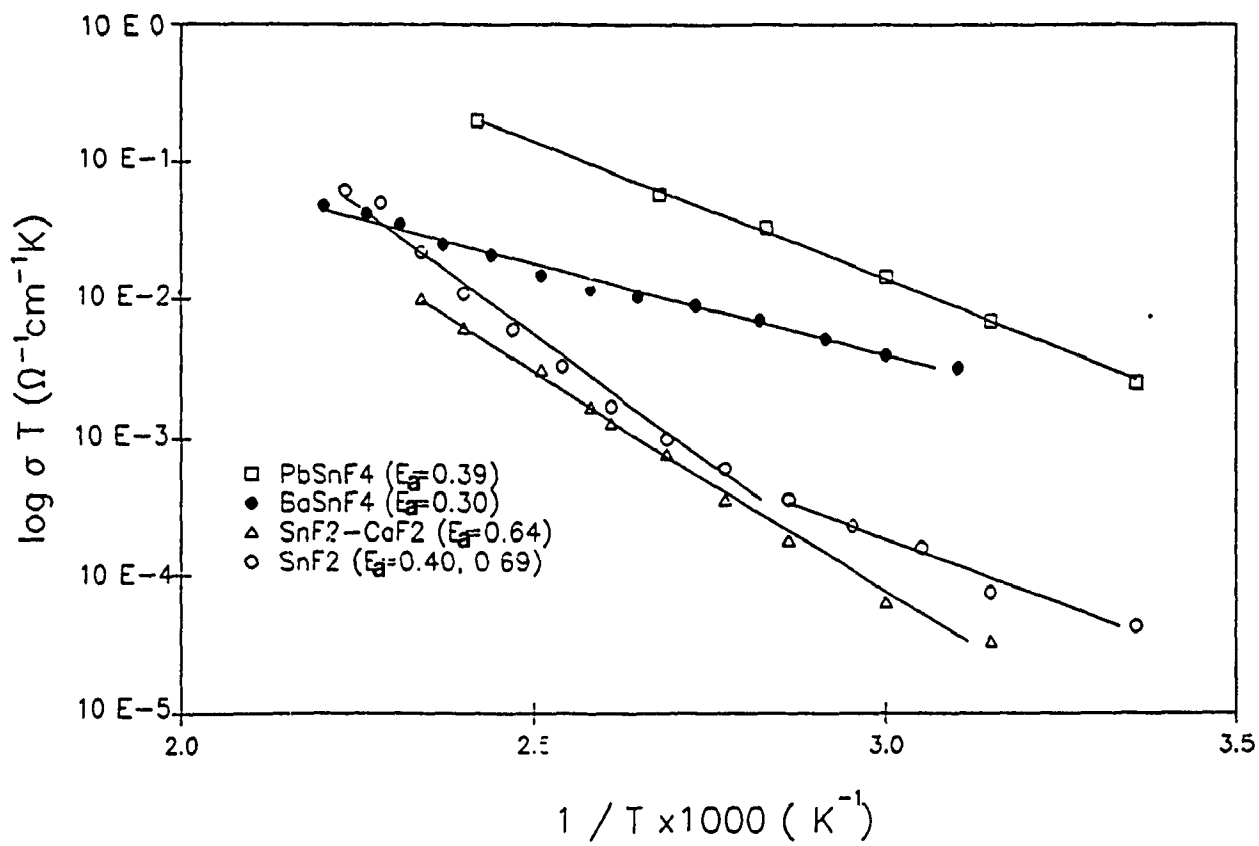
Fig. 6-4 Ionic Conductivity of MSnF4

In contrast to the above, the conductivity of the CaF_2-SnF2 system (Fig. 6-5) depends on the preparation conditions and, in particular, the reaction mole fraction, n. At low n values where a crystalline phase (Chapter 5) is obtained, the conductivity exhibits a behaviour which is very similar to SnF_2 again suggesting that the crystalline phase is tin-rich. In contrast, at high n values where the microcrystalline phase (CaF_2 structure) is obtained, a higher ionic conductivity is obtained (Table 6-1). Similarly, at intermediate values, the conductivity of the mixed products depends on the volume fractions of the crystalline and micro-crystalline phases. Although the results are consistent with Effective Medium Percolation Theory (EMPT) [60], it is impossible to analyze the system fully in these terms at this time. The main reasons for this include

1) a lack of information about the chemical composition;

2) the poor correlation of the chemical properties; and, in particular;

3) the fact that the crystal structure of the crystalline phase which has not been indexed (Chapter 5).

Conductivity measurements in this system also suggest that the products obtained at various n values decompose at approximately 220 °C (Fig. 6-6), well below the melting point of (260 °C - 290 °C). This is witnessed by a change in activation energy for the conductivity and also the appearance of a green coloration. Although the decomposition product has not been identified, tentatively it has been suggested that a component is α-SnF_2 since it has the same X-ray powder diffraction pattern (Fig. 5-15 in section 5.6.2.). The greenish coloration suggests a reaction of the compound with the copper electrodes as suggested in chapter 5.

6.1.2. Electronic Conductivity

The results of an approximate measurement of the electronic conductivity are shown in Fig. 6-8. The electronic conductivity of the $MSnF_4$ compounds obtained by the more accurate polarization method are compared in Fig. 6-7. These results show that the $MSnF_4$ materials are good ion conductors and poor electronic conductors. This can be also demonstrated by the ionic and electron conductivities listed in Table 6-1. From the ionic and electronic conductivity measurements described above, the ionic transport number

113
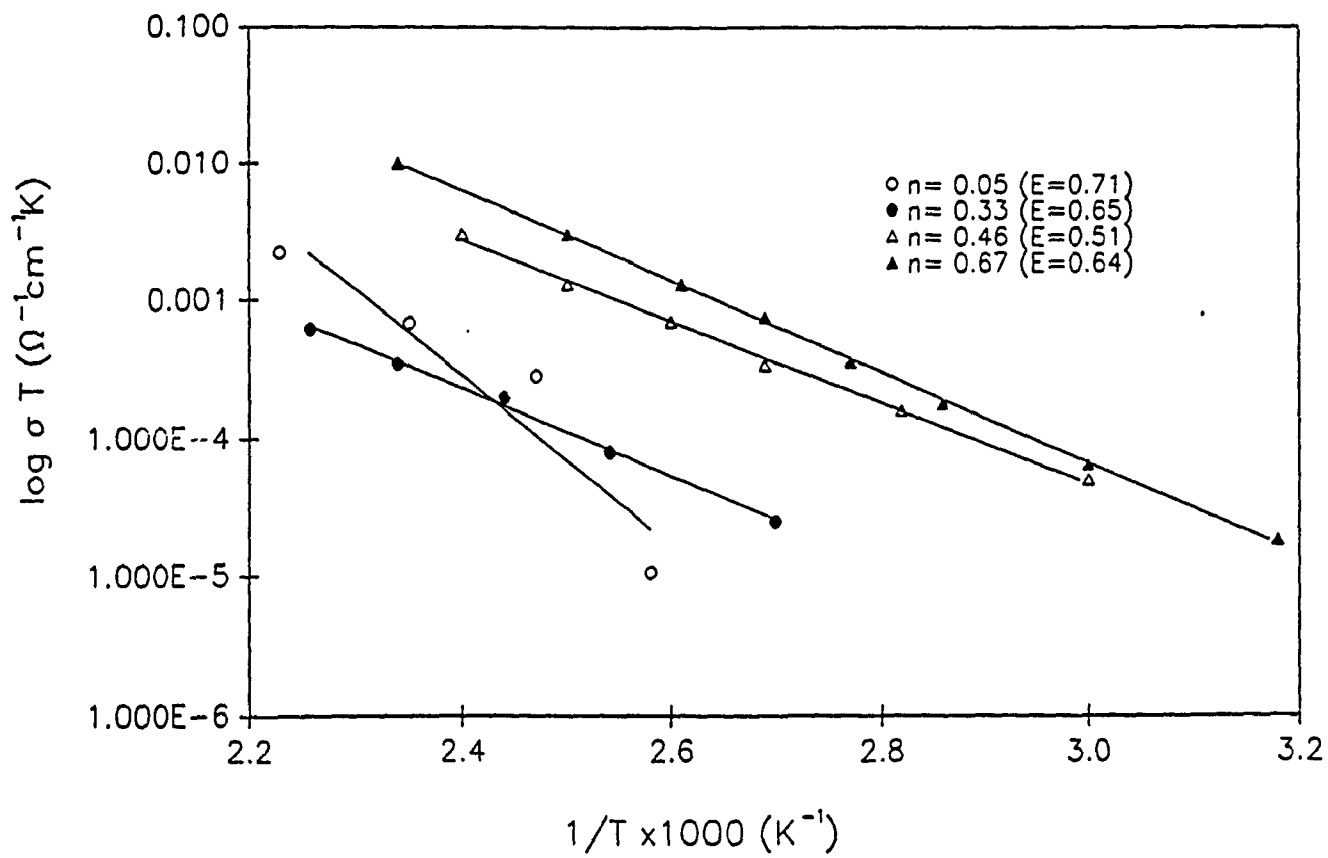
Fig.6−5. Ionic Conductivity of SnF2−CaF2 System

114
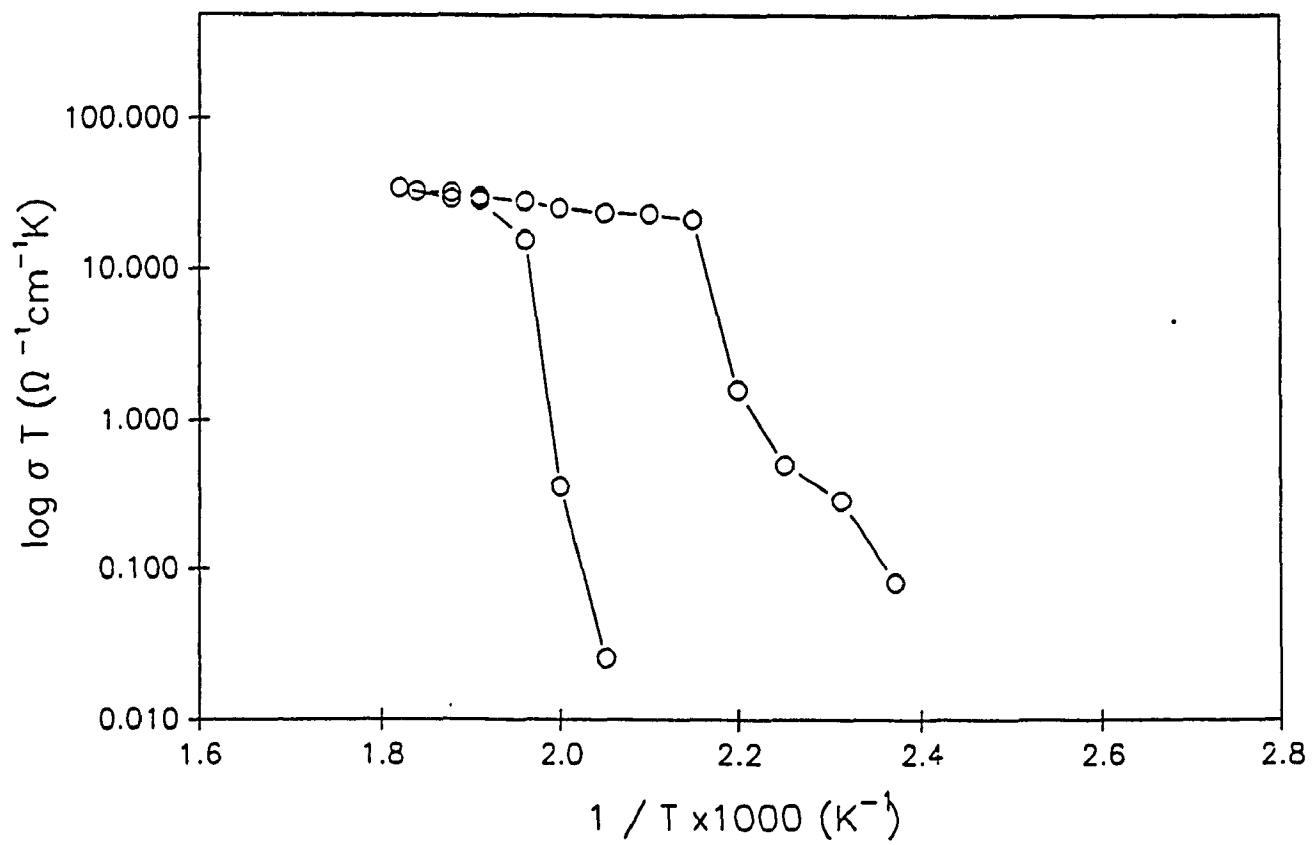
Fig. 6-6 Decomposition of SnF$_2$-CaF$_2$ System

can be calculated (Table 6-2).

At low n values, the CaF_2-SnF_2 system has a very low transport number which is more like γ-SnF_2 and it is a very poor ionic conductor. $BaSnF_4$ has about the same level of electronic conductivity as CaF_2-SnF_2 system at higher n values, but it has 100 times higher ionic conductivity than CaF_2-SnF_2 system.

Table 6-2. Ion Transport Number at Room Temperature

Compound	Transport Number
α-SnF_2	0.99
γ-SnF_2(160°C)	0.71
$PbSnF_4$	0.99
$BaSnF_4$[53]	0.99
CaF_2-SnF_2(n=0.10)	0.50
CaF_2-SnF_2(n=0.67)	0.96

Figure 6-7 shows that the $PbSnF_4$ has high electronic conductivity and a low activation energy. Qualitatively, it is felt that this may be due to the fact that, in $PbSnF_4$ the Pb(2+) and Sn(2+) can easily change their oxidation states, i.e.

$$Pb^{2+} - 2e \rightleftharpoons Pb^{4+}$$

$$Sn^{2+} - 2e \rightleftharpoons Sn^{4+}$$
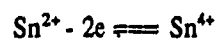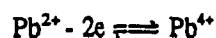
These processes may leave electron holes and result in high electronic conductivity. The M(4+) will change back to they original state M(2+). This is a very fast process, and it is too fast to see the change of oxidation states. Note that Ca and Ba have no other oxidation states and cannot therefore participate in such a process.

116
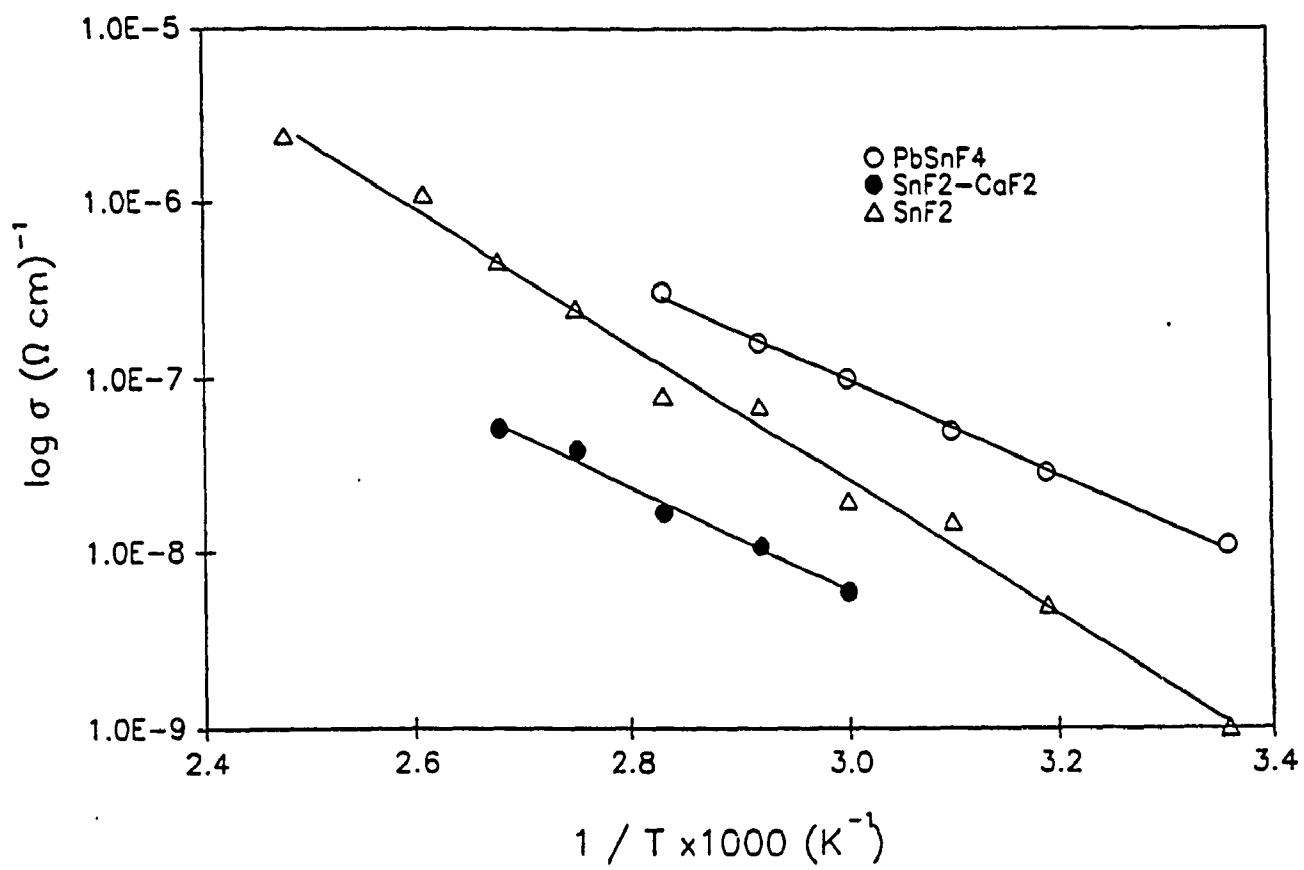
Fig. 6-7. Electronic Conductivity by Polarization Cell Method
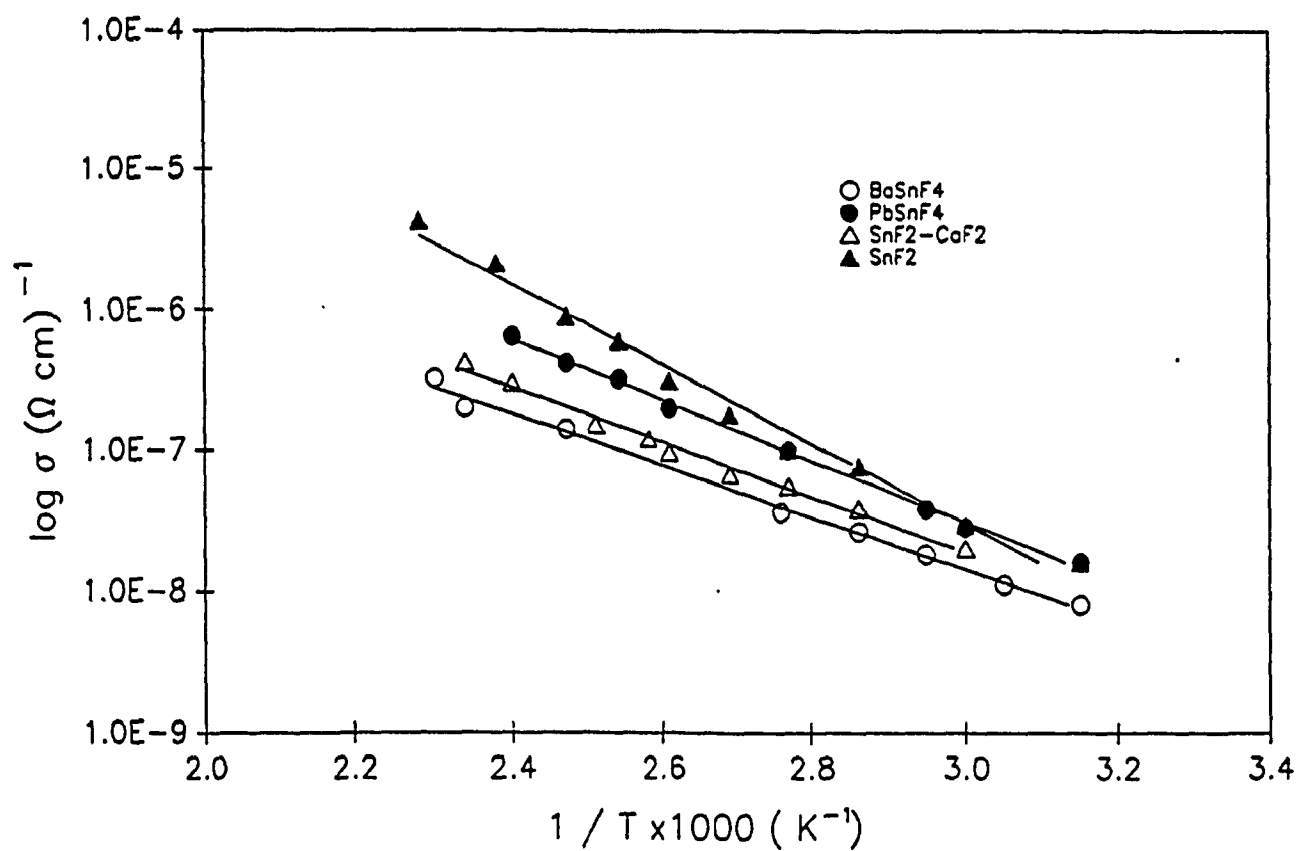
Fig. 6-8. Electronic Conductivity by Approximate Method

6.2. The Current-Potential Behaviour

The current-potential behaviour of $BaSnF_4$ electrolytes between two non-blocking electrodes was measured as a function of temperature and typical I-V curves are shown in Fig. 6-9. These curves were used to calculate the Tafel constant and exchange current density (Table 6.3). In contrast, in the CaF_2-SnF_2 system, at temperature below 80°C, the electrolyte resistance was too high to allow further analysis. Between 80 °C and 110 °C, however, typical Tafel behaviour - as illustrated by linear log I-V curves (Fig. 6-10) - was observed allowing calculation of the Tafel constant, b, and the exchange current density, i_o (see Chapter 4). The values obtained are listed in Table 6-4. To explain this behaviour, it is necessary to have two electrode reactions occurring - one anodic and one cathodic - to allow charge transfer across the electrode interfaces. As it seems unlikely that any reactions involving the oxidation / reduction of fluoride ions can occur due to its high electronegativity, the observed electrode reactions must involve a change in oxidation state of the metal ion(s) (either M^{2+} or Sn^{2+}).

6.2.1. The Anodic Reaction

As no other stable oxidation states of barium or calcium are known to exist, the main anodic reaction must therefore be due the oxidation of tin:

$$Sn \longrightarrow Sn^{2+} + 2e \qquad (6.1)$$

$$Sn^{2+} \longrightarrow Sn^{4+} + 2e \qquad (6.2)$$
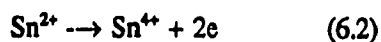
Note, however, that these both represent an overall 2-electron step and does not preclude the participation of other species (for example included O_2) in the exact mechanism to form species such as SnO_2. A further possibility is the oxidation of O_2 or H_2O encapsulated in the cell during loading. It is very difficult to eliminate this possibility completely. However, the available evidence suggests that, as no dependence on the atmospheric conditions or sample conditions was observed, these mechanisms seem unlikely.

119

Table 6-3. Exchange Current Density and

Tafel Slope of the $BaSnF_4$

T($^\circ$C)	i_0(A/cm^2)	b(mV/decade)
50	1×10^{-6}	90
60	2×10^{-6}	85
70	4×10^{-6}	75
80	5×10^{-6}	60

i_0: Exchange current density;

b: Anodic and cathodic Tafel slope.

Table 6-4. Exchange Current Density and

Tafel Slope of the SnF_2-CaF_2 System

Compound	T ($^\circ$C)	i_0(A/cm^2)	b(mV/decade)
SnF_2-CaF_2 (n=0.67)	80	4.8×10^{-7}	73
	95	1.2×10^{-6}	60
	110	1.0×10^{-6}	35

i_0: Exchange current density;

b: Anodic and cathodic Tafel slope.

(A)

(B)
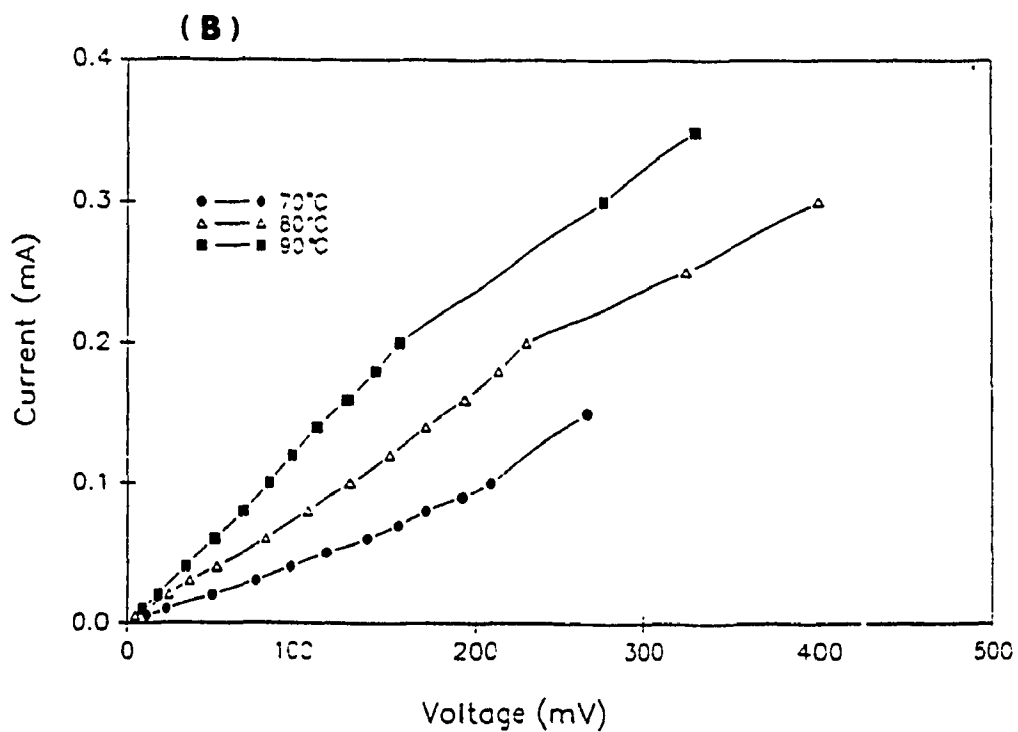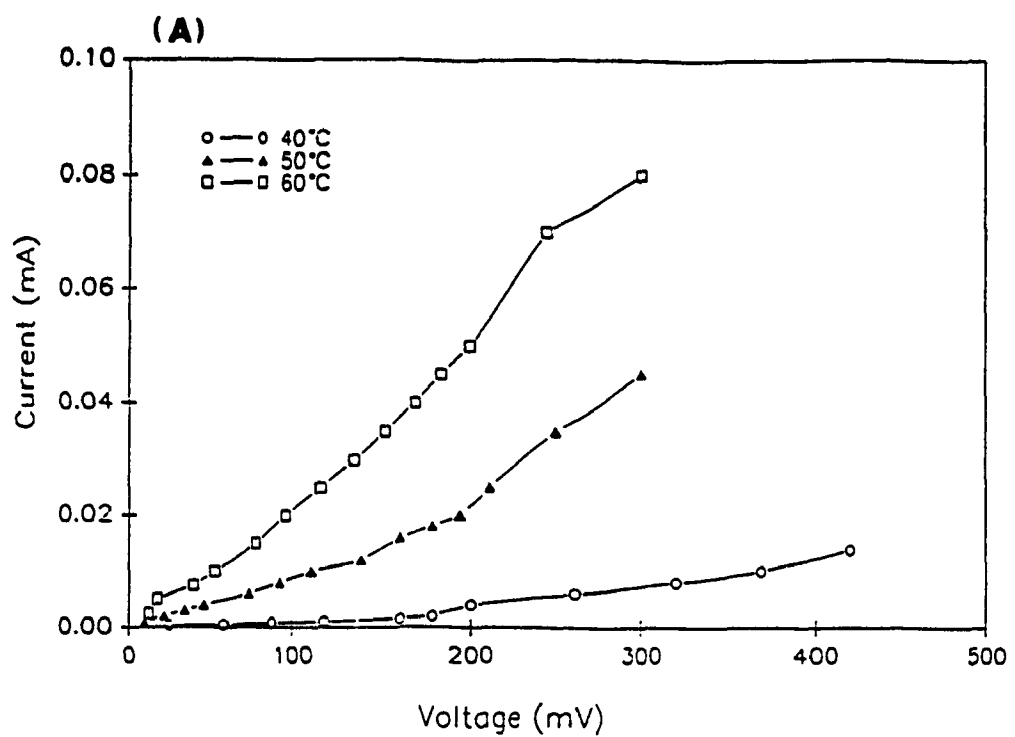
Fig. 6-9   I-V Curve of BaSnF₄

121
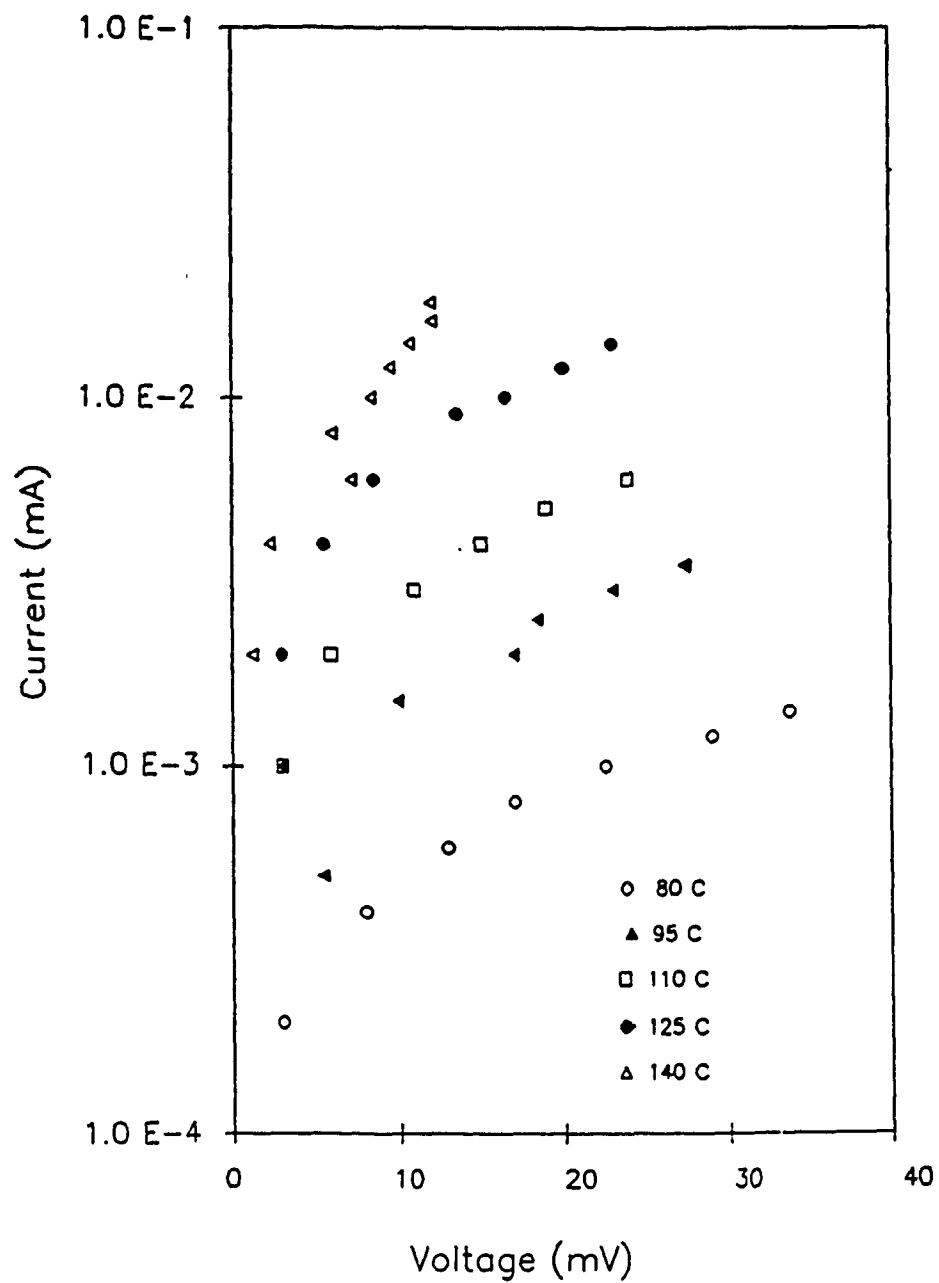
Fig. 6-10 log i vs E of $Ca_{1-x}Sn_xF_2$

122

6.2.2. The Cathodic Reaction

In contrast to the above, three cathodic reactions can be postulated. The first two involve the electrodeposition of the pure metals

$$M^{2+} + 2e \longrightarrow M \qquad (6.3)$$

and
$$Sn^{2+} + 2e \longrightarrow Sn \qquad (6.4)$$

Considering the difference in electronegativity of the two metals, it is felt that the first of these reactions (equation 6.3) can be precluded. However, alloy formation, caused possibly by simultaneous deposition of both metals (equation 6.5), cannot be discounted

$$M^{2+} + Sn^{2+} + 4e \longrightarrow (MSn)_y \qquad (6.5)$$
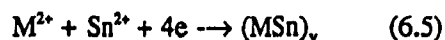
This would certainly be favoured at high n values in the CaF_2-SnF_2 where it is believed a calcium-rich phase is formed (chapter 5 and section 6.1). As will be shown, the experimental data is not available to distinguish between these possibilities. Again the evolution of hydrogen from any water present cannot be eliminated. However it would be expected that the high reactivity of the products of such a reaction would lead to sample degradation which was not observed in any of these experiments. This suggests that these reactions involving H_2O do not in fact occur to any great extent.

6.2.3. Kinetics

Certain similarities exist between the behaviour of $BaSnF_4$ and CaF_2-SnF_2 electrolytes. In the CaF_2-SnF_2 system, the Tafel constants at 80 °C and 90 °C indicate that the rate is limited by an irreversible step (i_d>>i_0) occurring at one of the electrodes, at 110 °C, the Tafel constant suggests that the two-electron transfer is reversible, i.e. the concentration of the electroactive species becomes a predominant factor at high temperature. Similarly, for the $BaSnF_4$ electrolyte, where a larger temperature range is available for analysis, a gradual transition from exponential kinetics to apparently diffusion limited behaviour is observed. These observations imply that

1) A second mobile species is being generated in the interfacial region to allow the concentration of the electroactive species to vary with potential and yet preserve electroneutrality;

2) The 'diffusion-limited' current, i_d, must be proportional to the diffusion coefficient, D, of this second species according to a relation of the form

$$i_d = \frac{D_s C_s}{\delta}$$

where c_s is the interfacial concentration of the slow species and δ is the diffusion layer thickness;

3) The rate of diffusion must increase with potential to allow the linear increase observed in i_d (Fig. 6-11).

Perusal of the possible electrode reactions (6.1 - 6.5) leads to the conclusion that only the oxidation of Sn^{2+} to Sn^{4+} would provide the second mobile species necessary to measure the effects of diffusion. Thus the overall reaction can therefore be viewed as shown schematically in Fig. 6-12. At the anode, Sn^{2+} is oxidized to Sn^{4+} which requires that the local concentration of fluoride ion increases to form a 'compound' of the form SnF_4 or $MSnF_6$. This requires that the cathodic reaction is the deposition of the metal to allow 2 'free' fluoride ions to migrate to the anode under the influence of the electric field, as the fluoride ion is known to have relatively high mobility in these compounds, the second mobile species for the observation of diffusion limited kinetics would be Sn^{4+}. Note that this does not require the Sn^{4+} ion to move physically, rather two electrons can be transferred from adjacent Sn^{2+} ions resulting in an overall transport of an Sn^{4+} ion.

To confirm this hypothesis it is necessary that the diffusion rate be proportional to the electron mobility and thus can be compared to the data discussed in Section 6.1.2. Thus i_d (defined as the point at which diffusion limits are observed (Fig. 6-11)) should have the same activation energy as that for electronic conduction as measured independently by the Hebb-Wagner polarisation method. Experimentally it is found that this value (0.6 eV) is much closer to that of electronic (0.8 eV) rather than ionic (0.3 eV) conductivity. If it is remembered that other contributions such as the grain boundaries have been neglected and the experimental determination of i_d is difficult, these values tend to confirm the interpretation. In contrast to solid electrolytes, the current in the diffusion-limited region will not be constant but rather vary linearly with potential (Fig. 6-11). This is because the separation between charges (F^- and Sn^{4+} in this case) will increase as the voltage across the electrolyte is increased. Thus the resistance defined by the slope of this section curve should reflect the resistance to motion of the slower species. Over the small temperature range available, the measured data ($E_a = 0.6$) tends to confirm this conclusion. Although qualitatively correct because similar observations have been observed in other solid electrolyte systems [61, 62], a new theory is being formulated mathematically to better account for this behaviour and thus further prove our

124
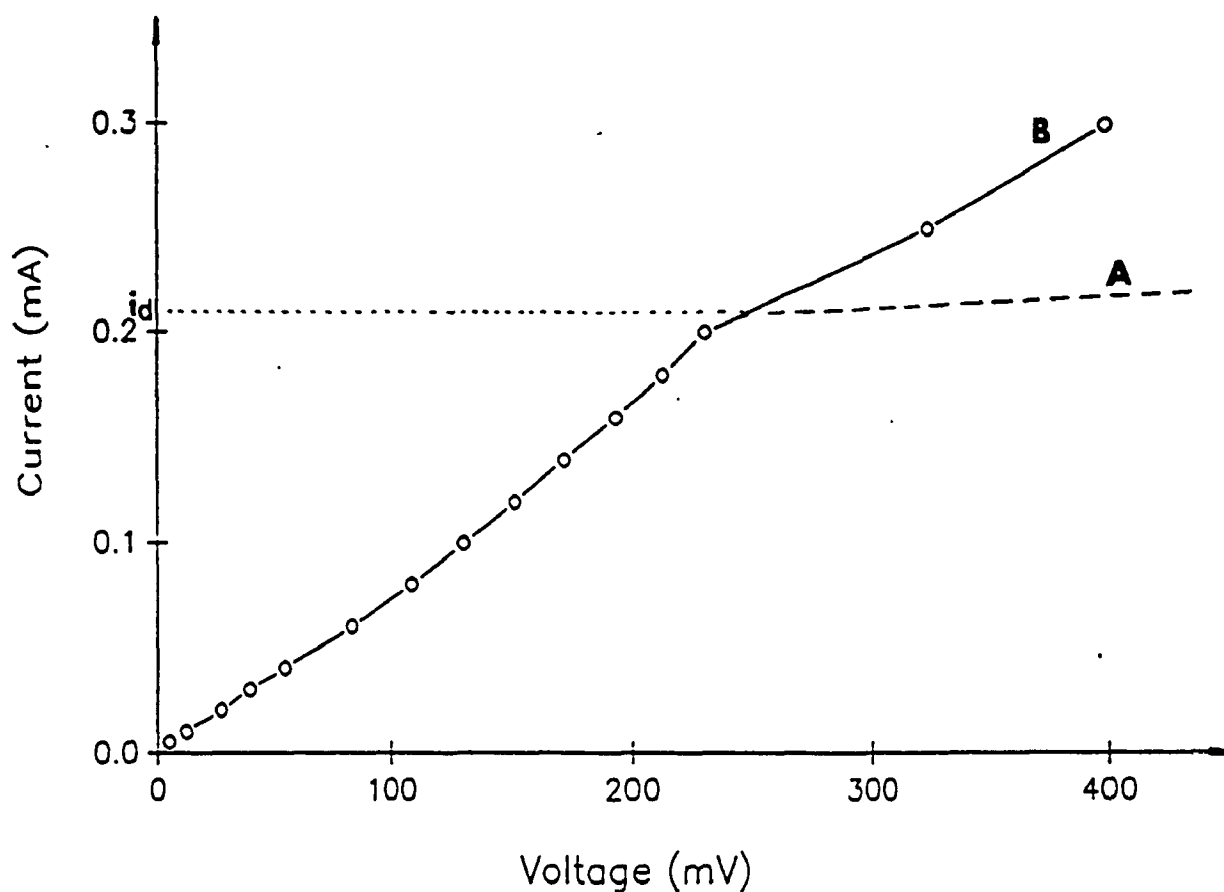
Fig. 6-11 A Schematic Current-potential to Show the Difference
        Between Diffusion-limited Behaviour Obtained at :
        A) A solid Electrode / Aqueous Solution Interface
        B) A Solid Electrode / Solid Electrolyte Interface
        o Experimental Points for the Cu / BaSnF$_4$ Interface
        at T = 80 °C

ANODE

CATHODE

$$Sn \xrightarrow{\ B\ } Sn \xrightarrow{\ 2e\ } \xrightarrow{\ A\ } Sn$$
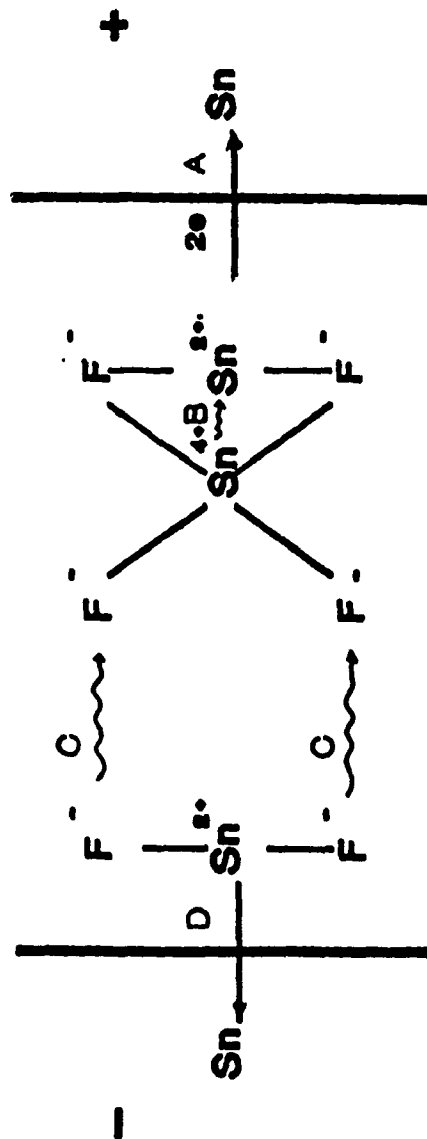
A: oxidation of Sn^{2+} to Sn^{4+} (R.D.S., low T), $Sn^{2+} \rightarrow Sn^{4+}$
B: "diffusion" of Sn^{4+} into the electrolyte (R.D.S., high T)
C: ionic diffusion of F^- to cause formation of "SnF_4"
D: electrodeposition of tin at the cathode, $Sn^{2+} + 2e \rightarrow Sn$

Fig. 6-12   Schematic Electrode Reaction

126

conclusions. However, as the general aspects of the theory fit the experimental results, it is concluded that this theory is essentially correct.

6.2.4. Discussion

Based primarily on the data obtained with a $BaSnF_4$ electrolyte between tin electrodes, it can be concluded that the electrode reactions responsible for charge transfer can be summarized as follows:

The cathodic and anodic reaction are the deposition of tin and the oxidation of Sn^{2+} to Sn^{4+} respectively. As the current-voltage curve exhibits diffusion-limited behaviour, it is suggested that the rate-limiting reaction is the oxidation of Sn^{2+} to Sn^{4+} and the latter's diffusion into the electrolyte. All of the observations are consistent with this hypothesis. Because of the limited temperature range available, the situation with CaF_2-SnF_2 based electrolytes is less clear, although the change of Tafel slopes is measured consistent with the onset of diffusion control.

As a pointer to future work, it can be suggested that a number of confirmatory experiments can be carried out, the most important of which would by the use of the A.C. Impedance technique. This should allow the separation of grain and grain boundary contribution, and show the characteristics of diffusion and allow the determination of the charge transfer parameters.

6.3. ΔH, ΔS and ΔG of MSnF₄

As described in Chapter 4, the potential at which decomposition occurs can be measured using an asymmetric cell employing a copper anode and a tin cathode. In this arrangement, the copper electrode acts theoretically to block the ionic motion though the electrolyte and only the electronic component can be measured. However, when decomposition occurs, a large increase in current occurs at a specific potential - the decomposition potential, E_d -which is directly related to the Gibb's Free Energy of the overall reactions responsible for decomposition. Figure 6-13 shows a typical I-E curve in this measurement and Fig. 6-14 shows the E_d in different temperature. Note that this may not be related to the formation constant for reactions of the type.

$$M + Sn + 2F_2 \;---\rightarrow\; MSnF_4$$
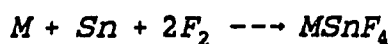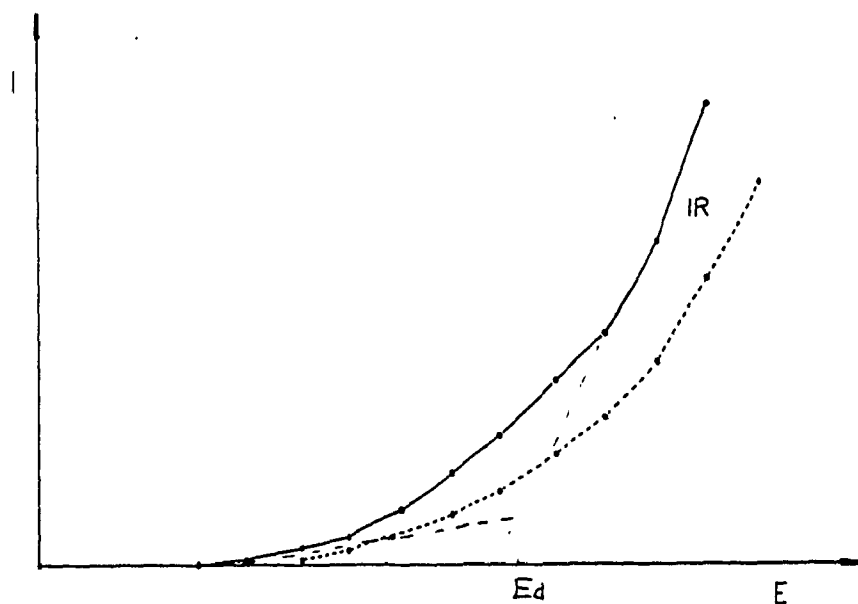
Fig. 6-13 Typical I vs E Curve
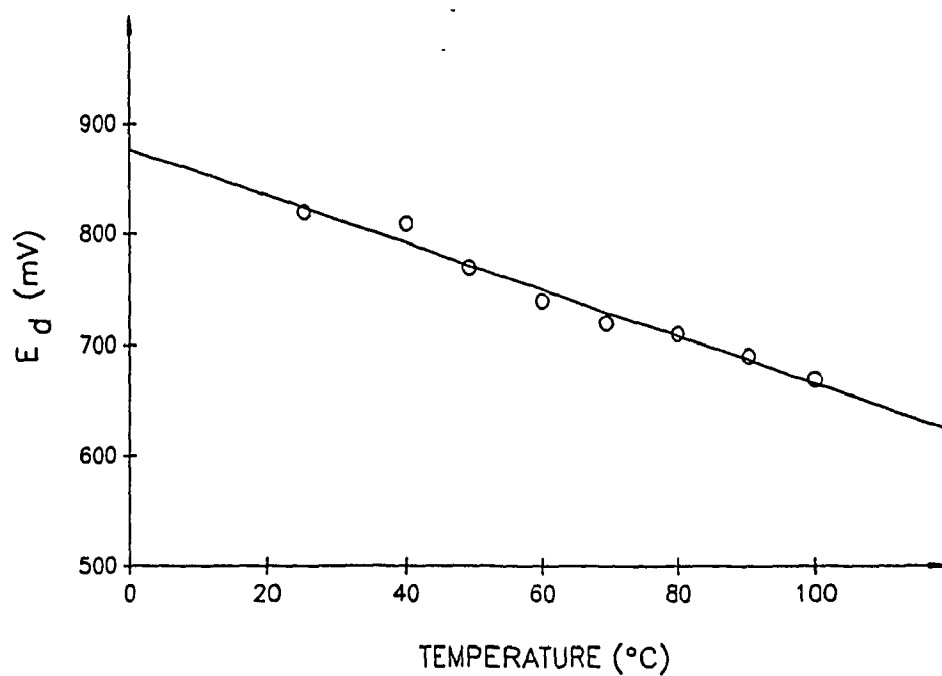
Fig. 6-14 E_d vs T Curve of BaSnF$_4$

More likely in this case, given the discussion in section 6.2, is that decomposition is associated with the oxidation of Sn^{2+} associated with reactions such as:

Cathodic reaction $\quad M^{2+} + Sn^{2+} + 4F^- + 2e \longrightarrow M^{2+} + Sn + 4F^-$

Anodic reaction $\quad \underline{M^{2+} + Sn^{2+} + 4F^- \longrightarrow M^{2+} + Sn^{4+} + 4F^- + 2e}$

overall reaction $\quad 2\,MSnF_4 \longrightarrow M_2SnF_8 + Sn$
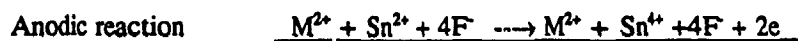
Note again that this does not imply that a compound with the formula, M_2SnF_8, actually exists. Rather this represents the overall composition near to the copper electrode surface. However, such a situation would be favoured by a high electronic conductivity since the voltage developed across the two interfaces equals the total cell voltage minus IR_e, where R_e is the resistance of the electrolyte to electronic motion. Thus comparing the electronic conductivities of the various materials (Table 6.1), $PbSnF_4$ should have the lowest decomposition voltage as is observed. Again this suggests that the Pb^{2+} may participate in both the electronic conduction process (section 6.1.2) and the oxidation process. Thus numerous reaction schemes can be formulated for the anodic reaction in the case of $PbSnF_4$:

a) Simultaneous oxidation of Pb^{2+} and Sn^{2+} to produce a compound such as '$PbSnF_8$'; the extra fluoride ions being supplied by the decomposition of tin at the cathode.

b) Oxidation of Pb^{2+} to Pb^{4+} followed by the two-electron transfer from a neighbouring Sn^{2+} ion.

c) Oxidation of Sn^{2+} to Sn^{4+} followed by two-electron transfer form either a neighbouring Pb^{2+} or Sn^{2+} ion.

The experimental evidence is insufficient to distinguish between these cases.

In the other compounds studied (M = Ba, Ca), these reactions are impossible and only the oxidation of Sn^{2+} can be considered. Although this again depends on the electronic conductivity, the rate of the reaction will also depend on the rate at which fluoride ions can be supplied i.e. the ionic conductivity. Thus, as can be seen from Tables 6.1 and 6.5, SnF_2 has the lowest ionic conductivity and therefore 'exhibits' a high decomposition potential. Note that this may in fact be misleading in that the true decomposition potential may be much lower but at a very low rate, i.e. the exchange current density is lower than our present measurement capabilities. (As an example of such behaviour, hydrogen evolution from aqueous solutions conventionally occurs at 0 V (1M acid) and, at a platinum electrode, this is readily observed because the exchange current density is approximately 10^{-3} A cm^{-2}. In contrast, the exchange current density for hydrogen evolution at a mercury electrode is very low (10^{-13} Acm^{-2}) and a large voltage

(ca. 1.8 V) must be applied before hydrogen evolution can be observed.)

Table 6-5. ΔH, ΔS and ΔG of MSnF$_4$ (25 °C)

Compound	ΔH (cal/mol)	ΔG (cal/mol)	ΔS(cal/mol,deg)	E$_d$(mV)
SnF$_2$	-53000	-46000	-23	1000
BaSnF$_4$	-73600	-42000	-106	910
PbSnF$_4$	-13300	-9200	-14	200
SnF$_2$-CaF$_2$(n=0.67)	-42000	-31000	-38	670

From this discussion, it can be seen that the decomposition potential of all of the SnF$_2$- based conductors studied is less than 1 V making the development of high energy density batteries impractical. Their use as ion and gas sensors is open to some discussion.

6.4. Conclusions

The measurements described in this chapter lead to a self-consistent discussion of the properties. Given the structural and chemical similarities (especially of the Sn^{2+} ion) the decomposition voltages of these compounds are expected to be similar, the only differences being due to charges in the Sn^{2+} concentration (the Nernst Equation for the oxidation of Sn^{2+} implicitly contains [Sn^{2+}]) and possible participation by the other metal cation (e.g. Pb^{2+}) in the electrode reactions. However, as the most probable reaction leading to decomposition is the oxidation of Sn^{2+} which requires the transport of both fluoride ions and electrons, the decomposition rate will depend on both the ionic and the electronic conductivities of the various materials. Thus, in relative terms, in compounds exhibiting both high ionic and electronic conductivity (e.g. PbSnF$_4$), it will be possible to observe a measurable current even at a small apparent voltage. Whereas, in the opposite case (low conductivities e.g. SnF$_2$), a high apparent voltage will be necessary to reach

130

measurable current levels. This leads the conclusion that in all of these materials, the true decomposition voltage is no greater than that of our measured E_d for $PbSnF_4$, i.e. 200 mV. Considering that the standard potential for Sn^{4+} reduction in aqueous solution is 150 mV. This is a reasonable value. However, as this low decomposition voltage would lead to self-charge of high-energy density battery systems, it therefore seems impractical to design such systems and future work should only consider the more basic aspects of these compounds.

CHAPTER 7.

CONCLUSIONS

The work described in this thesis is concerned with the preparation and characterization of solid electrolytes based on tin(II) fluoride. The characterization includes mainly the use of elemental analyses, X-ray diffraction, Mössbauer spectroscopy and bulk density measurements for the study of the reactions taking place, the investigation of the structure of the materials prepared and the determination of their stability. The electrochemical properties include ionic conductivity, electronic conductivity and electrode kinetics.

7.1. The CaF_2-SnF_2 System

Direct reaction of SnF_2 and CaF_2 is known to yield no mixed tin(II)-calcium fluoride. However, it was known that the reaction of aqueous solutions of SnF_2 and calcium nitrate resulted in the formation of an amorphous product with variable composition and the reactions were irreproducible. A detailed study of this reaction has been carried out under carefully monitored conditions. The following results were obtained:

a) Two materials, a crystalline phase suggested to be $CaSn_2F_6$ and a microcrystalline $Ca_{1-x}Sn_xF_2$ solid solution were obtained;

b) Depending on the stoichiometry of the reaction mixture, three results have been observed:

- mixtures rich in Sn (≥ 77 % Sn) give pure $CaSn_2F_6$;

- mixtures with similar amounts of Sn and Ca ($23 < \%Ca < 62$) give a mixture of crystalline $CaSn_2F_6$ and microcrystalline $Ca_{1-x}Sn_xF_2$ solid solution;

- mixtures rich in Ca ($>62\%$ Ca) give a pure $Ca_{1-x}Sn_xF_2$ solid solution.

c) Although the structure of $CaSn_2F_6$ is unknown, it has been established in this work that it contains tin(II) with a stereoactive lone pair of electrons with considerable p character and these electrons do not contribute to the conduction process;

d) The overall structure of the $Ca_{1-x}Sn_xF_2$ solid solution is an undistorted fluorite type, with random substitution of Ca by Sn and random orientation of the lone pair direction. However, although there is no unit-cell distortion due to the statistically random distribution of tin on the metal sites and due to the random orientation of the Sn-E (E = lone pair) axes orientation, Mössbauer spectroscopy shows that there is considerable local distortion due to the relative large size of tin(II) and its lone pair, compared to the size of the fluoride ion cubes.

e) In the region of the reaction mixture stoichiometries where a mixture of the two materials is obtained, it has been found that the end product of the reaction is very strongly dependent on the rate of mixing of the two solutions. Thus a fast dilution of Ca^{2+} ions in a SnF_2 solution gives crystalline $CaSn_2F_6$, whereas if the local concentration of Ca^{2+} is allowed to increase, microcrystalline $Ca_{1-x}Sn_xF_2$ is favoured.

f) Bulk density measurements show that:

- both crystalline and microcrystalline phases are formed without improved packing relative to the mixture of $SnF_2 + CaF_2$, and therefore they can be expected to have a low stability;

- The microcrystalline phase was found to contain considerably less tin than found by chemical analysis, which suggests that it coexists with another phase, which is amorphous and richer in tin, and could not be identified;

g) Crystalline $CaSn_2F_6$ is unstable in aqueous solution; it loses SnF_2 to the solution and yields two microcrystalline fluorite-type phases, one with an average particle diameter of ca. 500 Å, the other of much finer texture, of about 40 Å. Their average composition is $Ca_{0.65}Sn_{0.35}F_2$ possibly Ca_2SnF_6;

h) The SnF_2 released into the aqueous solution, when crystalline $CaSn_2F_6$ is suspended in water, is partially oxidized by the oxygen dissolved in the water; it results in the formation of Sn_7F_{16} and SnO_2. This is the first report of the production of Sn_7F_{16} from an aqueous solution. The reaction of oxidation is consistent with X-ray diffraction and Mössbauer spectroscopic results, including the relative amounts of Sn(II) and Sn(IV) in the samples;

i) Comparing our Mössbauer spectroscopic results and those from the literature, it has shown that, the interpretation of the tin(II) spectrum anisotropy in Sn_2F_7 by other authors in an earlier studies was erroneous,

and it was established that there is no detectable Goldanskii-Karyagin effect on tin(II). However, there are at least two tin(II) sites in Sn_7F_{16}, the structure of which is not known;

j) A combination of X-ray diffraction and conductivity measurements showed that crystalline $CaSn_2F_6$ is stable up to ca. 220 °C, at which point it decomposes to amorphous CaF_2 and liquid SnF_2. This result explains why earlier attempts to carry out syntheses in the CaF_2/SnF_2 system by high temperature reactions failed, and it is in agreement with the poor stability predicted from bulk density measurements.

k) The overall conclusion for this part of this thesis is that we have overcome previously reported difficulties in preparing Ca/Sn(II)/F materials, and defined their conditions of preparation, characterized them and studied their stability.

7.2. Comparison of the Electrochemistry of the CaF_2-SnF_2 System with α-SnF_2 and $MSnF_4$ Compounds

The solid electrolytes are never fully ionic conductors. It is necessary to measure both ionic conductivity and electronic conductivity. The study on the electrochemistry properties of the CaF_2-SnF_2 system have been carried on this work. The results are described below:

a) Ionic conductivity measurements show that $PbSnF_4$ has highest conductivity in all of the MF_2-SnF_2 compounds and SnF_2 shows the lowest conductivity. In contrast, the CaF_2-SnF_2 exhibits intermediate values with the microcrystalline phase having a ten-fold higher conductivity than the crystalline phase.

b) Careful measurements of the electronic component show that the $MSnF_4$ compounds are poor electronic conductors and have an ion transport number ~1. However, in the crystalline phase of CaF_2-SnF_2, which has been suggested has a $CaSn_2F_6$ structure, has a lower ion transport number ($t_i = 0.5$) because it is a tin rich phase.

c) Although $PbSnF_4$ has high ionic conductivity, it also exhibits high electronic conductivity especially at higher temperature, since it has two not fully oxidized cation (Pb^{2+}, Sn^{2+}).

d) The current potential study suggest that at 80 - 90 °C, the electrode reaction of the CaF_2-SnF_2 microcrystalline phase is an irreversible step, while at 110 °C, a two-electron transfer reversible step is

suggested.

e) For BaSnF$_4$, the Tafel slope measurement suggested the electrode reaction rate is limited by a reversible step occurring at one of the electrodes.

f) The anodic reaction is probably due to the oxidation of the tin, that is,

$$Sn \longrightarrow Sn^{2+} + 2e$$

or $\qquad Sn^{2+} \longrightarrow Sn^{4+} + 2e$

g) The cathodic reaction could be due to the electrode composition of the metal or alloy,

$$M^{2+} + 2e \longrightarrow M$$

$$Sn^{2+} + 2e \longrightarrow Sn$$

or $\qquad M^{2+} + Sn^{2+} + 4e \longrightarrow (MSn)_y$
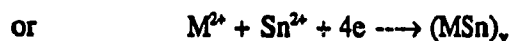
h) As only the oxidation of Sn^{2+} would give rise to diffusion limited kinetics, it is suggested that this is the rate-limiting reaction.

i) According to the study of entropy, enthalpy and Gibb's free energy, BaSnF$_4$ is the most stable material and PbSnF$_4$ is the least stable.

j) Thus the overall conclusion from the electrochemical measurements is that although SnF$_2$ based conductors exhibit interesting conduction properties, they are inherently unstable due to the ease with which the Sn^{2+} ion can be oxidized to Sn^{4+}. This would prevent their application in high energy devices.

135

REFERENCES

1. J. Schoonman, J. Electrochem. Soc., 123, 1772 (1976)

2. J. Schoonman, A. Wolfert, Solid State Ionics, 314, 373 (1981)

3. J.M. Oberschmidt, D. Lazarus, Fast ion Transport in Solids, 691 (1979)

4. Inorganic Solid Fluorides Chemistry and Physics, p. 426 (1985)

5. J.M. Réau, A. Rhandour, S.F. Matar and P. Hagenmuller, Solid State Chem. 55, 7 (1984)

6. C. Lucat, G. Campet, J. Claverie, J. Portier, J.M. Réau and P. Hagenmuller, Mater. Res. Bull. 11, 167 (1976)

7. Inorganic Solid Fluorides Chemistr; and Physics, p. 450 (1985)

8. C. Tubandt, Z. Anorg. Allg. Chem. , 115, 105 (1921)

9. M. Baker, A. Taylor, J. Phys. Chem. Solids, 30, 1003 (1969)

10. H.J. Matzke, J. of Mater. Sci. , 5, 831 (1970)

11. E. Barsis, A. Taylor, J. Chem. Phys. , 48, 4357 (1968)

12. E. Barsis, A. Taylor, J. Chem. Phys., 48, 4362 (1968)

13. J.D. Donaldson and B.J. Senior, J. Chem. soc., A, 1821 (1967)

14. T. Birchall, G. Denes, K. Ruebenbauer and J. Pannetier, Hyperfine Int. 29, 1331 (1986)

15. G. Denes, J. Pannetier and J. Lucas, C. R. Acad. Sc. Paris, 280C, 831 (1975)

16. J. Hladik, Physics of Electrolyte, 221 (1972)

17. W.H. Flygare, R.A. Huggins: J. Phys. Chem. Solids, 34, 1199 (1974)

18. J. Hladik, Physics of Electrolytes, 36 (1972)

19. Paul F. Weller, "Solid State Chemistry and Physics", New York, M. Dekker, 14 (1973)

20. G. Denes, J. Solid State Chem., 77, 54 (1988)

21. D. Mckie and C. Mckie, "Crystalline Solids", New York, Wiley, p. 5 (1974)

22. U. Gonser, Mössbauer Spectroscopy, Topic in Applied Physics (5)", New York, Springer-verlag, p. 64 (1975)

23. T.C. Gibb, "Principles of Mössbauer Spectroscopy" (1976)

24. "International Critical Tables of Numerical Data, Physics, Chemistry and Engineering", ed. E.W. Washbura, NRC, USA, Vol. 111, pp. 27-28, McGraw-Hill, New-York (1928)

25. M.H. Hebb, J. Chem. Phys., 20, 185 (1952)

26. D.O. Raleigh, Progress in Solid State Chemistry, vol.3, 83 (1967)

27. P. P. Schmidt, Electrochemistry, Volume 5, Chapter 2, 1978

28. P. P. Schmidt, Electrochemistry, Volume 6, Chapter 4, 1978

29. S. Glasstone, K.J. Laidler, H. Eyring, The Theory of Rate Processes, 575 (1941)

30. R.A. Swalin, Thermodynamics of Solid (1972)

31. Powder Diffraction File No. 15-744, International Centre for Diffraction Data, Swarthmore, PA (1988)

32. Powder Diffraction File No. 35-816, International Centre for Diffraction Data, Swarthmore, PA (1988)

33. A.R. West, "Solid State Chemistry and its Applications", John Wiley & Son, New York, p. 240 (1984)

34. B.D. Cullity, "Elements of X-Ray Diffraction", 2nd ed., Addison-Wesley, Don Mills, Ontario, pp. 192, 294 (1978)

35. G. Denes, J. Pannetier, J. Lucas and J.Y. Le Marouille, J. Solid State Chem. 30, 335 (1979)

36. T. Birchall, G. Denes, K. Ruebenbauer and J. Pannetier, J. Chem. Soc. , Dalton Tr., 1831 (1981)

37. J. D. Donaldson and J. Silver, J. Chem. Soc. (A), 666 (1973)

38. G. Denes, J. Pannetier, J. Lucas, J. Solid State Chem. 33, 1 (1980)

39. J. Pannetier and G. Denes, Acta Cryst. B 36, 2763 (1980)

40. G. Denes, J. Solid State Chem., 74, 343 (1988)

41. G. Denes, Y.H. Yu, T. Tyliszczak and H.P. Hitchcock, J. Solid State Chem., in press, 90 (1991)

42. M. Durand, J. Pannetier and G. Denes, J. Physique 41, 831 (1980)

43. G. Denes, Y.H. Yu, T. Tyliszczak and H.P. Hitchcock, J. Solid State Chem., Publication in preparation

44. G. Denes, Mat. Res. Bull. 15, 807 (1980)

45. G. Denes and G. Lazanas, J. Chem. Soc. (A), Dalton Tr., in press

46. R. Sabatier, A.M. Hebrard and J.C. Cousseins, C.R. Acad. Sc. Paris, 279C, 1121 (1974)

47. M.F.A. Dove, R. King and T.J. King, J. Chem. Soc., Chem. Comm., 944 (1973)

48. M.C. Madamba, Chem-419 Senior Undergraduate Research Thesis, Concordia University (1989)

49. L. Fournes, J. Grannec, Y. Potin and P. Hagenmuller, Solid State Comm. 59, 833 (1986)

50. L. Fournes, J. Grannec and Y. Potin, Hyperf. Inter. 55, 1137 (1990)

51. V.A. Bryukhanov, N.N. Delyagin, A.A. Opanlenko and V.S. Shpinel, Sov. Phys. JETP Engl. Transl. 16, 310 (1963) [J. Eks. Theor. Phys (USSR) 43, 432 (1962)]

52. N.N. Greenwood and T.C. Gibb, "Mössbauer Spectroscopy", Chapman and Hall, London (1971)

53. T. Birchall, G. Denes, K. Ruebenbauer and J. Pannetier, J. Chem. Soc. , Dalton Tr., 2296 (1981)

54. D. Ansel, J. Debuigne, G. Denes, J. Pannetier and J. Lucas, Ber. Bunsenges. Phys. Chem., 82, 376 (1978)

55. J. Pannetier, G. Denes, M. Durand and J.L. Buevoz, J. Physique, 41, 1019 (1980)

56. G. Denes, J. Solid State Chem. 36, 20 (1981)

57. G. Denes, J. Solid State Chem. 37, 16 (1981)

58. I.V. Murin, S.V. Chernov, M.Yu. Vlasov, A.V. Shashkin, S.R. Tkharkahova, D. Diaz-Gonzalez and A.A. Pronkin, Zhurnal Prikladnoi Khimii, Vol. 58, No.11, 2439-2442 (1985)

59. G. Denes, T. Birchall, M. Sayer and M.F. Bell, Solid State Ionics, 13, 213-219 (1985)

60. M.F. Bell, M. Sayer, D.S. Smith, P.S. Nicholson, Solid State Ionics, 9 & 10, 731 (1983)

61. M.F. Bell and U. Von Alpen, J. Electroanal. chem., 129, 315-320 (1981)

62. R.D. Armstrong and M.F. Bell, J. Electroanal. chem., 129, 321-325 (1981)

APPENDIX I

Preparation of TISAB II

Place about 500 ml distilled water in a 1-litre beaker. Add 57 ml glacial acetic acid, 58 g NaCl and 4 g CDTA (CDTA, available commercially, is cyclohexylene dinitrilo tetraacetic acid, or 1,2-diaminocyclohexane N,N,N'N'-tetraacetic acid). Stir to dissolve. Immerse a calibrated pH electrode into the solution, and slowly add 5 M NaOH until the pH is between 5.0-5.5. Pour into a 1-little flask and dilute to volume with distilled water.

APPENDIX II

Yield of the Products

Molar Fraction n	Yield %	Molar Fraction n	Yield %
0.048	9.8	0.524	37.5
0.09	18.3	0.535	34.8
0.13	22.5	0.545	35.3
0.17	27.0	0.555	42.8
0.20	37.4	0.565	38.9
0.23	37.6	0.574	33.8
0.26	35.6	0.583	38.4
0.286	32.9	0.592	33.7
0.31	38.3	0.60	33.1
0.33	39.7	0.608	33.7
0.35	39.1	0.615	33.1
0.375	37.7	0.623	37.2
0.39	37.0	0.63	33.3
0.41	31.4	0.636	36.9
0.43	32.4	0.643	34.8
0.44	36.1	0.649	34.8
0.46	33.6	0.655	32.4
0.47	33.5	0.661	32.4
0.487	40.4	0.667	32.3
0.50	33.4	0.75	32.0
0.512	37.6	0.80	34.4

APPENDIX III

Results of the Elemental Analyses of the Product

n^*	In % (M/M) in the Product				In % (M/M) in $Ca_{1-x}Sn_xF_2^{**}$				x^{***}
	Sn	Ca	F	NO$_3$		Ca	Ca+Sn	F	
0.048	19.98	11.16	64.53	4.3		11.7	32.65	67.5	0.64
0.20	22.06	13.32	62.25	2.3	22.6	13.6	36.2	63.8	0.62
0.33	15.68	17.06	62.99	4.3	16.4	17.8	34.2	65.8	0.48
0.43	15.42	15.12	64.01	5.4	16.3	16.0	32.3	67.7	0.50
0.50	17.06	17.12	63.57	2.3	17.5	17.5	35.0	64.8	0.50
0.56	16.66	15.06	62.89	5.4	17.2	15.6	32.8	65.0	0.52
0.60	10.72	22.52	66.26	0.5	10.8	22.6	33.4	66.6	0.32
0.64	12.34	20.29	65.63	1.7	12.6	20.7	33.3	71.4	0.38
0.67	9.65	23.86	65.94	0.5	9.7	24.0	33.7	66.3	0.29
0.75	7.9	23.04	67.80	1.2	8.0	23.3	31.3	68.6	0.26
0.80	7.07	21.65	64.32	1.0	7.6	23.3	30.9	69.1	0.25
Average	-	-	65.4	-	-	-	33.2	67.1	-

* n = Ca/(Ca+Sn) molar ratio in the reaction mixture;

** The % in $Ca_{1-x}Sn_xF_2$ where calculated by not taking into account the nitrate impurity, which is not a component of the fluoride phase.

*** x = substitution ratio of Ca by Sn in the formula $Ca_{1-x}Sn_xF_2$.

141

APPENDIX IV

X-Ray Powder Pattern of the Crystalline Phase

Peak Number	$2\theta(°)$	d (Å)	I/I_0
1	18.56	4.782	25
2	20.55	4.321	22
3	23.08	3.853	13
4	24.27	3.667	73
5	24.91	3.574	100
6	25.80	3.453	33
7	26.90	3.314	51
8	28.19	3.165	47
9	28.80	3.100	42
10	32.64	2.744	34
11	33.88	2.646	7
12	37.65	2.389	7
13	39.55	2.279	10
14	40.76	2.214	12
15	41.04	2.199	15
16	41.85	2.158	9
17	42.07	2.147	12
18	42.61	2.122	9

Peak Number	2θ(°)	d (A)	I/I₀
19	43.25	2.092	10
20	43.61	2.075	19
21	44.10	2.053	12
22	44.38	2.041	18
23	45.29	2.002	14
24	46.92	1.936	12
25	47.30	1.922	25
26	47.93	1.898	8
27	49.42	1.844	7
28	50.02	1.823	18
29	50.61	1.804	9
30	51.27	1.782	11
31	51.75	1.766	16
32	53.34	1.717	13
33	55.50	1.656	6
34	58.28	1.583	6
35	59.84	1.546	10

I/I_0 = Relative intensity

143

APPENDIX V

A: X-Ray Powder Pattern of the Micro-crystalline Phase

Peak Number	hkl	2θ(°)	d (Å)	I/I₀
1	111	27.65	3.226	100
2	200	32.00	2.791	25
3	220	46.04	1.971	54
4	311	54.61	1.680	26

I/I_0 = Relative intensity

B: X-Ray Powder Pattern of CaF_2

Peak Number	hkl	2θ(°)	d (Å)	I/I₀
1	111	28.46	3.136	100
2	200	-	-	0
3	220	47.12	1.929	96
4	311	55.85	1.646	29

I/I_0 = Relative intensity

144

APPENDIX VI

X-Ray Powder Pattern Observed for n=0.46 with a Fast Stirring Rate

Peak Number	$2\theta(°)$	d (Å)	I/I_0	Linewidth
1	18.54	4.782	43	N
2	20.60	4.307	26	N
3	23.11	3.846	12	N
4	24.35	3.652	70	N
5	24.98	3.561	100	N
6	25.87	3.442	38	N
7	26.97	3.304	58	N
8	27.62	3.227	15	N
9	28.28	3.153	50	N
10	28.82	3.095	53	N
11	32.64	2.741	37	N
12	37.80	2.378	11	N
13	40.64	2.218	16	N
14	41.15	2.192	12	N
15	41.79	2.160	15	N
16	42.19	2.140	16	N
17	42.66	2.118	10	N
18	43.32	2.087	8	N
19	43.68	2.071	21	N
20	44.39	2.039	20	N
21	46.98	1.933	18	N

Peak Number	$2\theta(°)$	d (Å)	I/I_0	Linewidth
22	47.33	1.919	26	N
23	47.86	1.899	17	N
24	48.38	1.880	7	N
25	49.96	1.824	20	N
26	50.41	1.809	13	N
27	51.42	1.776	10	N
28	51.76	1.765	23	N
29	53.38	1.715	11	N
30	55.55	1.653	11	N
31	58.45	1.578	12	N

I/I_0 = Relative intensity

Linewidth: B=Broad, N=Narrow

APPENDIX VII

X-Ray Powder Pattern Observed for n=0.46 with a Medium Stirring Rate

Peak Number	$2\theta(°)$	d (Å)	I/I_0	Linewidth
1	18.56	4.776	100	N
2	20.61	4.306	17	N
3	23.13	3.842	10	N
4	24.31	3.658	51	N
5	24.94	3.567	56	N
6	25.87	3.441	18	N
7	26.92	3.309	25	N
8	27.65	3.224	25	B
9	28.05	3.179	57	N
10	28.92	3.085	21	N
11	32.71	2.735	26	N
12	37.85	2.375	8	N
13	39.65	2.271	8	N
14	40.75	2.213	12	N
15	41.15	2.192	7	N
16	41.82	2.158	6	N
17	42.19	2.140	9	N
18	42.74	2.114	8	N
19	43.66	2.072	12	N
20	44.29	2.043	5	N
21	45.29	2.001	7	N

Cont.

Peak Number	$2\theta(°)$	d (Å)	I/I_0	Linewidth
22	45.84	1.978	9	N
23	47.35	1.918	18	N
24	47.80	1.901	9	N
25	49.88	1.827	6	N
26	50.53	1.805	6	N
27	51.29	1.780	5	N
28	53.41	1.714	7	N

I/I_0 = Relative intensity

Linewidth: B=broad, N=narrow

X-Ray Powder Pattern Observed for n=0.46 with a Slow Stirring Rate

Peak Number	2θ(°)	d (Å)	I/I₀	Linewidth
1	18.55	4.775	69	N
2	24.30	3.663	23	N
3	25.01	3.561	26	N
4	27.56	3.236	100	B
5	28.84	3.095	24	N
6	31.98	2.798	25	B
7	32.70	2.739	22	N
8	37.80	2.380	21	N
9	45.87	1.978	49	B
10	47.44	1.916	19	N
11	51.98	1.759	9	N
12	54.38	1.687	18	B

I/I_0 = Relative intensity

Linewidth: B=broad, N=narrow

APPENDIX IX

Unit Cell Parameter of the $Ca_{1-x}Sn_xF_2$ Microcrystalline Phase as a function of the molar fraction "n" of Ca in the Reaction Mixture

x	n	a (Å)	x	n	a (Å)
0.25	0.80	5.5528		0.54	5.6085
0.26	0.75	5.5540	0.50	0.50	5.5508
		5.5366		0.49	5.4812
		5.5315		0.46	5.5386
0.29	0.67	5.5642		0.44	5.5588
	0.66	5.6207		0.43	5.5503
	0.65	5.5747	0.50	0.41	5.5802
0.38	0.64	5.5712		0.39	5.5739
	0.63	5.5755		0.37	5.5583
	0.61	5.5613		0.35	5.5739
	0.60	5.5579		0.33	5.5581
	0.59	5.5791	0.48	0.31	5.4386
0.32	0.58	5.5905		0.28	5.5581
	0.57	5.5783		0.26	5.6255
		5.5833]			
CaF_2	5.4592 (This work)				
CaF_2	5.4626 [33]				

APPENDIX X

Typical Mössbauer Parameters for Different Environments
and Oxidation States of Tin

Isomer Shifts δ

(Due to the s electron density at the tin-119 nucleus)

Referenced to $CaSnO_3$ = 0

Sn^o = 1.5 - 2.5 mm/s

Sn^{2+} = 2.5 - 4.0 mm/s

Sn^{4+} = -0.6 - 1.5 mm/s

Quadrupole Splitting Δ

(Due to unequal occupancy of the 5p orbitals resulting from covalent bonding and to non-symmetrical coordination.)

Sn^o and inorganic Sn^{4+} = 0 -1.0 mm/s

Sn^{2+} dominated by non-bonding electrons:

Stereoactive lone pair > 1.5 mm/s

Non-stereoactive lone pair= 0 - 0.5 mm/s

Zeeman Magnetic Hyperfine Splitting

All oxidation states of tin are diamagnetic, therefore there is no spontaneous internal field. Magnetic splitting is observed only if a transferred field from a magnetically ordered sublattice is present, or in an applied field.

APPENDIX XI

Bulk Density of the Products

n	x	Density (g/cm^3)		$\Delta\rho/\rho$ (°/°)	x'
		ρ_m	ρ_c		
0.05	0.64	4.28(4)			
0.17		4.23(3)			
0.31		4.152(7)			
0.47		3.951(7)			
0.55		3.69(1)			
0.61		3.68(9)			
0.67	0.29	3.47(7)	3.89	12.1	0.15
0.75	0.26	3.37(4)	3.82	13.4	0.11
0.80	0.25	3.33(4)	3.79	13.8	0.10
α-SnF$_2$* [35]		4.84	4.88	0.8	
CaF$_2$* [33]		3.18			

* Literature values

ρ_m = measured density

ρ_c = density calculated from the unit-cell and the chemical composition

x = Tin substitution ratio in the Ca$_{1-x}$Sn$_x$F$_2$ determinated from Chemical Analysis

x' = Tin substitution ratio in the Ca$_{1-x}$Sn$_x$F$_2$ determinated from the unit-cell
parameter and measured density

152

APPENDIX XII

Bragg Peaks Found in a Sample (n=0.05) After Washing with Water

Peak Number	hkl	$2\theta(^\circ)$	d (Å)	I / I_0
1	$(111)_B$	26.13	3.407	16
2	111	27.80	3.206	100
3	200	32.40	2.761	11
4	220	46.45	1.953	71
5	311	55.07	1.666	22

I/I_0 = Relative intensity

$(111)_B$ = (111) Bragg peak, which is very highly broadened

X-ray Powder Pattern of the Solid Residue

After Evaporation of the Water Used For Washing Crystalline $CaSn_2F_6$

Peak Number	2θ (°)	d (Å)	I/I_0
1	17.61	5.033	36
2	19.95	4.446	28
3	21.07	4.212	7
4	24.48	3.633	100
5	24.90	3.5573	67
6	25.55	3.484	16
7	26.11	3.411	68
8	26.73	3.333	12
9	27.69	3.220	62
10	29.20	3.056	7
11	29.91	2.985	6
12	30.66	2.913	8
13	31.43	2.844	29
14	34.23	2.617	21
15	35.34	2.538	18
16	37.60	2.391	17
17	38.52	2.335	9

Cont.

Peak Number	2θ (°)	d(Å)	I/I_0
18	40.29	2.237	14
19	41.41	2.179	17
20	43.35	2.086	11
21	44.51	2.034	8
22	44.87	2.018	10
23	45.62	1.987	14
24	47.84	1.900	8
25	48.37	1.880	11
26	48.96	1.859	6
27	49.39	1.844	6
28	49.69	1.833	12
29	50.18	1.816	11
30	51.09	1.786	11
31	51.61	1.770	15
32	52.14	1.752	14
33	53.66	1.707	18
34	53.96	1.698	14
35	55.28	1.660	10
36	57.48	1.602	10
37	58.59	1.574	8

I/I_0 = Relative intensity